PREDICTION OF GAS DISTRIBUTION
USING SEISMIC SIMULTANEOUS INVERSION METHOD

A Proof of Concept for Upper Gabus Massive Formation of RAF Field, West Natuna Basin - Indonesia

THESIS

LUKMAN HIDAYAT

0 7 0 6 1 7 1 9 7 0

UNIVERSITY OF INDONESIA

FACULTY OF MATHEMATICS AND NATURAL SCIENCES

RESERVOIR GEOPHYSICS GRADUATE PROGRAM

JAKARTA

DECEMBER 2009

PREDICTION OF GAS DISTRIBUTION
USING SEISMIC SIMULTANEOUS INVERSION METHOD

A Proof of Concept for Upper Gabus Massive Formation of RAF Field, West Natuna Basin - Indonesia

THESIS

Proposed for partially fulfill one of the requirements to earn degree Master of Science

LUKMAN HIDAYAT

0 7 0 6 1 7 1 9 7 0

UNIVERSITY OF INDONESIA

FACULTY OF MATHEMATICS AND NATURAL SCIENCES

RESERVOIR GEOPHYSICS GRADUATE PROGRAM

JAKARTA

DECEMBER 2009

APPROVAL PAGE

Thesis submitted by

Name	: Lukman Hidayat
NPM	: 0706171970
Study Program	: Reservoir Geophysics
Thesis title	: Prediction of Gas Distribution Using Seismic Simultaneous Inversion Method - *A Proof of Concept for Upper Gabus Massive Formation of RAF Field, West Natuna Basin - Indonesia*

Has been approved by the committee member and accepted in partial fulfillment of the requirement for the Degree of Master of Science in Reservoir Geophysics, Faculty of Mathematics and Natural Sciences, University of Indonesia.

Supervisor,

Prof. Dr. Suprajitno Munadi
NIP. 100 003 427

Examiners:

Dr. Abdul Haris

Dr. Waluyo

Dr. Ricky Adi Wibowo

Chairman,

Dr. Dedi Suyanto
NIP. 195508041981031006

Defense date: **December 4th, 2009**

ABSTRACT

The change of lateral rock properties such as porosity, density, fluid saturation etc are reflected in seismic impedance changing. It is known widely that seismic inversion allows us for correlation investigation in the impedance domain which often highlights uniquely the change of rock properties. However the analysis of the early P-wave full-stack seismic inversion data alone can lead to ambiguous conclusions in many exploration situations.

Answering this problem, performing simultaneous inversion will bring us to a less ambiguous interpretation of our inversion results in which we are able to estimate Density, P and S-impedance which have sufficiently different response to discriminate fluid and lithology effects. Utilizing the mathematical concept of AVO inversion, simultaneous inversion use partial angle stack data which can be inverted simultaneously using wavelet extracted from each offset.

Later, these parameters combined with rock physics technique analysis can be used as a tool to predict sand, porosity and saturation distribution. Also, they can be transformed to Lambda-Rho ($\lambda\rho$) that is used for pore fluid content indicator. Finally by analyzing the rock properties distribution map overlaid by structure map and producer well, we can identify the potential area for further development strategy to optimize the hydrocarbon recovery of the study area.

ABSTRAK

Perubahan sifat-sifat batuan seperti porositas, densitas, saturasi dan lain-lain terefleksikan oleh perubahan impedansi seismik. Seperti diketahui, inversi seismik memungkinkan kita untuk mencari korelasinya pada domain impedansi, yang secara unik sering mencirikan perubahan sifat-sifat batuan. Namun demikian, analisa dari seismic inversi *full stack* gelombang-P membawa kita pada kesimpulan yang membingungkan pada banyak situasi explorasi.

Dengan melakukan inversi simultan, kita diarahkan pada interpretasi hasil inversi yang lebih pasti dimana kita dapat mengestimasi densitas, impedansi P dan S yang memberikan respon yang cukup berbeda dalam memisahkan pengaruh *lithology* dan fluida. Dengan menggunakan konsep matematika inversi AVO, inversi simultan menggunakan data *partial angle stack* yang kemudian diinversikan secara bersamaan menggunakan *wavelet* yang di *extract* dari setiap *offset*.

Kemudian dengan mengkombinasikan parameter-parameter ini dengan teknik analisa *rock physics* yang dapat digunakan sebagai alat untuk memprediksi distribusi *lithology*, porositas dan saturasi. Kemudian parameter-parameter ini juga dapat ditransformasikan menjadi Lambda-Rho yang dapat digunakan sebagai indikator kandungan fluida di pori batuan. Akhirnya dengan menganalisa peta distribusi sifat batuan yang di *overlay* dengan peta struktur dan sumur produksi, kita dapat mengidentifikasi area potensial untuk strategi pengembangan lebih lanjut untuk mengoptimalkan pengurasan hidrokarbon pada area studi.

KATA PENGANTAR

Alhamdulillah, puji syukur penulis panjatkan ke hadirat Allah SWT yang telah melimpahkan hidayah, taufiq, rahmat dan karuniaNya sehingga tesis ini dapat diselesaikan pada saatnya.

Ungkapan rasa terima kasih yang sebesar-besarnya dan setulusnya penulis haturkan kepada Prof. Dr. Suprayitno Munadi selaku pembimbing tesis serta seluruh staf dosen pengajar dan administrasi Program Pasca Sarjana Geofisika Reservoir UI 2007 – 2009 yang telah membantu dalam proses pembelajaran. Ucapan terima kasih juga penulis sampaikan kepada teman-teman sekelas dan sekantor atas bantuan, diskusi dan masukan-masukannya yang sangat berharga dalam penyusunan thesis.

Tidak lupa, penulis menyampaikan rasa terima kasih kepada orang tua kami terkasih, istri dan putra-putri kami tercinta, yang tak henti-hentinya mengiringkan doa, dorongan dan semangat kepada penulis dalam pengerjaan thesis ini. Terakhir ucapan terima kasih penulis sampaikan kepada manajemen PT ConocoPhillips Indonesia yang telah memberikan dukungan dan perijinan dalam penggunaan data untuk thesis ini.

Akhir kata, penulis menyadari hasil penelitian ini merupakan tahap awal yang mungkin masih mengandung banyak kekurangan dan diharapkan selanjutnya dapat dilakukan lagi penelitian untuk memperbaiki, melengkapi dan menyempurnakan hasil penelitian ini.

Alhamdulillahirabbil ‘aalamin.

Jakarta, Desember 2009

Table of Contents

Table of Figures

Table of Tables

Chapter One:
INTRODUCTION

1.1 Background

Recently most of the obvious structural traps have been tested by exploration activities over the past 80 years. Explorationists have now begun to focus on the more subtle trap types. The most significant of these traps are stratigraphic and or combination stratigraphic-structural traps. These traps were formed by laterally changing in depositional environment and associated with facies changes which reflected in changing rock properties such as porosity, density, fluid saturation etc which have unique rock physics properties. In seismic data this changes are reflected by changing in seismic impedance laterally and furthermore it is known widely that seismic inversion allows us for correlation investigation in the impedance domain which often highlights uniquely rock properties changing and which then characterize the reservoir which include delineating, correlating and describing the reservoir both in quality and or quantity.

Seismic inversion is a technique that has been used by geophysicists for almost 30 years for reservoir characterization. Early inversion techniques transformed the seismic data into P-Impedance (the product of density and P-wave velocity), from which we were able to make predictions about lithology and porosity. However, these predictions were somewhat ambiguous since P-Impedance is sensitive to combined effect of lithology, fluid and porosity effects, and it is difficult to separate the influence of each effect.

Answering this challenge, Seismic Simultaneous Inversion method is designed to perform a less ambiguous interpretation of our inversion results, in which we estimate P-Impedance, S-Impedance (the product of density and S-Wave velocity) and density simultaneously. The reason for this is that the P and S-Wave response of the subsurface is sufficiently different to allow us to see the difference between fluid and lithology effects. We have now progressed to the point where inversion for P-Impedance, S-Impedance and density is feasible.

Utilizing the mathematical concept of AVO inversion, Seismic Simultaneous Inversion method use partial angle stack data (near, mid, far offset stack) and each partial angle stack was inverted simultaneously using wavelet extracted from each offset to estimate P and S-impedance (Z_P and Z_S) and furthermore very reliable density (ρ) estimates can be derived from this inversion, which have proven very useful in prediction of certain lithology and fluid saturation. Those 3 inversion results can be then transformed to Lambda-Rho ($\lambda\rho$) – which known as *Incompressibility* that is used for pore fluid content indicator in this case hydrocarbon potential and Mu-Rho ($\mu\rho$) – known as *Rigidity* that can be used for Lithology indicator since this parameter is sensitive to rocks matrix character. Additionally, a V_P/V_S volume is also generated from P and S impedance to eliminate the density effect to see how this parameter can distinguish the fluid effect.

RAF Field is setted at tertiary fluvio-deltaic depositional environment system which contains mutiple pay zones and vary in sand quality and distribution. A conventional seismic interpretation technique may have been very uncertain in this deposition environment. For this reason, this study is intending to reduce this uncertainty as well as a proof of concept to show how the Seismic Simultaneous Inversion method result and its derivatives combined with rock physics analysis technique will lead us to a delineation of hydrocarbon bearing distribution prediction. Further, this delineation may support development strategy in optimizing hydrocarbon recovery from this field.

1.2 Thesis Objectives

The main objective of this study is to perform Seismic Simultaneous Inversion method as a proof of concept and provide a better image for predicting gas distribution at Upper Gabus Formation of RAF Field, West Natuna Basin – Indonesia. Going forward with this prediction result, it can be identified several potential areas for further development extension to optimize hydrocarbon recovery.

This study is also performed to partially fulfill the requirements for the master degree of Science in Reservoir Geophysics Graduate program, Faculty of Mathematics and Natural Sciences, Department of Physics, University of Indonesia.

1.3 Thesis Scope

This study will cover the estimation of Impedance (P and S) and Density volume through Seismic Simultaneous Inversion method following the workflow which will be explained later in Chapter IV. These volumes and its derivatives, such as Lambda-Rho, Mu-Rho and V_P/V_S, are used and analyzed to delineate and predict the gas and porosity distribution. This prediction will be used to identify and locate the potential area for next development extension which requires more integrated study. This thesis will not generate any numbers of reserves as it is not allowed by company and MIGAS policy.

1.4 Object and Study Area

The object of this study is Upper Gabus Formation of RAF Field which will be analyzed based on observation of well logs, seismic data and its derivatives.

RAF Field is situated at West Natuna Basin and located in the southwestern part of the South China Sea. It is about 1100 km north of the Jakarta, approximately 300 km northeast of Singapore, and just west of Natuna Island, in the shallow waters between Indonesia and Malaysia on the Sunda Shelf (figure 1.1).

Figure 1.1 Study area located at West Natuna B Block, South China Sea

1.5 Hypothesis

In this study, there are some hypotheses that will be attested, they are:

- There is a relationship between rock physics (Z_P, Z_S, V_P/V_S, $\lambda\rho$, $\mu\rho$) and rock properties (Density, Porosity, Gas saturation, Shale Volume) in the data of the study area.
- Seismic Simultaneous inversion method is feasible to be applied in this study area and can be used to estimate a reliable P-impedance, S-impedance and Density volumes
- Its derivative products and combination with rock physics allow us to carry out qualitative and quantitative analysis to predict and estimate the desired reservoir characters: porosity, gas distribution, its geometry and connectivity.

1.6 Data Availability and Assumptions

This study will use RAF Field dataset: Well and Seismic data. For well data, this field has 4 exploration wells and 3 development wells (table 1.1). However, only 2 of them: RAF-3 and NE RAF-1 will be considered to be used for the simultaneous inversion since both compressional and shear sonic are only available at these wells and the other wells such as RAF-2, RAF-A01 and RAF-A02 will be used for blind well testing. For seismic data, this study use a part of 3D seismic survey which are clipped at Inline 6200 – 8950 and Xline 4600 – 5400 to cover only RAF field (figure 1.2). This survey has set of Full and Partial angle stack seismic volumes: Near Stack (5°-15°), Mid Stack (15°-25°) and Far stack (25°-35°) of Western Geco 2005 reprocessing.

All well logs and 3D seismic data that are used in this study are assumed that have been through valid environment correction, calculation and or conditioning process.

WELL NAME	TYPE	SONIC		CKS	GAMMA	RESISTIVITY		CALI	DENSITY	NEUTRON	WATER	EFF	SHALE
		COMP	SHEAR	VSP	RAY	SHALLOW	DEEP				SAT	PORO	VOLUME
RAF-1	Vertical	No data due to drilling problem at 3800'											
RAF-2	Vertical	DT	-	v	GR	RTS	RTD	CAL	DEN	NPHI	SW	PHIE	VSHL
RAF-3	Vertical	DTCO	DTSM	v	CGR	RTS	RTD	CALI	RHOB	NPHI	SW	PHIE	VSHL
RAF-A01	Slant	-	-	-	GR	RTS	RTD		RHOB	NPHI	SW	PHIE	VSHL
RAF-A02	Slant	-	-	-	GR	RTS	RTD		RHOB	NPHI	SW	PHIE	VSHL
RAF-A04	Horizontal	Can not be used											
NE RAF-1	Vertical	MDT	XDT	v	GR	RTS	RTD	CALI	RHOB	NPHI	SW	PHIE	VSHL

Table 1.1 Well data availability which are required for this study

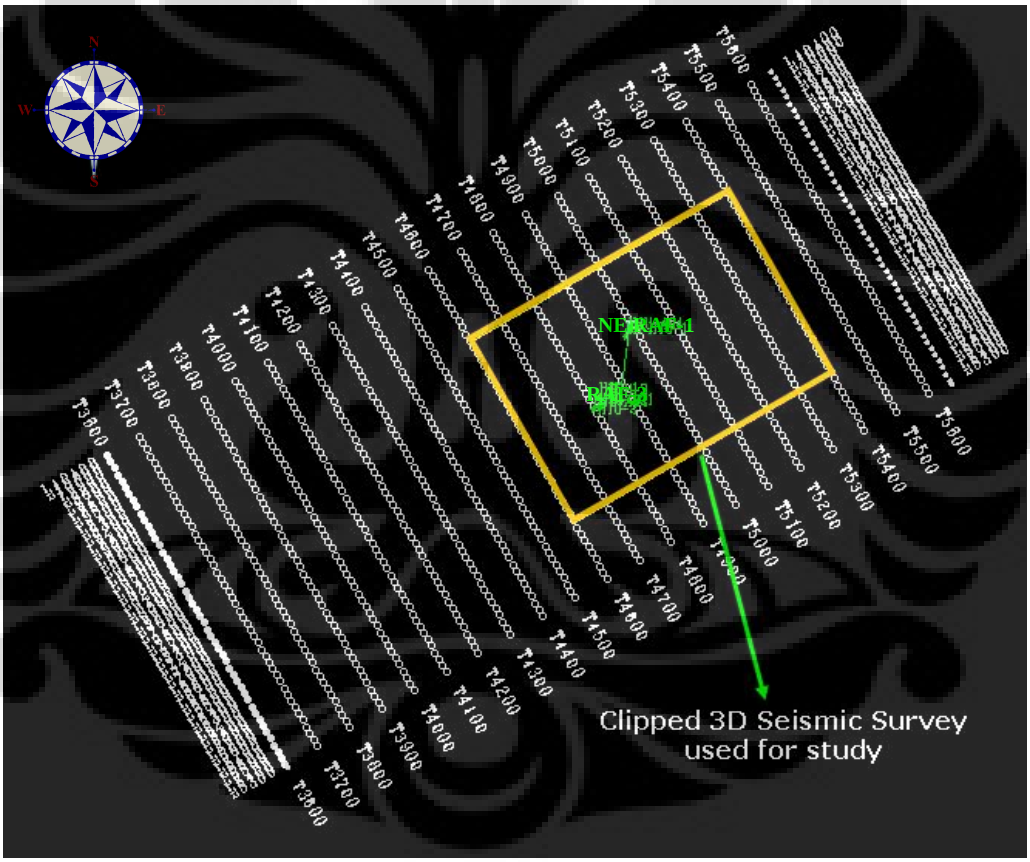

Figure 1.2 3D seismic data which are clipped at limited area for this study

Chapter Two:
REGIONAL AND FIELD GEOLOGY

2.1 Regional Geology

RAF Field is located at the northern part of West Natuna B Block and situated at West Natuna Basin. The present day configuration of the West Natuna basin (figure 2.1) was mainly composed by 2 main tectonic regimes: extensional regime, which produced Eosen – Oligosen graben phase and compressional regime, which produced Miocene sinistral and dextral wrench fault phase. Two major tectonic events (Tapponier, 1982 opcite Daines et al., 1985) which responsible for these regimes history are:

- The collision of Indian and Eurasian plates during the Middle Eocene.
- The collision of the Australian continental shelf with the Philippine Sea plate during the Early Miocene.

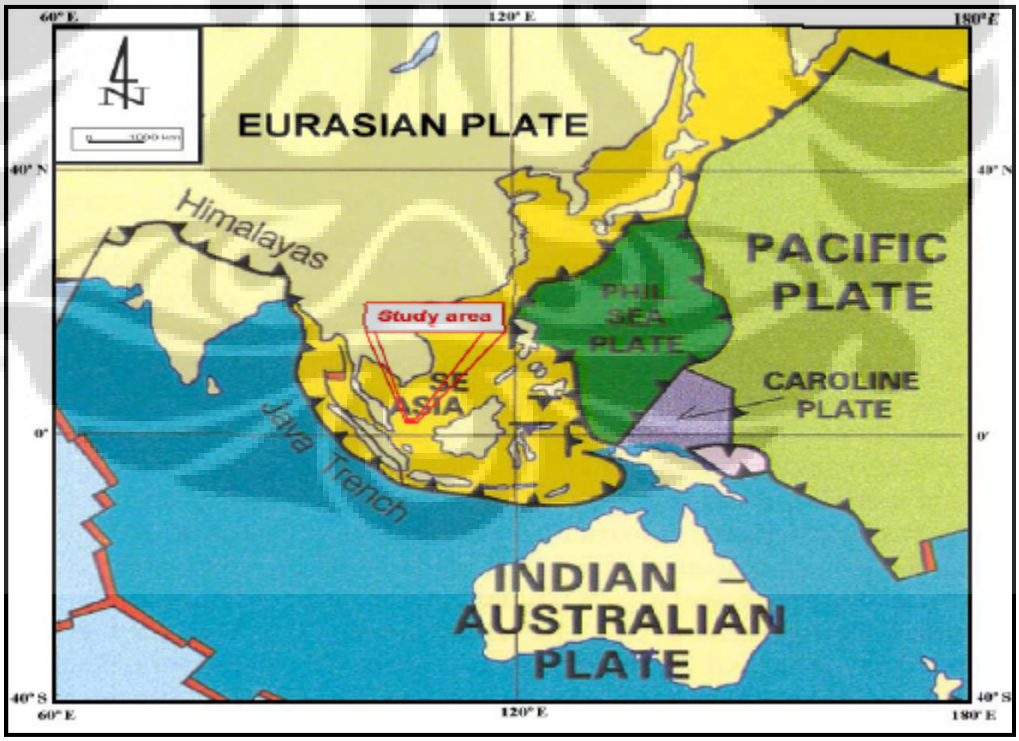

Figure 2.1 Present plate tectonic overview of study area (Daines et al, 1985).

The basin was initially formed during the Eocene-Oligocene along the Eastern border of South Asia which characterized by oblique extensional rifting that generated northeast-southwest trending faults systems (White et al., 1978). These fault systems occur at different scales and are characterized by down to the northwest half grabens formed by northwest dipping, planar, domino-style faults. The graben margins appear to be controlled by northwest-southeast trending basement structures. The origins of this structure are not well understood, although they are possibly related to left-lateral strike slip faults formed by the extrusion tectonics of Southeast Asia. Predominantly granitic basement provided the provenance for coarse continental clastics, which filled in the basin. Belut and Gabus sediments were deposited in fluvial and lacustrine environments during this period.

From Late Oligocene to Middle Miocene, a compressive and wrenching phase caused structural inversion of the basin. This produced fault-related folds on the re-activated extensional northeast-southwest-trending fault systems. This structural inversion phase was probably caused by Indonesian-Australian plate collision and subduction east of Sulawesi. Many original half-grabens were inverted into faulted anticlines which now are major exploration targets. While deposition continued in a marginal marine/estuarine setting with fluvial and marginal marine deposits of the Udang, Barat and Upper Arang Formations.

The compression was then ceased by the end of Middle Miocene and a regional unconformity developed. Subsequently a regional sag phase dominated the structural regime. This period was resulting Muda Shales which generally is considered to be open shelf, shallow marine deposits.

Ginger et al., (1993) divided the West Natuna basin into 4 (four) major tectono-stratigraphic units: Syn-Rift, Post-Rift, Syn-Inversion, and Post-Inversion.

- **Syn-Rift Stratigraphy**

  The Syn-Rift stratigraphic sequence is characterized by divergent seismic reflection geometries that thicken onto the rift border faults and shows poor continuity from one half graben to others. Syn-rift stratigraphic sequence is dominated by non-marine fan delta, coarse alluvial fan, fluvial and lacustrine deposits. There are 2 intervals of potential source rock could be identified at this

sequence, they are deep lacustrine shale of early syn-rift and shallow lacustrine shale of late syn-rift which known as Belut Formation.

- **Post-Rift Stratigraphy**

  The Post-Rift stratigraphic sequence is characterized by a gradual, stratigraphic thickening toward the deepest parts of the inactive half-grabens and a relatively thin section over flexural highs. The post-rift sequence is generally nonmarine, characterized by widespread fluvial braided channel systems. The lower part of this sequence is dominated by lacustrine facies which interpreted was deposited on large and shallow lake (Ginger et al., 1993). This interval is known as Keras Shale member. Subsequently, Upper Gabus formation was conformably deposited over Keras Shale member and showing the early environment changing from lacustrine to prograding plain delta and fluvial braided channel system. The indicator of marine influence is seen at Upper Gabus and Barat formation which contain *Miliammina foraminifera* in mudstone of these both formations (Ginger et al., 1993).

- **Syn-Inversion Stratigraphy**

  The Syn-Inversion sequence represents a period of lacustrine to nonmarine deposition to open marine conditions due to the connection to the sea from the northeast. Syn-Inversion deposit that found in this basin is Barat formation which then overlaid by Arang formation on fluctuated environment between shallow marine and coal swamp-dominated coastal plains (Ginger et al., 1993). This fluctuation is interpreted, was controlled by inversion events and regional relative sea level changing. The general configuration of this sequence is stratigraphic thinning sediment package due to erosion and/or non-deposition toward the crest of the inversion anticlines and thickening toward the flanks. Understanding local sediment dispersal distribution caused by the uplift and erosion of the inversion anticlines is important because it directly affects reservoir quality distribution and paleogeography.

- **Post-Inversion Stratigraphy**

  The Post-Inversion stratigraphy is characterized by predominantly shallow marine deposition. It is easily recognized on seismic data by a basal regional

unconformity. In this sequence, Muda formation was deposited unconformable over Arang formation. Predominantly, Muda formation was deposited on shallow marine environment which fluctuated due to regional relative sea level changing (Ginger et al., 1993). This section is an important seal interval; it provides key source-rock maturation overburden in some areas (Wongsosantiko et al., 1984).

A summary of stratigraphic and tectonic relationships in the basin is shown in figure 2.2.

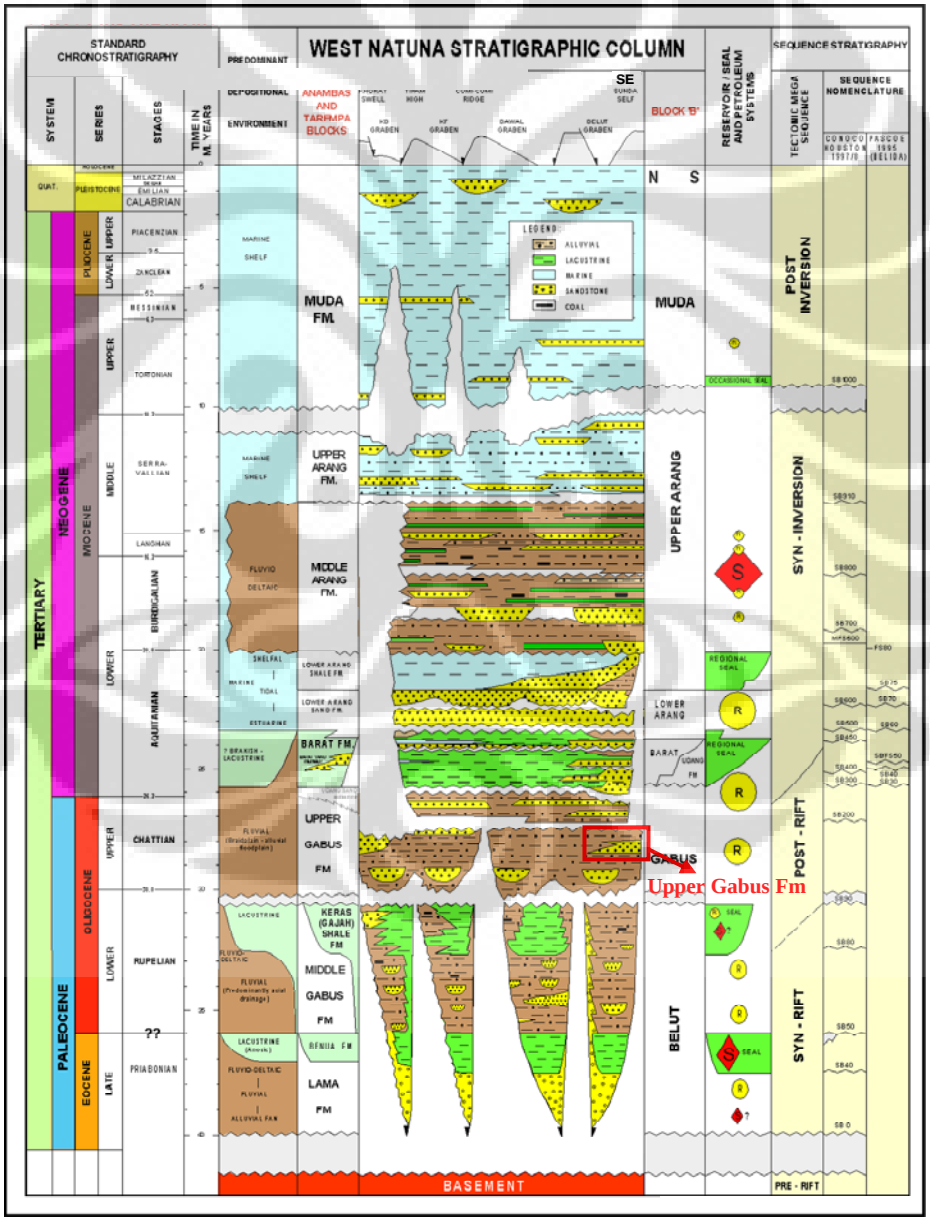

Figure 2.2.Tectono-Stratigraphy of West Natuna Basin (Modified from Daines, 1985).

2.2 RAF Field Summary

RAF field is located in West Natuna B Block, at South China Sea. Water depth is approximately 300 ft. It comprises of 2 structures: RAF structure, 4.5 km long by 3 km wide and NE RAF structure, 2.5 km long and 1.75 km wide. The structures are inverted fault blocks, NE-SW anticline with 4 way dip closure, bounded by a major reverse fault on the south and cut by a series of smaller faults perpendicular to the anticlinal axis. Figure 2.3 shows structure map of Top Upper Gabus Formation.

RAF structure was tested in 1979 by RAF-2 exploration well and discovered the hydrocarbon accumulation. A total of 4 wells have been drilled to date – 2 exploration and 2 development wells (table 2.1). It contains multiple stacked pay zones in the Upper Gabus (UG 1A, 1B, 1C, and UG Massive), Gabus Zone-3 (Z3), and Lower Gabus (LG) reservoir sands. Figure 2.4 is showing hydrocarbon distribution over RAF field prior developed.

RAF is predominantly a gas accumulation and Upper Gabus is introduced Lowest Known Gas. Gas water contact was generated from pressure plots (figure 2.5). Appraisal well RAF-3 confirmed reservoir continuity and fluid contacts. Oil is present in LG Sands, 41 API gravity, waxy, 90-95 °F pour point and contains up to 3% CO2. The average reservoir pressures are 1,780; 2,100 and 2,450 psig for UG, Z-3 and LG respectively.

No	Wells	Type	Spud Date	Status
1	RAF-2	exploration	Sept,1979	P&A, oil and gas well
2	RAF-3	exploration	May,2000	P&A, oil and gas well
3	NE RAF-1	exploration	Nov, 2002	P&A, gas well
4	RAF-A01	development	Mar 2005	Gas producing well
5	RAF-A02	development	Apr, 2005	Gas producing well
6	RAF-A04	development	May,2005	Gas producing well

Table 2.1 RAF Field drilling history

NE RAF structure is faulted anticline located at the north east of RAF structure. The total size is 2.5 km long and 1.75 km wide (figure 2.3). Exploration well NE RAF-1, drilled in November 2002, was to establish hydrocarbon type and reservoir sand quality on a structural nose trending NE – SW adjacent to RAF structure. RDT data confirmed

that NE RAF has separate fluid contacts from RAF reservoir although fluid analyses showed that NE RAF gas is similar to RAF in composition.

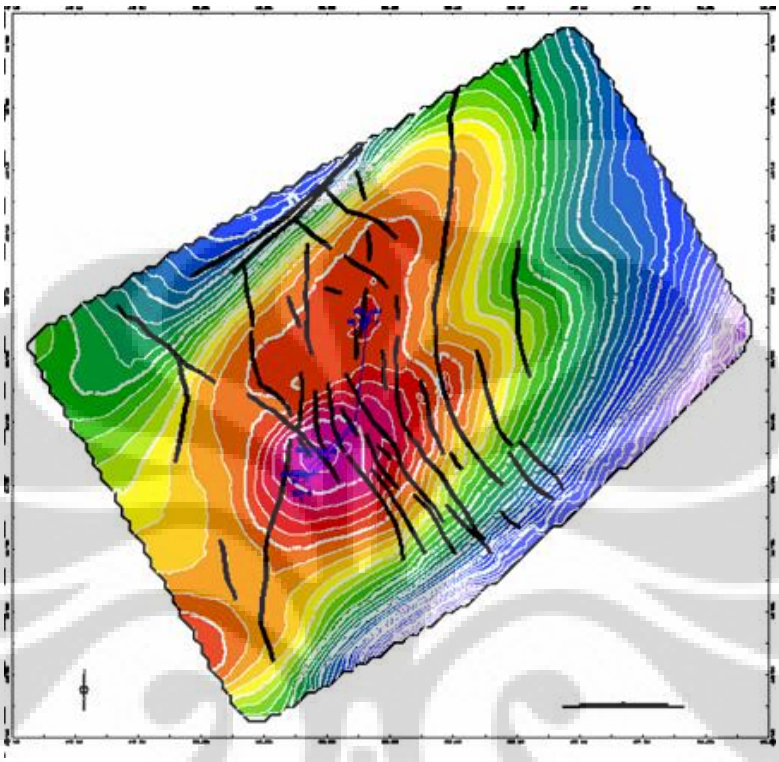

Figure 2.3 Top Upper Gabus (UG-1A) Structure map

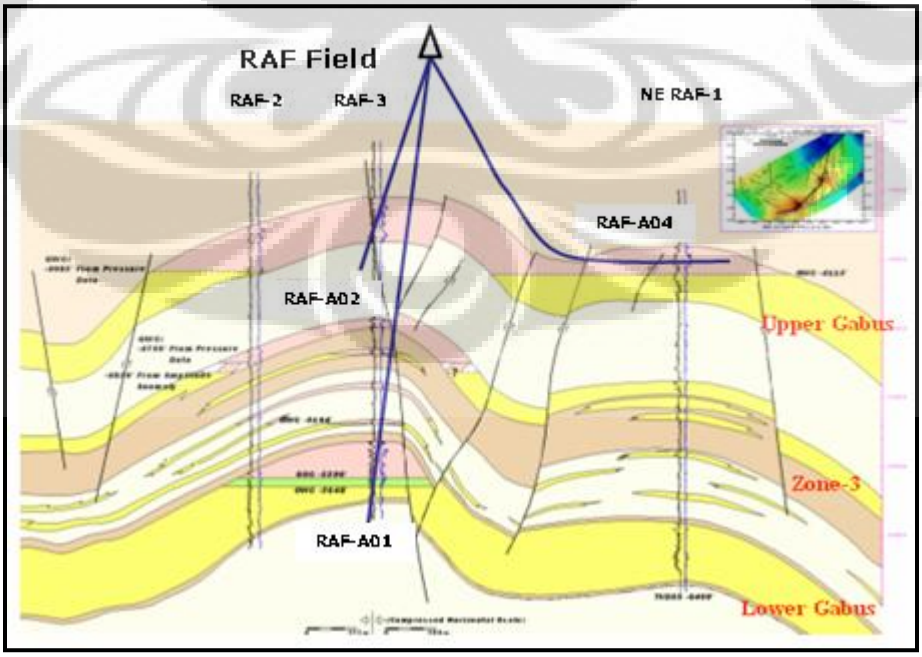

Figure 2.4 Shows hydrocarbon distribution over RAF field prior developed

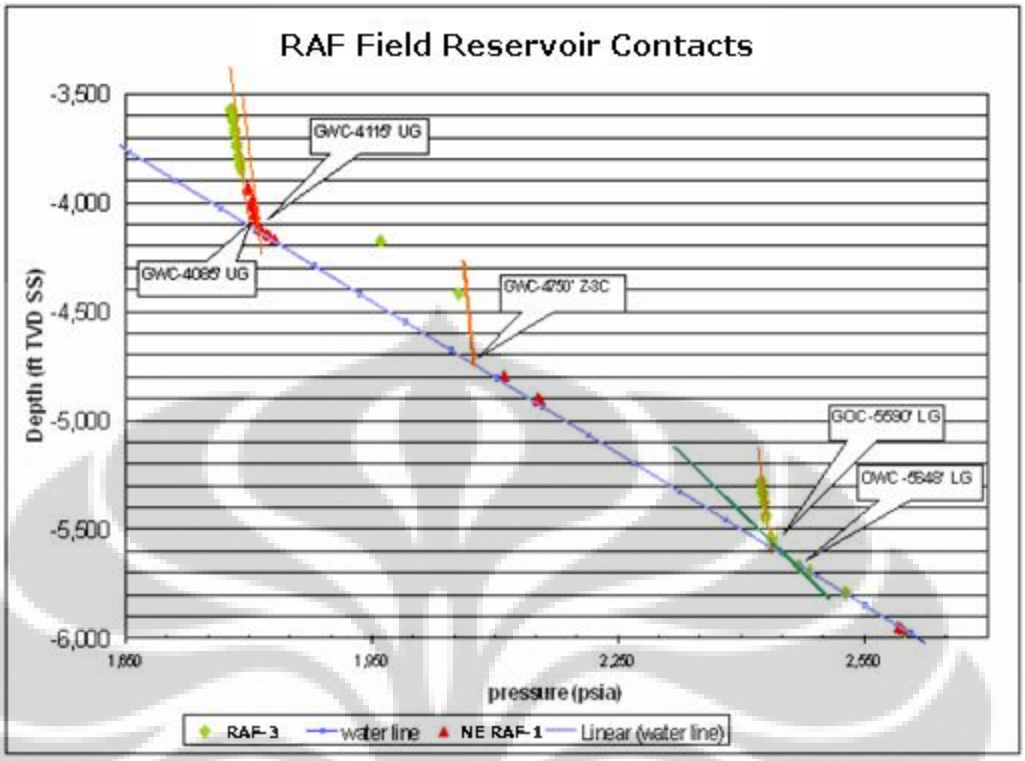

Figure 2.5 RAF-3 and NE RAF-1 Pressure Plots Showing Reservoir Fluid Contacts

2.3 Upper Gabus (UG) Reservoir Properties

Four hydrocarbon bearing sand reservoirs in Upper Gabus Formation are UG-1A, UG-1B, UG-1C, and UG Massive (figure 2.6). These sands have been penetrated by all the wells in the field. Conventional cores UG-1B were taken from RAF-2 well and sidewall cores were extensively taken both from RAF-2 and RAF-3 wells. In RAF structure, the main reservoir is UG-1A, UG-1B, and UG Massive Sand. While in NE RAF structure, gas bearing sands in Upper Gabus Formation is only UG-1B. NE RAF-1 exploration well was drilled on November 2002. Conventional cores were taken from UG-1B, sidewall cores were taken from UG-1A, UG-1B, UG-1C, and UG Massive from the well.

The Upper Gabus formation is interpreted to be deposited in a fluvial to deltaic environment; this can be observed from wire line logs and conventional cores. The zone is composed mainly fluvial channel deposit with mouth bar deposits. The fine to coarse grain size with moderate to well sorted texture, the fining-upward cycles, and also the

presence planar cross-bedding, low to high angle cross-bedding, trough cross-bedding, parallel bedding and climbing ripples suggest that the UG-1B and UG Massive sand were deposited in a low sinuosity to anastomosing channel system. The GR profiles also support this interpretation. Most of the UG 1A-1C and UG Massive sands show fining-upward to blocky log motives, with the exception of coarsening-upward UG-1A sands in NE RAF-1 well that suggest the sands were deposited as mouth bar deposits in a delta-front environment The Upper Gabus 1A, 1B and 1C comprised of alternating interbedded sandstone, shale, and minor siltstone. The sand is white to light gray quartz sandstone, very fine to coarse grain. It is moderately well cemented, slightly calcareous in some interval, common fine carbonaceous dissemination, occasionally fine coal in laminations, poor to fair visible porosity.

The Upper Gabus Massive sand is thick sand with shale interbedded at the bottom part of the Upper Gabus Formation. The sand is fairly homogeneous white to light grey, or light olive grey, with pale yellowish brown, clear to translucent quartz grains. It is typically varied from medium to coarse grain although occasionally fine grained, friable to loose, sub rounded to rounded and poor to moderate sorted. It is moderate to strongly cemented, with traces of carbonaceous material and non calcareous cement, very finely disseminated pyrite, chlorite, and lithic fragments. Porosity derived from cores indicates that these sands have a good primary porosity and secondary porosity.

A summary of petrophysical properties of RAF reservoirs can be seen in Table 2.2

		Petrophysical Log Analysis					Core Data		
Reservoir	Wells	Avg Gross Thickness (ft)	Avg Net Pay Thickness (ft)	Avg Net Pay to Gross (%)	Avg Por @ Pay (%)	Avg Sw @ Pay (%)	Avg Por (%)	Avg Perm (%)	Note
Upper Gabus: 1A,1B,1C	RAF-2,RAF-3, NE RAF-1	112	55	49	21	33	26	728	Core from UG-1B of NE RAF-1
UG Massive	RAF-2,RAF-3, NE RAF-1	187	29	15	20	51			

Table 2.2 RAF Petrophysical Properties Summary

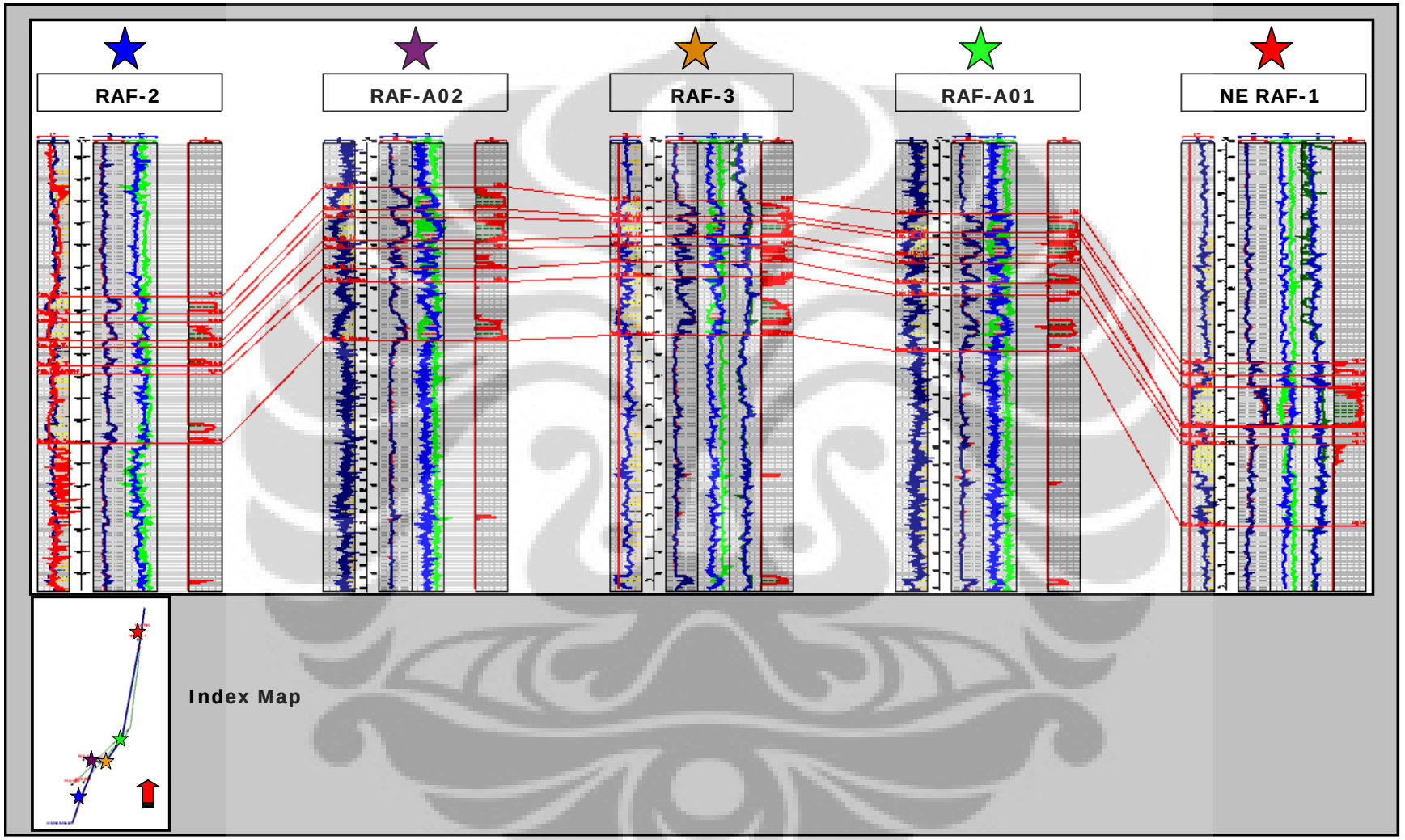

Figure 2.6 Well correlation shows Upper Gabus Formation: UG-1A, UG-1B, UG-1C and UG Massive

Chapter Three:
BACKGROUND THEORY

3.1 Seismic Reflection Theory

Seismic reflection theory covers a very wide topic; therefore below we will only discuss a bit, some basic seismic reflection theories that relate to the thesis topic and the method itself.

The fundamental concept of seismic exploration is to send into the earth a short time signal, which is then reflected back from a boundary between two units called reflector. The big advantage of the seismic method over other methods is fine horizontal resolution. The signals is transmitted through the earth as an elastic wave and bring back to the receiver kind of subsurface information such as geological structure, lithology and fluid through travel time, reflection amplitude and phase variation. A seismic reflection occurs whenever there is a change in acoustic impedance as a function of velocity (V) and density (ρ) which could be then interpreted as lithology contrast. At perpendicular incidence, that is, when ray path strikes a reflecting interface at right angle, the familiar basic equation of the reflection coefficient is:

$$r_i = \frac{\rho_{i+1} V_{i+1} - \rho_i V_i}{\rho_{i+1} V_{i+1} + \rho_i V_i} \qquad (1)$$

where:

ρ_i = density of layer ith

Vi = velocity of later ith

The signal received in a seismic trace is content of wiggle wave series. This seismic trace is assumed by convolution of wavelet of the source with the reflection series of the earth reflectors. Seismic wavelet itself is a clipped oscillation curve form like sinusoidal (Suprajitno, 2000).

In mathematical relationship this convolution can be written as:

$$\mathbf{S(t) = W(t) * RC(t) + n(t)} \quad (2)$$

where : S(t) = seismic trace, W(t) = seismic wavelet,
RC(t) = reflection coefficient, n(t) = noise

3.1.1 Compressional Velocity (Vp) and Shear Velocity (Vs)

As discussed above, the seismic wave is transmitted through the earth as an elastic wave. Commonly, based on the travel medium, elastic wave is classified as (1) **Body wave**, where the wave propagates through the body of the medium and (2) **Surface wave**, where the wave propagates along a boundary of the medium and the amplitude is weaken when going through the medium (Suprajitno, 2000). Body wave may be either P-wave (also called primary or compressional or longitudinal wave) or S-wave (also called shear or transversal wave). Surface wave may travel by several modes, the most common of which are Rayleigh waves, Love waves and Stoneley waves.

However in this section we will only focus to discuss the body waves: **P-wave**, in which the direction of particle motion is in the same direction as the wave movement and **S-wave**, in which the direction of particle motion is at right angles to wave movement (figure 3.1). Both of these waves have a certain velocity when they propagate through the earth and its value is depend on the traveled media elasticity. However, S-wave is typically slower (lower velocity) than P-wave and one thing that can be noted is S-wave can not travel in fluid medium. Compressional (V_P) and Shear velocity (V_S) can be simply presented as:

$$Vp = \sqrt{\frac{\lambda + 2\mu}{\rho}} = \sqrt{\frac{K + \frac{4}{3}\mu}{\rho}} \quad (3)$$

$$Vs = \sqrt{\frac{\mu}{\rho}} \quad (4)$$

dimana : $\boldsymbol{\lambda}$ **:** lambda coefficient = $\boldsymbol{K + 2/3\ \mu}$**,** (5)

$\boldsymbol{K}$ **:** bulk modulus, $\boldsymbol{\mu}$ **:** shear modulus,

$\boldsymbol{\rho}$ **:** density

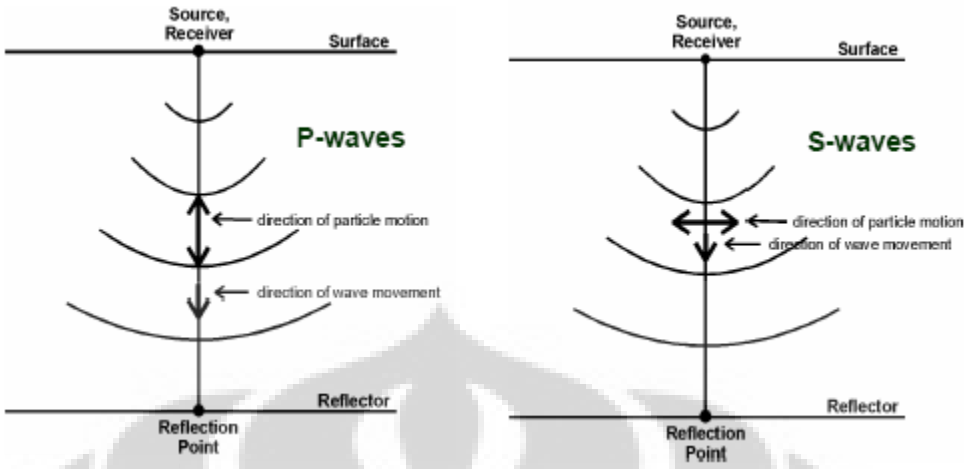

Figure 3.1 Illustration of particle movement trajectory of (a) P-wave and (b) S-wave

The ratio of V_P and V_S can be presented by Possion's Ratio (σ) as:

$$\sigma = \frac{\gamma - 2}{2\gamma - 2} \tag{6}$$

Where : $\gamma = \left(\frac{V_P}{V_S}\right)^2$ (7)

It is widely known that V_P/V_S can be used as lithology indicator (Avseth et al, 2005). Clay, if assumed isotropic is always having higher V_P/V_S ratio than sand. In carbonate, V_P/V_S can be used to discriminate limestone from dolomite. Later V_P/V_S, using AVO method can be also used as DHI (Direct Hydrocarbon Indicator) since V_S is not sensitive to fluid changing while V_P is sensitive to lithology and fluid changing which resulting changing in V_P/V_S.

3.1.2 Rigidity (μρ) and Incompressibility (λρ)

Based on equation (3) and (4) of the above section, mathematically those parameters, Vp and Vs, could be transformed to other rock physic parameters: Rigidity and Incompressibility.

$$V_P = \sqrt{\frac{\lambda + 2\mu}{\rho}} \quad \text{and} \quad V_S = \sqrt{\frac{\mu}{\rho}}$$

so $Z_S^2 = (\rho V_S)^2 = \mu\rho$ = Mu-Rho (Rigidity) (8)

and $Z_P^2 = (\rho V_P)^2 = (\lambda + 2\mu)\rho$ (9)

Then $\lambda\rho = Z_P^2 - 2Z_S^2$ = Lamda-Rho (Incompressibility) (10)

Mu-Rho or Rigidity can be described as the physical properties of rock matrix (changing in form) when it is given the stress. Rigidity is sensitive to rock matrix and not influenced by fluid therefore it can be used as a lithology indicator. The denser the rock matrix, the easier it gets to slide over each other then it is said that lithology has high rigidity value. Low rigidity values represent coal and or shales while sand or carbonates are characterized by high values. Lamda-Rho or Incompressibility is a measure of the physical response of the rock matrix and its interstitial fluids (changing in volume) for a given stress. The easier the medium are compressed, the lower the incompressibility value will be. This changing is more caused by changing in pore rather than changing in grain size. Lamda-Rho is a good indicator for lithology and pore fluid. Low incompressibility values are associated with gas sand (Goodway et al., 1997).

Table below is showing rock physic analysis presented by Goodway et al., 1997 indicating that λ/μ is the most sensitive to variation in rock properties going from shale to gas sand.

TABLE 1	Vp (m/s)	Vs (m/s)	ρ (g/cc)	Vp/Vs	$(Vp/Vs)^2$	σ	λ + 2μ	μ	λ	λ/μ
Shale	2898	1290	2.425	2.25	5.1	0.38	20.37	4.035	12.3	3.1
Gas Sand	2857	1666	2.275	1.71	2.9	0.24	18.53	6.314	5.9	0.9
Avg. Change	1.40%	25%	6.40%	27%	55%	45%	9.20%	44%	70%	110%

(moduli λ, μ are in GPa's)

Table 3.1 Rock physics analysis using Lame' parameter (Goodway et al., 1997)

3.1.3 Density

Density in a simple way can be described as ratio between mass (kg) to volume (m^3). Density is used in Vp, Vs and impedance equation where they all influence the response of seismic wave. The effect of density can be modeled in Wyllie equation:

$$\rho_{sat} = \rho_m(1-\phi) + \rho_w S_w \phi + \rho_{hc}(1-S_w)\phi \qquad (11)$$

where:

ρb = bulk density ρm = matrix density
ρf = fluid density φ = porosity
Sw = water saturation ρw = water density (close to 1 g/cm^3)
ρhc = hydrocarbon density.

Figure 3.2 Illustrate that density of reservoir decrease dramatically in gas zone compares to in oil zone. This character is important in seismic interpretation for the reservoir.

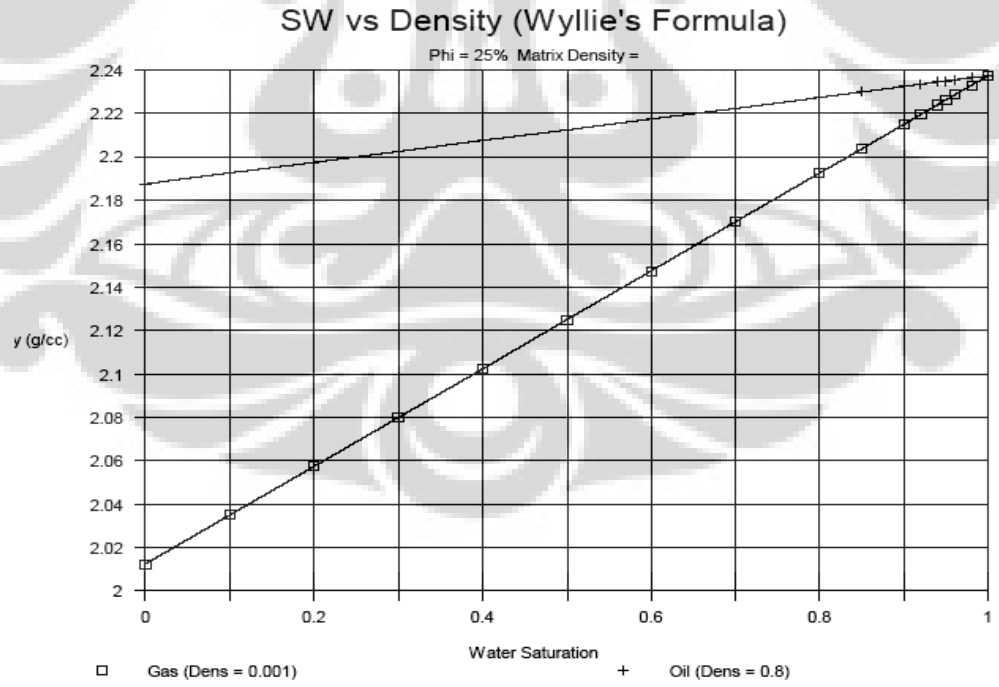

Figure 3.2 Sw vs Density. Application of Wyllie equation in oil and gas reservoir (Russell, 1999)

3.2 Amplitude Variation with Offset (AVO)

Initially the AVO method was addressed as the technique to validate the amplitude anomaly in seismic associated with gas presence in a reservoir. This anomaly appears as the result of reflection coefficient decrease drastically in gas reservoir compare to surrounding layers. This phenomenon is called "bright spot". In practical, not all bright spot will show gas presence since coal, porous or fractured layer, salt, conglomerate, turbidite and tuning effect of thin layer can also showing this anomaly (Pendrel et al., 2000). AVO was developed to reduce this ambiguity.

The basic principle of AVO was started from the anomaly of the increasing amplitude of reflection signal to the increasing offset, the distance from seismic source to receiver when seismic wave is reflected by layer contain gas. This offset relate to incidence angle of reflection surface. The bigger offset, the bigger incidence angle will be. AVO is caused by energy partition at the surface reflector. Some of the energy are reflected and some are transmitted. When the wave is coming to layer boundary at the non-zero incidence angle then P wave is converted to S wave. The amplitude of reflected and transmitted energy depends on rock physics of surface reflector. As the consequence, reflection coefficient becomes a function of compressional velocity (Vp), Shear velocity (Vs), density of each layer and incidence angle (θ_1). Therefore there are 4 curve that can derived: P wave reflected amplitude, P wave transmitted amplitude, S wave reflected amplitude and S wave transmitted amplitude as it shown in figure 3.3 below.

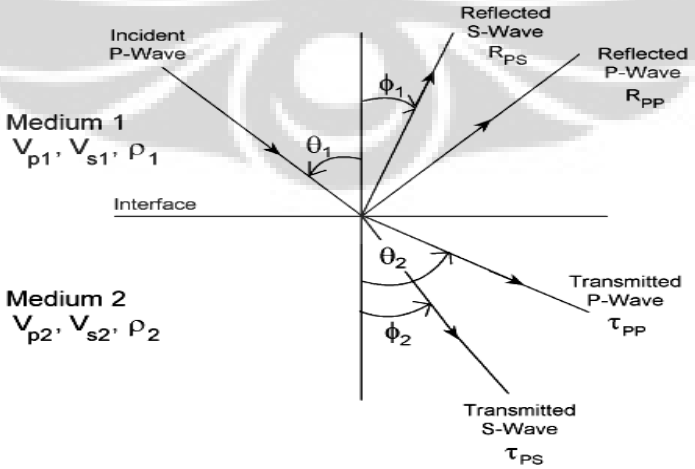

Figure 3.3 Seismic energy partition at surface reflector (Russel, 1999)

The first AVO equation was introduced by Zoeppritz, 1919 (opcite Aki et al., 2002) which described that reflection and transmission coefficient as the function of Vp, Vs, density and incidence angle on elastic media. The equation can be written as:

$$\begin{bmatrix} R_P(\theta_1) \\ R_S(\theta_1) \\ T_P(\theta_1) \\ T_S(\theta_1) \end{bmatrix} = \begin{bmatrix} -\sin\theta_1 & -\cos\phi_1 & \sin\theta_2 & \cos\theta_2 \\ \cos\theta_1 & -\sin\phi_1 & \cos\theta_2 & -\sin\phi_2 \\ \sin 2\theta_1 & \frac{V_{P1}}{V_{S1}}\cos 2\phi_1 & \frac{\rho_2 {V_{S2}}^2 V_{P1}}{\rho_1 {V_{S1}}^2 V_{P2}}\cos 2\phi_1 & \frac{\rho_2 V_{S2} V_{P1}}{\rho_1 {V_{S1}}^2}\cos 2\phi_2 \\ -\cos 2\phi_1 & \frac{V_{S1}}{V_{P1}}\sin 2\phi_1 & \frac{\rho_2 V_{P2}}{\rho_1 V_{P1}}\cos 2\phi_2 & \frac{\rho_2 V_{S2}}{\rho_1 V_{P1}}\sin 2\phi_2 \end{bmatrix}^{-1} \begin{bmatrix} \sin\theta_1 \\ \cos\theta_1 \\ \sin 2\theta_1 \\ \cos 2\phi_1 \end{bmatrix} \quad (12)$$

where :

$R_P(\theta_1)$ = Reflected P-wave amplitude — θ_1 = P-wave reflection angle

$R_P(\theta_2)$ = Reflected S-wave amplitude — θ_2 = P-wave refraction angle

$T_p(\theta_1)$ = Transmitted P-wave amplitude — ϕ_1 = S-wave reflection angle

$T_S(\theta_2)$ = Transmitted S-wave amplitude — ϕ_2 = S-wave refraction angle

Vp = P-wave velocity — ρ = density

Vs = S-wave velocity

Aki, Richard and Frasier then approximated the Zoeppritz equation into 3 terms. First term incorporate density, second incorporate Vp and third incorporate Vs.

$$R(\theta) = a\frac{\Delta\alpha}{\alpha} + b\frac{\Delta\rho}{\rho} + c\frac{\Delta\beta}{\beta} \quad (13)$$

where:

$a = 1/(\cos^2\theta) = ½ + \tan^2\theta$; $b = 0.5 - [(2V_S^2/V_P)\sin^2\theta]$; $c = -(4V_S^2/V_P^2)\sin^2\theta$;

$V_P = (V_{P1} + V_{P2})/2$; $V_S = (V_{S1} + V_{S2})/2$; $\rho = (\rho_1 + \rho_2)/2$; $\Delta V_P = V_{P1} - V_{P2}$;

$\Delta V_S = V_{S1} - V_{S2}$; $\Delta\rho = \rho_1 - \rho_2$; $\theta = (\theta_i + \theta_t)/2$; $\theta_t = \arcsin[(V_{P2}/V_{P1})\sin\theta_i]$

The P-wave reflection coefficient formulation of Zoeppritz was then simplified by Shuey, 1985 (opcite Aki et al., 2002):

$$R(\theta) = R_p + \left(R_p A_0 + \frac{\Delta\sigma}{(1-\sigma)^2}\sin^2\theta + \frac{1}{2}\frac{\Delta\alpha}{\alpha}\left(\tan^2\theta - \sin^2\theta\right)\right) \qquad (14)$$

where: $\sigma = \frac{(\sigma_1 + \sigma_2)}{2}$; $A_0 = B - 2(1+B)\frac{1-2\sigma}{1-\sigma}$ and $B = \frac{\Delta\alpha/\alpha}{\Delta\alpha/\alpha + \Delta\rho/\rho}$

with : σ = average Poisson ratio

$\Delta\sigma = \sigma_2 - \sigma_1$

α = average Vp = $\frac{\alpha_1 + \alpha_2}{2}$

$\Delta\alpha = \alpha_2 - \alpha_1$

θ = average incidence angle and transmitted angle = $\frac{\theta_1 + \theta_2}{2}$

ρ = average formation density = $\frac{\rho_1 + \rho_2}{2}$

$\Delta\rho = \rho_2 - \rho_1$

From the final result, it can be concluded that AVO response is strongly influenced by R_P at low angle and also influenced by $\Delta\sigma$ at fairly high angle. Qualitative AVO analysis is done in common-mid-point-gather (or super-gather or common offset gather etc). Every amplitude value from every offset in gather simply linearly regressed to get simplified relationship between amplitude vs offset. From this point we get the AVO attribute: **Intercept** and **Gradient** which describe relationship between amplitude response and incidence angle.

Zoeppritz and Shuey equation are the function of incidence angle, however seismic is recorded as the function of offset distance. Therefore it need conversion from offset distance to angle of incidence. Figure 3.4 and 3.5 show simple approach using straight ray.

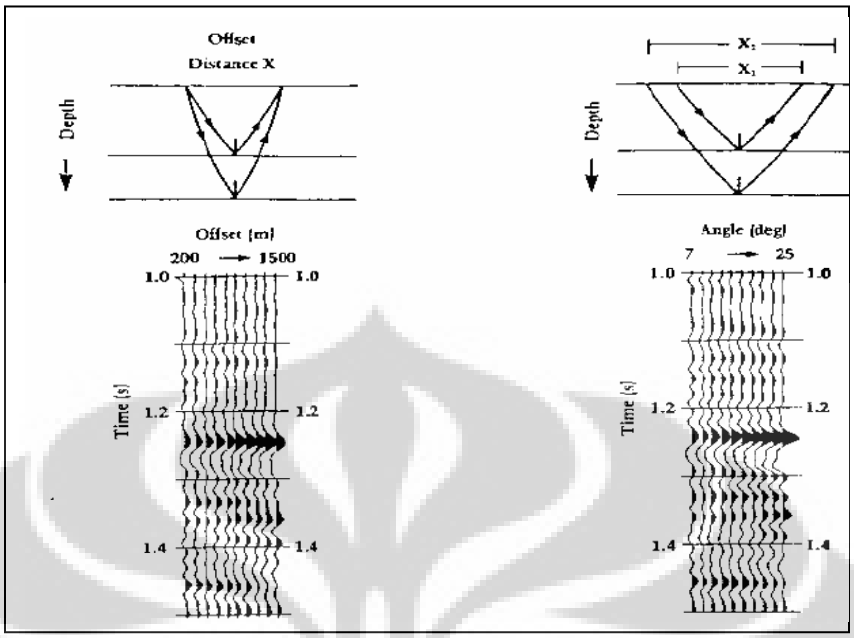

Figure 3.4 AVO response (a) and its transformation to AVA (Amplitude versus Angle) (b) (Russel, 1999)

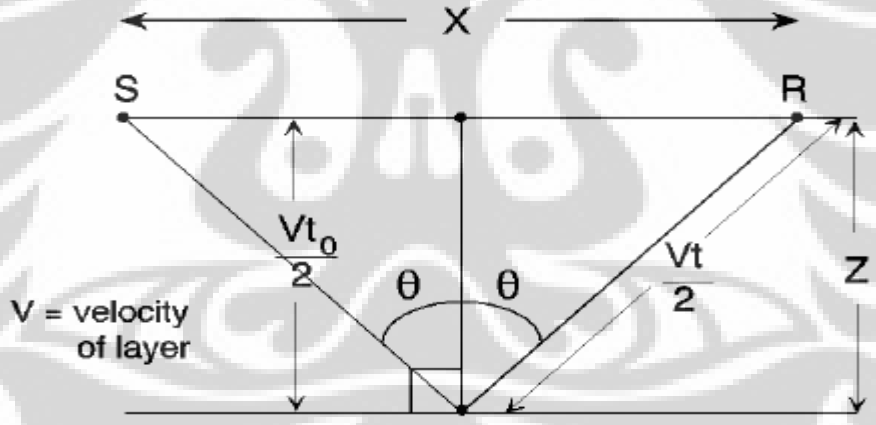

Figure 3.5 Geometry of seismic ray track for one shot-receiver on media with constant velocity (Russel, 1999)

Relationship between offset and angle can be presented as:

$$\tan \theta = X/2Z \qquad (15)$$

where: θ = angle

X = offset

Z = depth

If we know the velocity of the media, we can then write the equation as:

$$Z = V.t_o /2 \quad (16)$$

Where: V = velocity (RMS or average)

T = time at zero-offset

By substituting equation (18) into (21), we will get:

$$\tan \theta = X/V.t_o \quad (17)$$

So

$$\theta = \tan^{-1}[X/V.t_o] \quad (18)$$

Using this equation, offset can be transformed into angle.

Although AVO analysis is based on increasing reflection amplitude versus offset, however there is a maximum offset which should fit to critical angle. When the angle exceeds the critical angle, the reflected signal behavior will not follow the reference theorem in AVO analysis.

3.3 AVO Classification

Rutherford and Williams,1989 (opcite Sukmono, 2002) devided three (3) classes of gas sandstone which are: Class-1, *high impedance gas-sandstone* ; Class-2, *near zero contrast gas-sandstone* ; Class-3, *low impedance gas* sandstone. Castanga (1998) then introduced sandstone Class-4 from AVO crossplot based on Rutherford and Williams classification (figure 3.6)

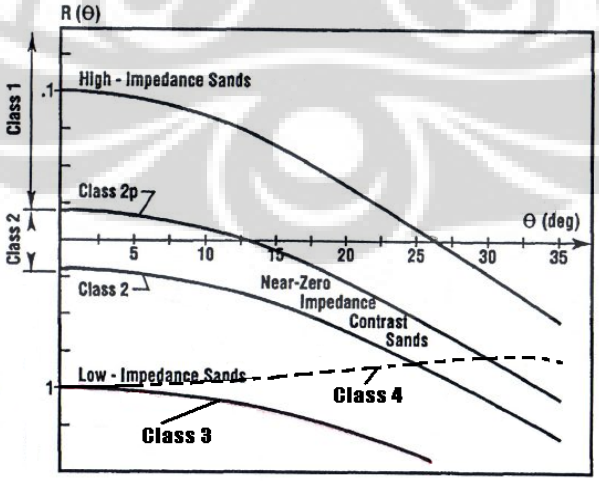

Figure 3.6 Plot of reflection coefficient versus angle of incidence for gas layer top sand based on Rutherford and Williams (1989) and Castagna (1998) classification

Below is the description of 4 (four) AVO classes of gas-sandstone classification:

1. **Class-1 Anomaly - *High Acoustic Impedance Sandstone with decreasing AVO***
   Typically class-1 sandstone has relatively high acoustic impedance compare to the seal layer which usually shale. Boundary between shale and sand will have high reflection coefficient (R_0). The zero-offset reflection coefficient on this class-1 sandstone will have a positive value and along with offset increase, the absolute amplitude value will decrease. Amplitude changing versus offset is known as Gradient where gradient for class 1 usually is higher than gradient class 2 and 3.
2. **Class-2 Anomaly – *Near Zero Acoustic Impedance Contrast Sandstone***
   Class-2 sandstone has a close acoustic impedance value to its seal layer. Typically this sandstone is compact and well consolidated. Class-2 gradient is usually high but still lower than class 1 gradient, where going farther from the offset, amplitude value is getting smaller. Class-2 sandstone is divided into 2: **Class-2** and **Class-2p**. Class-2p has a positive reflection coefficient at zero offset and normally reversed polarity occurs at near offset. While Class-2 sandstone has zero reflection coefficient at zero offset.
3. **Class-3 Anomaly - *Low Accoustic Impedance Sandstone with increasing AVO***
   Class-3 sandstone has lower acoustic impedance compare to its seal layer. Normally this sandstone is less compact and less consolidated. On seismic stack, Class-3 sandstone typically has large amplitude value and high reflection coefficient at all offset, its gradient is usually high but still lower than Class-1 and Class-2. Reflection coefficient at normal incidence angle is always negative.
4. **Class-4 Anomaly - *Low Accoustic Impedance Sandstone with decreasing AVO***
   Class-4 sandstone is usually marked by anomaly with positive reflection coefficient as offset increase. It usually occurs on porous sandstone which bounded by high velocity lithology, such as: hard shale (eg. Siliceous or calcareous), siltstone, tighly cemented sand or carbonate.

3.4 Seismic Inversion

There are two ways of geophysical modeling: Forward modeling and Inverse modeling (figure 3.7). Forward modeling is calculating or predicting geophysical response from earth model while inverse modeling is calculating or predicting earth model from geophysical response. Therefore Seismic Inversion is defined as geological subsurface modeling technique using seismic data as input and well data as control (Sukmono, 2002). The output model by this seismic inversion is impedance model such as AI (Z_P), SI (Z_S) which are parameters of lithology layer but not the parameter on lithology boundary as reflection coefficient. Seismic inversion is much easier understandable and easier to interpret. Impedance model can also be correlated quantitatively with well reservoir rock properties such as porosity, water saturation etc. If it is well correlated then the inversion result can be used to map those well reservoir rock properties on the seismic data to get better understanding its lateral prediction.

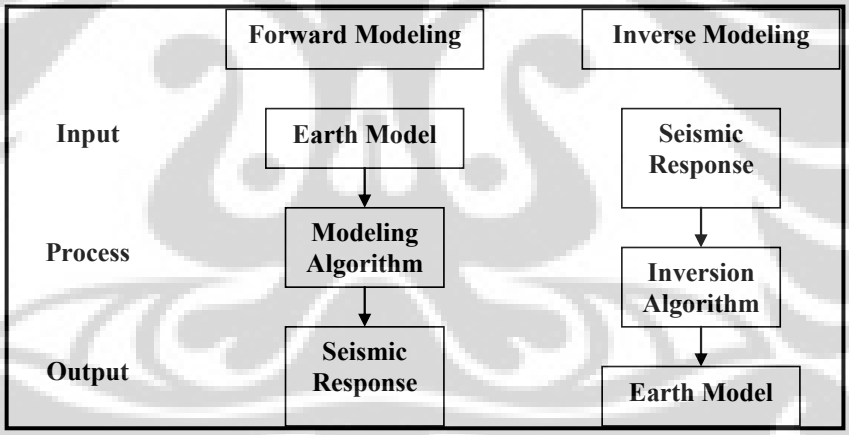

Figure 3.7 Two ways of geophysical modeling

Basically seismic inversion method is a process of transforming seismic amplitude value to impedance value. This is done by de-convolution process which transforms seismic trace to earth's reflectivity. Based on type of seismic data used, seismic inversion method can be divided into 2 types (Russel, 1999) (figure 3.8), they are: Post-stack seismic inversion and Pre-stack seismic inversion. Post-stack seismic data assumed that seismic amplitude is only represented by $R_{(0)}$, therefore Post-stack seismic inversion can only produce AI (Z_P). While Pre-stack seismic data still contains $R_{(\theta)}$

information, so Pre-stack seismic inversion can produce parameters AI (Z_P), SI (Z_S) and its derivatives such as: V_P/V_S, Lamda-rho, Mu-rho etc. However in this study, we will not discuss post-stack inversion method, we will later discuss pre-stack inversion method, particularly Seismic Simultaneous Inversion method in more detail.

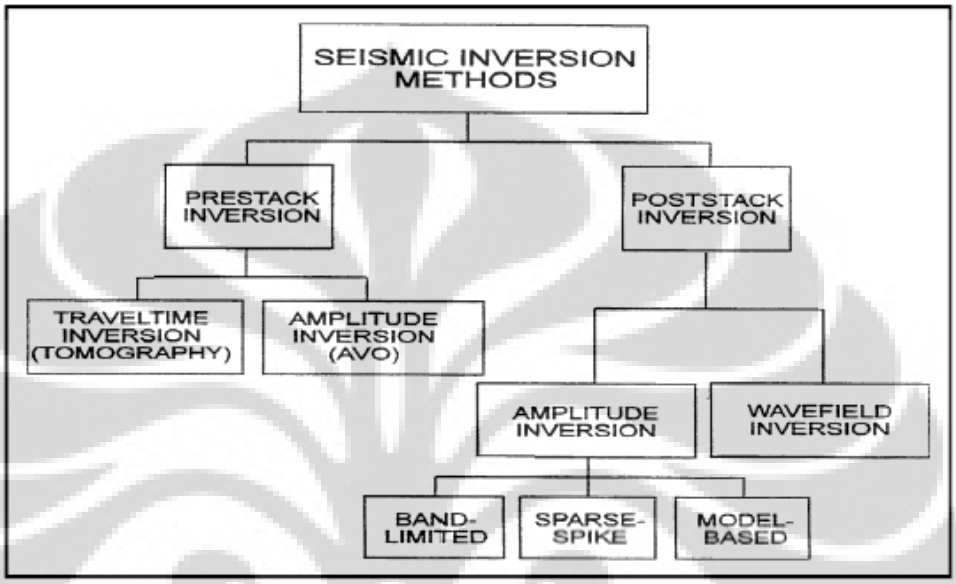

Figure 3.8 Seismic Inversion methods (Russel, 1988)

3.4.1 Acoustic Impedance (AI or P-impedance or Z_P)

Seismic trace is a convolution of earth's reflectivity (RC) with seismic wavelet plus noise component in time domain. It can be written as:

$$\mathbf{S(t) = W(t) * RC(t) + n(t)} \quad (19)$$

Where: S(t) = seismic trace, W(t) = wavelet seismic,
RC(t) = earth's reflectivity, n(t) = *noise*.

If noise is assumed zero, then:

$$\mathbf{S(t) = W(t) * RC(t)} \quad (20)$$

RC or reflection coefficient is a function of impedance contrast in earth, therefore RC is a value which represent boundary of two layers that have different impedance. Mathematically, RC on layer boundary can be defined as:

$$RC_i = \frac{AI_{i+1} - AI_i}{AI_{i+1} + AI_i} \tag{21}$$

Where $i = i^{th}$ layer and over the (i^{th} +1) layer

So that AI value can be estimated from reflection amplitude. The bigger amplitude, the more contrast the AI. AI is the multiplication between density and P-wave velocity.

$$AI = \rho \times V_p , \tag{22}$$

Where ρ = density,

V_p = P-wave velocity.

AI is one of rock physic parameters which influenced by type of lithology, porosity, fluid content, depth, pressure and temperature. That is why AI can be used to identify lithology, porosity and hydrocarbon indicator and since velocity has bigger order than density, so AI value is more controlled by seismic velocity rather than density. Figure 3.9 shows some of factors that influenced seismic velocity.

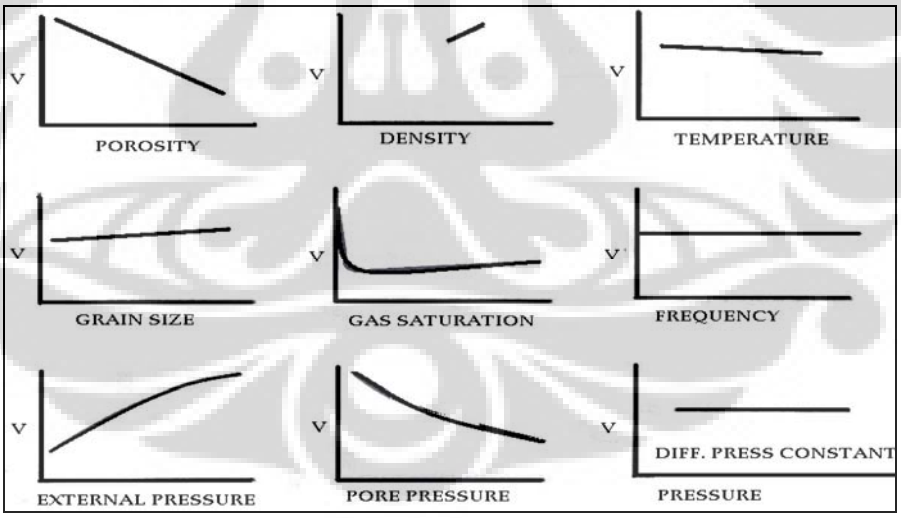

Figure 3.9 Some of factors that influenced seismic velocity (Hiltermann, 1977, opcite, Sukmono, 2002)

However characterization based on AI has some limitations in distinguish lihology and fluid effect. The low AI value due to hydrocarbon fluid is often overlapping with low AI of lithology effect.

3.4.2 Shear Impedance (SI or S-impedance or Z_S)

In general shear impedance is just the same with acoustic impedance, the only different is the velocity used for the multiplication with density is S-wave velocity (V_S). It can be written as:

$$\mathbf{SI = \rho\, Vs} \qquad (28)$$

where : SI : shear impedance

ρ : density

Vs : S-wave velocity

Since S-wave only measures the rigidity of rock matrix, therefore the fluid in the reservoir is undetectable. This wave will only pass through the solid medium, however when S-impedance is combined analysis with P-impedance, it can be used to predict and estimate the lithology and fluid content changing.

3.5 Seismic Simultaneous Inversion

The AVO method has become a foundation in Seismic Simultaneous Inversion and other AVO Inversion technique development such as Elastic inversion and other independent inversion. It is called independent inversion, because the first step is to extract independently estimation of the zero-offset P (R_{P0}) and S reflectivity (R_{S0}) from the seismic gathers or partial stacks. While Simultaneous inversion is considered as dependent inversion since it work dependently and simultaneously when estimate P and S impedance.

Figure 3.10 shows the typical workflow of simultaneous inversion by Fugro-Jason. In this workflow, simultaneous inversion is done by combining partial seismic angle stack simultaneously with low frequency model and convoluted by wavelets which extracted from each angle stack to obtain angle dependent quantities such as P-Impedance, S- Impedance and Density. Later these quantities can be transformed to V_PV_S ratio, Lambda Rho and Mu Rho.

This method is actually the improvement to resolve the problem in the angle independent calculation which does not use rock property relationships between variables for the background case. Problem also appears in the angle independent calculation when combining the data with the different frequency as it will create noise.

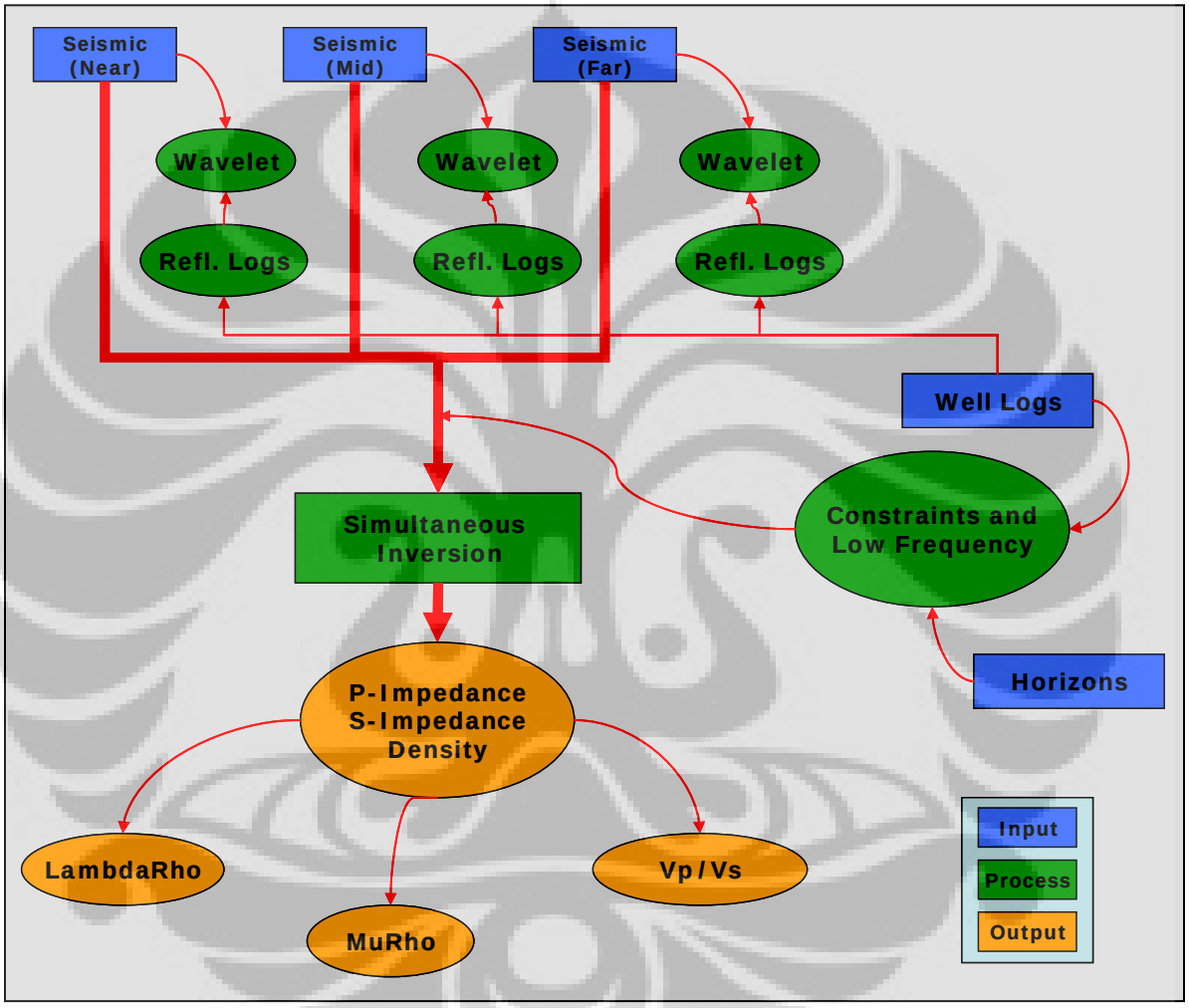

Figure 3.10 Shows the typical workflow of simultaneous inversion by Fugro-Jason

Started from Aki Richard equation (13) above, Fatti et al (1994) re-formulate the equation to a function of zero-offset P-wave reflectivity (R_{P0}), zero-offset S-wave reflectivity (R_{S0}) and density reflectivity (R_D) in the form.

$$\mathbf{R_{PP}(\theta) = c_1 R_{P0} + c_2 R_{S0} + c_3 R_D} \quad (29)$$

Where:

$$c_1 = 1 + \tan^2\theta$$
$$c_2 = -8\gamma^2 \sin^2\theta$$
$$c_3 = -\frac{1}{2}\tan^2\theta + 2\gamma^2 \sin^2\theta$$
$$\gamma = \frac{V_S}{V_P}$$

and

$$R_P = \frac{1}{2}\left[\frac{\Delta V_P}{V_P} + \frac{\Delta\rho}{\rho}\right]$$
$$R_S = \frac{1}{2}\left[\frac{\Delta V_S}{V_S} + \frac{\Delta\rho}{\rho}\right]$$
$$R_D = \frac{\Delta\rho}{\rho}.$$

And R_{PP} = total reflectivity, R_P = the P-wave reflectivity,
R_S = S-wave reflectivity, R_D = density reflectivity,
V_P = the P-wave velocity, V_S = S-wave velocity and
ρ = the density.

Russel et al. (2005) extended the work of Fatti et al. and developed a new approach that allows us to invert directly from reflectivity for *P*-impedance, S-impedance, and density. It started by defining a new variable $L_P = \ln(Z_P)$, which is the normal log of the acoustic Impedance, Z_P.

$$\mathbf{R_P(i) = 1/2\,[L_P(i+1) - L_P(i)]} \quad (30)$$

Or written in the matrix as follows:

$$\mathbf{R_P = (1/2)DL_P} \text{ or}$$

$$\begin{bmatrix} R_P(1) \\ R_P(2) \\ \vdots \\ R_P(N) \end{bmatrix} = \frac{1}{2}\begin{bmatrix} -1 & 1 & 0 & \cdots \\ 0 & -1 & 1 & 0 \\ 0 & 0 & -1 & 1 \\ 0 & 0 & 0 & \cdots \end{bmatrix}\begin{bmatrix} L_P(1) \\ L_P(2) \\ \vdots \\ L_P(N) \end{bmatrix} \quad (31)$$

Then wavelet effect is added in matrix equation:

$$\mathbf{T = W R_P} \quad \text{or}$$

$$\begin{bmatrix} T(1) \\ T(2) \\ \vdots \\ T(N) \end{bmatrix} = \frac{1}{2} \begin{bmatrix} W_1 & 0 & 0 & \cdots \\ W_2 & W_1 & 0 & \cdots \\ W_3 & W_2 & W_1 & \cdots \\ 0 & W_3 & W_2 & \cdots \end{bmatrix} \begin{bmatrix} -1 & 1 & 0 & \cdots \\ 0 & -1 & 1 & 0 \\ 0 & 0 & -1 & 1 \\ 0 & 0 & 0 & \cdots \end{bmatrix} \begin{bmatrix} L_P(1) \\ L_P(2) \\ \vdots \\ L_P(N) \end{bmatrix} \qquad (32)$$

Where T = the seismic trace

W = the seismic wavelet

The same operation is applied for the $L_S = \ln (Z_S)$ and $L_D = \ln (Z_D)$ where Z_S is the S-Impedance and Z_D is the density. Now Aki-Richards equation can be written as follows:

$$\mathbf{T(\theta) = (1/2)\, c_1 W(\theta)\, DL_P + (1/2)\, c_2\, W(\theta)\, DL_S + c_3\, W(\theta)\, DL_D} \qquad (33)$$

In the above equation (33), it model seismic trace, T on the θ angle as a function of impedance and density. This equation is also possible to implement for different wavelet with different angle.

To estimate P-Impedance, S-Impedance and density, it should be considered the fact that the density and impedance related to one another. The equation is expected representing the wet trend by assuming that the wet conditions can be modeled as the constant V_P/V_S ratio:

$$\mathbf{V_P / V_S = \gamma = constant}$$

$$\mathbf{\rightarrow \ln (Z_S) = \ln (Z_P) + \ln (\gamma)} \qquad (34)$$

Then by assuming Gardner equation (Russel et al., 2005) connects between the density and P-Impedance:

$$\rho = a V_P^{\,b}$$

$$\rightarrow \ln(\rho) = \frac{b}{1+b} \ln(Z_P) + \frac{\ln(a)}{1+b} \qquad (35)$$

where ρ = density, V_P = the P-wave velocity, a and b = constant.

From two assumptions above, it was then revealed that there are the linier relationships between ln Z_P (L_P) and ln Z_S (L_S) and between L_P and ln ρ (L_D) as it is expressed at the following equation:

$$\mathbf{\ln (Z_S) = k \ln (Z_P) + kc + \Delta L_S} \quad (36)$$

$$\mathbf{\ln (Z_D) = m \ln (Z_P) + mc + \Delta L_D} \quad (37)$$

where the coefficients k, kc, m, and mc will be determined by analyzing the well log data. Figure 3.10 illustrate the relationship between ln (Z_P) vs ln (Z_S) and ln (Z_P) vs ln (Density) of the well log data. The regression coefficient obtained by drawing a straight line on the interesting trend of the data. The deviations away from this straight line, ΔL_D and ΔL_S, are the desired fluid anomalies.

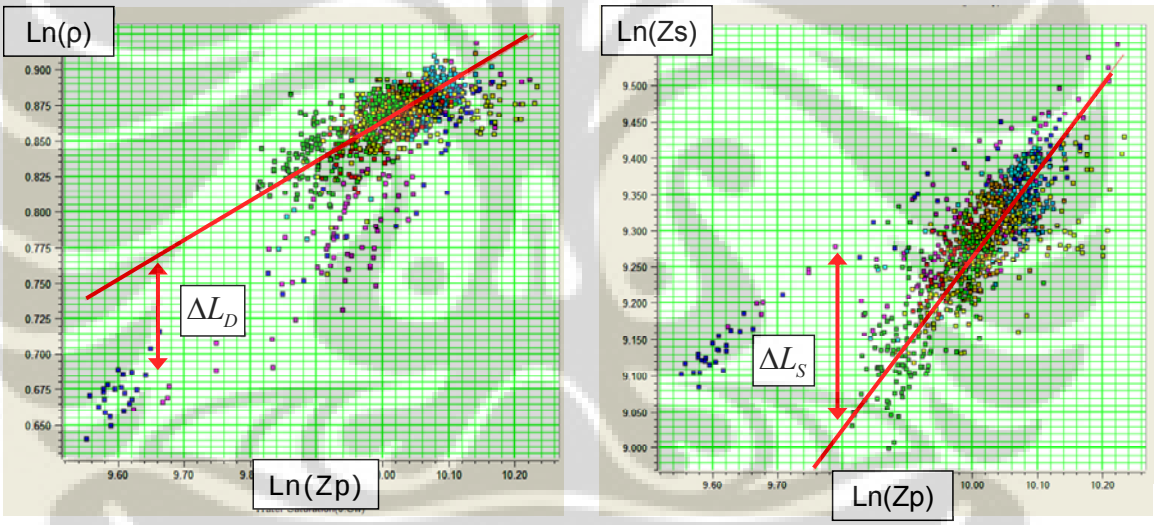

Figure 3.11 Crossplots of (a) ln(Z_D) vs ln(Z_P) and (b) ln(Z_S) versus ln(Z_P) where, in both cases, a best straight line fit has been added.

Next by substituting equation (36) and (37) into equation (33), Aki-Richard equation becomes:

$$T(\theta) = \tilde{c}_1 W(\theta) D L_P + \tilde{c}_2 W(\theta) D \Delta L_s + \tilde{c}_3 W(\theta) D \Delta L_D \quad (38)$$

where:

$\tilde{c}_1 = (½)c_1 + (½)kc_2 + mc_3$

$\tilde{c}_2 = (½)c_2$

W(θ= wavelet at angle θ

D = Derivative operator

$L_P = \ln (Z_P)$

In the matrix form, with the assumption the number of trace is N from various angles, the equation present as:

$$\begin{bmatrix} T(\theta_1) \\ T(\theta_2) \\ \vdots \\ T(\theta_N) \end{bmatrix} = \begin{bmatrix} \tilde{c}_1(\theta_1) W(\theta_1) D & \tilde{c}_2(\theta_1) W(\theta_1) D & \tilde{c}_3(\theta_1) W(\theta_1) D \\ \tilde{c}_1(\theta_2) W(\theta_2) D & \tilde{c}_2(\theta_2) W(\theta_2) D & \tilde{c}_3(\theta_2) W(\theta_2) D \\ \vdots & \vdots & \vdots \\ \tilde{c}_1(\theta_N) W(\theta_N) D & \tilde{c}_2(\theta_N) W(\theta_N) D & \tilde{c}_3(\theta_N) W(\theta_N) D \end{bmatrix} \begin{bmatrix} L_P \\ \Delta Ls \\ \Delta L_D \end{bmatrix} \quad (39)$$

Additionally, initial guess is determined and incorporated within the equation:

$$\begin{bmatrix} L_P & \Delta LS & \Delta L_D \end{bmatrix}^T = \begin{bmatrix} \log(Z_P) & 0 & 0 \end{bmatrix}^T \quad (40)$$

Finally, a reliable P-impedance, S impedance and density can be estimated:

$Z_P = \exp (L_P)$

$Z_S = \exp (kL_P + k_c + \Delta L_S)$

$\rho = \exp (mL_P + m_c + \Delta L_P)$

Chapter Four:
METHODOLOGY AND DATA PROCESSING

In general, the workflow used for this study to accomplish the objectives is summarized in figure (4.1). In a series, the workflow of this study and its steps in data processing can be listed as follows:

1. Data Preparation
2. Feasibility study
3. Well Seismic Tie and Wavelet Estimation
4. Horizon and Fault Interpretation
5. Low Frequency Model
6. Pre-Inversion QC Analysis
7. Simultaneous Inversion
8. Analysis and Interpretation

4.1 Data Preparation

The first thing in this step is to select and collect the required well and seismic data and other supported documents such as final well report, field study report and or published paper related to RAF Field. Next, prepare the data by QC'ing the data validity such well header, directional survey, time-depth data, top markers, logs, seismic survey and data etc and load them into database system which are Landmark-OpenWorks and HRS-GeoView.

4.1.1 Well Data

As it mentioned in Chapter-1 and summarized in Table 1.1, there are 7 wells located at RAF Field: 5 wells are located at RAF stucture and 2 wells are located at NE RAF structure. Based on well class, 4 wells are exploration wells: RAF-1, RAF-2, RAF-3, NE RAF-1 and 3 development wells: RAF-A01, RAF-A02 and RAF-A04.

However among those wells, 2 wells will not be used in this study: RAF-1, this well has only data up to 3800 ft due to drilling problem and RAF-A04, instead of this well has no both P and S sonic log and time-depth data, this well is a horizontal well which experienced having difficulty in calculation and display.

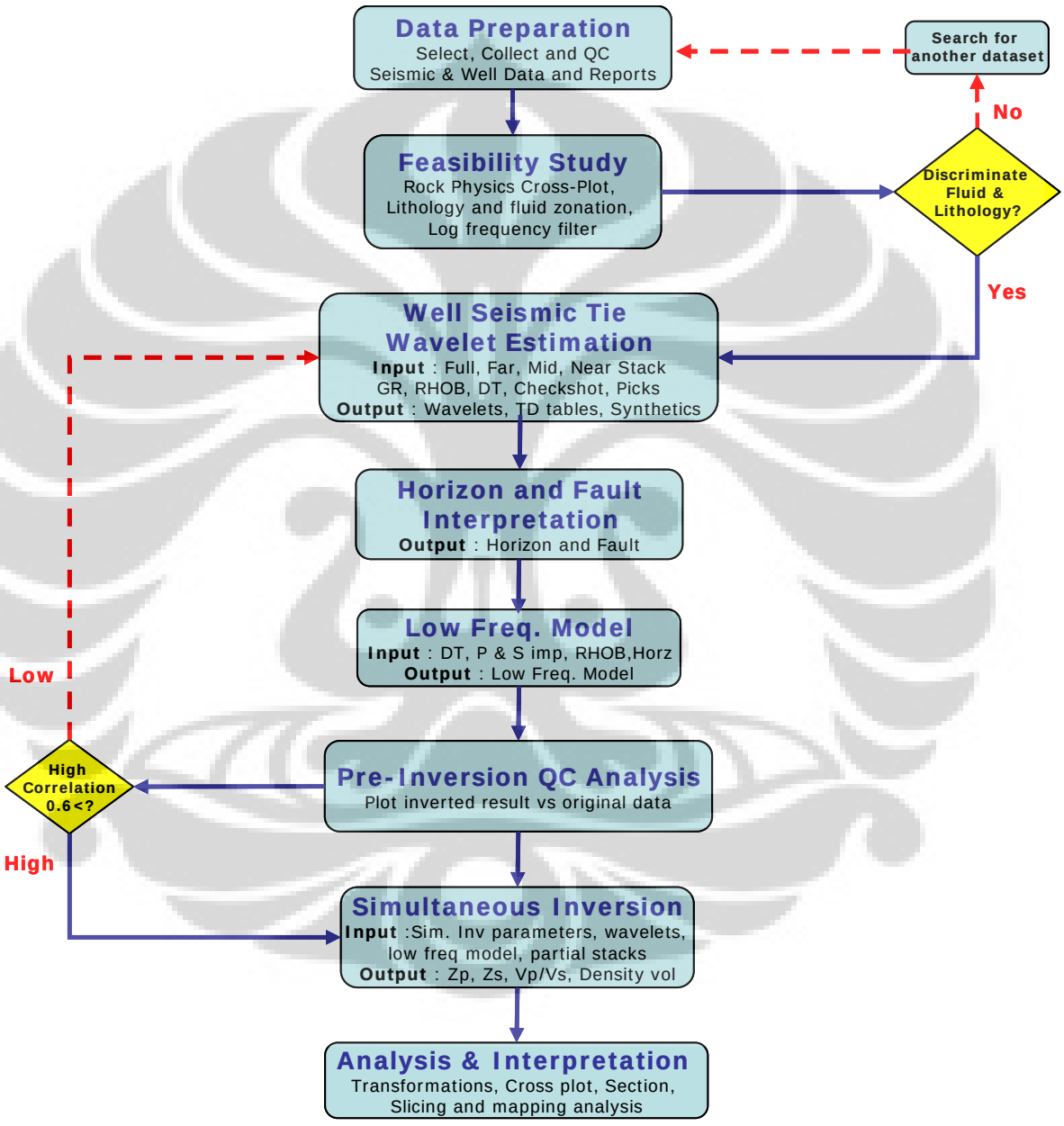

Figure 4.1 General workflow used for the study

The method of this study requires well data to have: both Compressional (P) and Shear (S) sonic for generating some rock physics parameter and elastic properties, Checkshot or VSP data for well seismic tie and other standard and petrophysical logs such as: Gamma Ray, Caliper, Resistivity, Neutron, Effective Porosity, Water Saturation, Shale Volume etc for defining reservoir properties. Therefore among of the 7 wells located in RAF Field; only 2 wells fulfill these requirements, they are RAF-3 and NE RAF-1. Figure 4.2 and 4.3 show RAF-3 and NE RAF-1 at interested interval of the object study; Upper Gabus formation and its logs standard and its derivatives.

From figures 4.2 and 4.3, at this interval it is seen that Caliper log which reading the borehole diameter shown good shape of well borehole. So it is concluded that logs reading in this interval is considered to be valid and no need any further borehole correction.

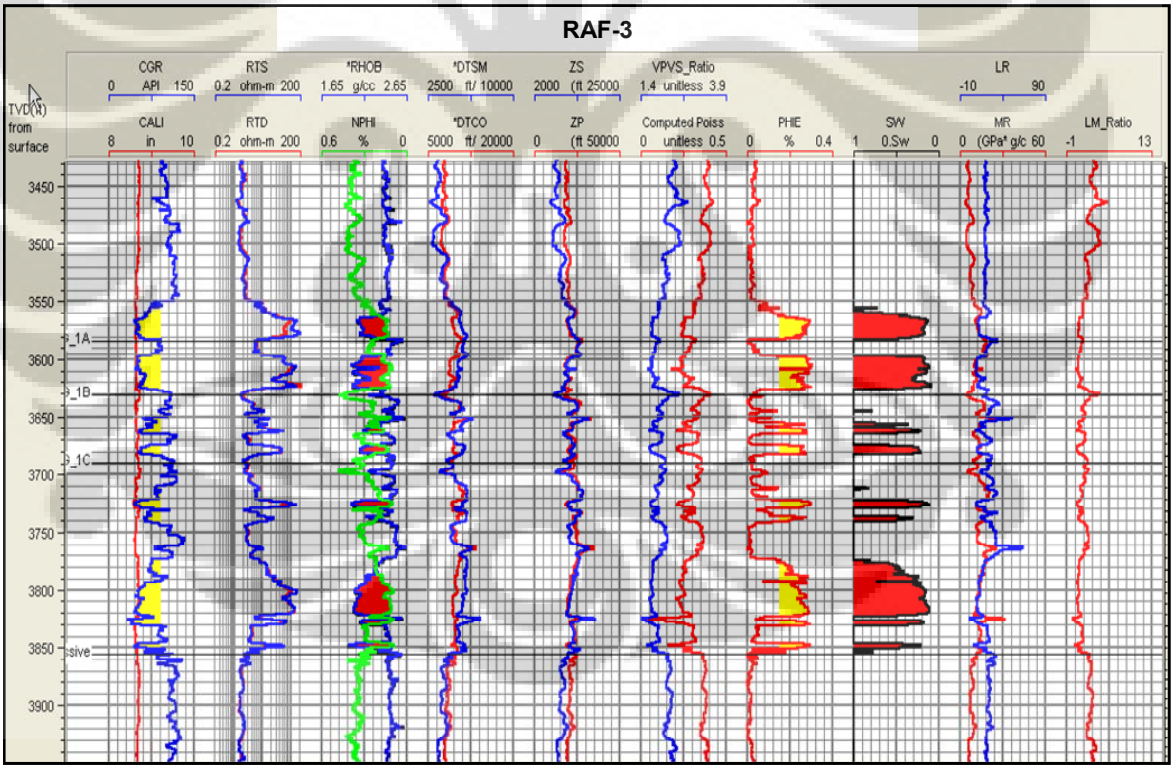

Figure 4.2 RAF-3 at the interested interval of the object study; Upper Gabus formation and its logs standard and its derivatives

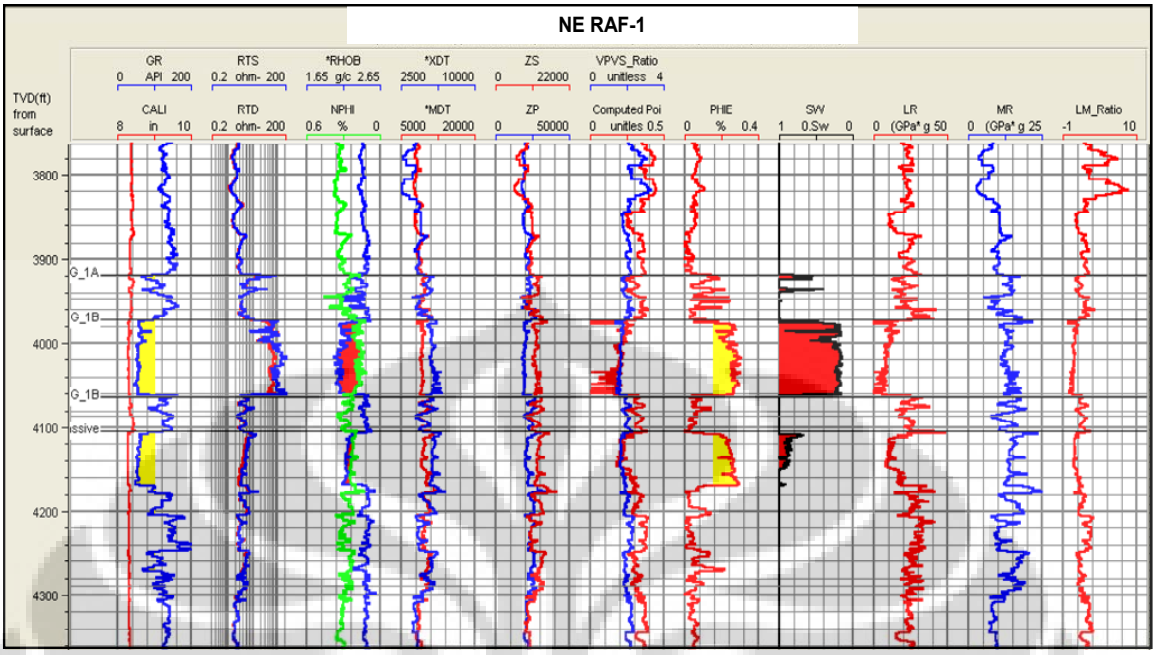

Figure 4.3 NE RAF-1 at the interested interval of the object study; Upper Gabus formation and its logs standard and its derivatives

4.1.2 Seismic Data

As it also mentioned in Chapter-1, this study use a part of 3D seismic survey shown in figure 1.2 which clipped at Inline 6200 – 8950 and Xline 4600 – 5400 to cover only RAF field. This survey has set of Full stack migrated and Partial stack migrated seismic volumes: Near angle stack (5°-15°), Mid angle stack (15°-25°) and Far angle stack (25°-35°) which loaded in 32 bit format and 2 ms sample rate. With assumption a valid processing and conditioning have been applied to this seismic dataset by seismic processing company, so in this study, there is no any seismic conditioning conducted.

Seismic well section of Full migrated stack at well RAF-3 and NE RAF-1 location are shown in figure 4.4, while figure 4.5 and 4.6 show seismic well section of Near, Mid and Far angle stack.

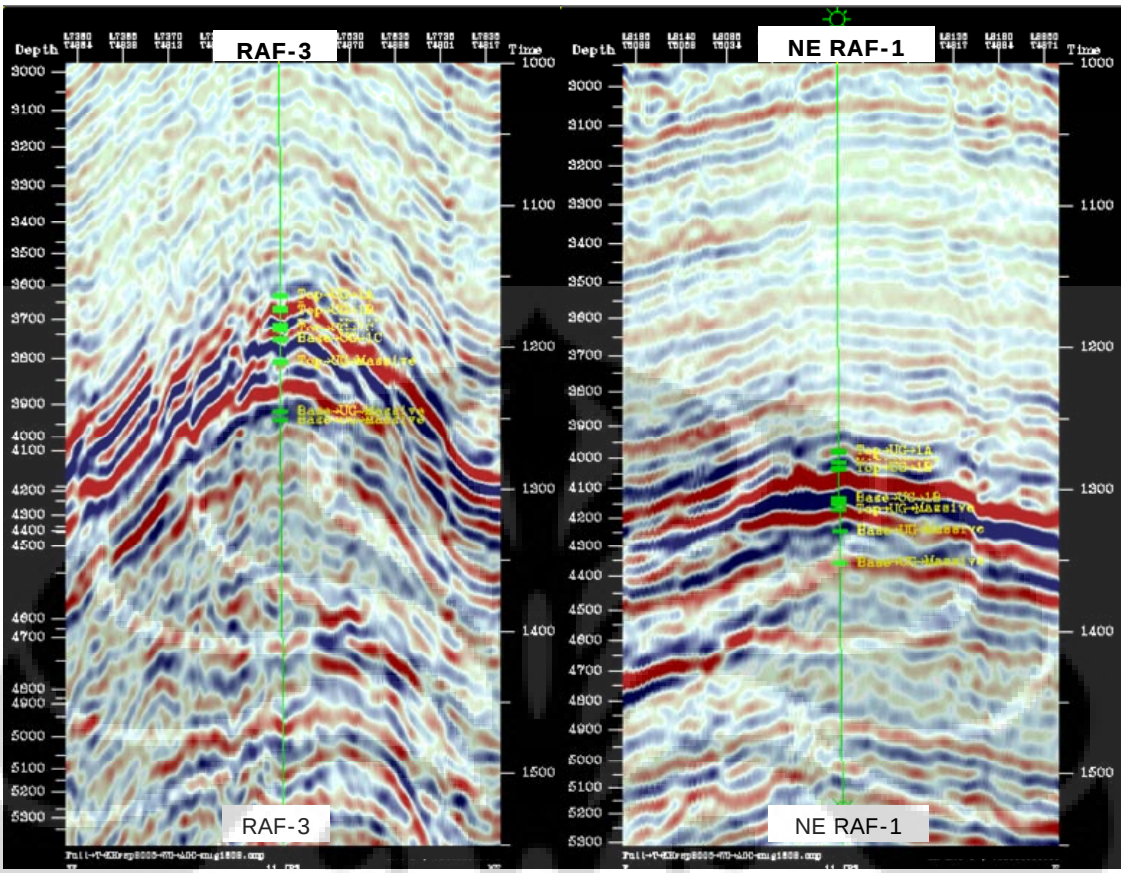

Figure 4.4 Seismic well section of Full stack migrated at RAF-3 and NE RAF-1 well

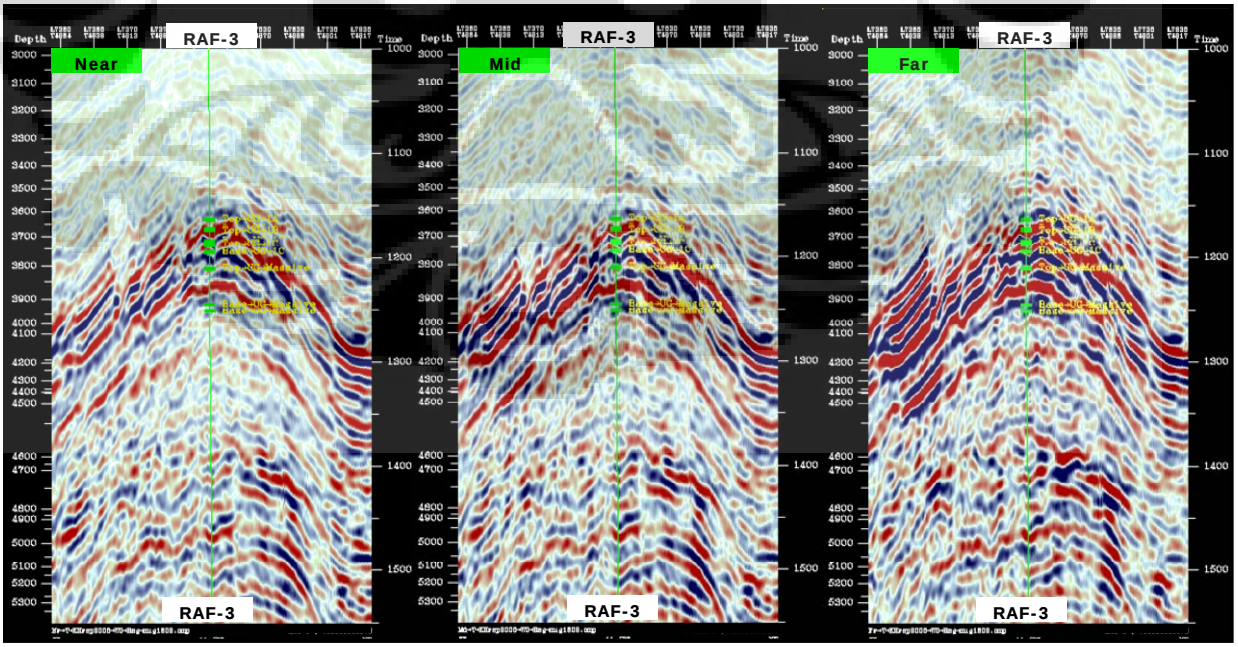

Figure 4.5 Seismic well section of Near, Mid and Far stack migrated at RAF-3 well

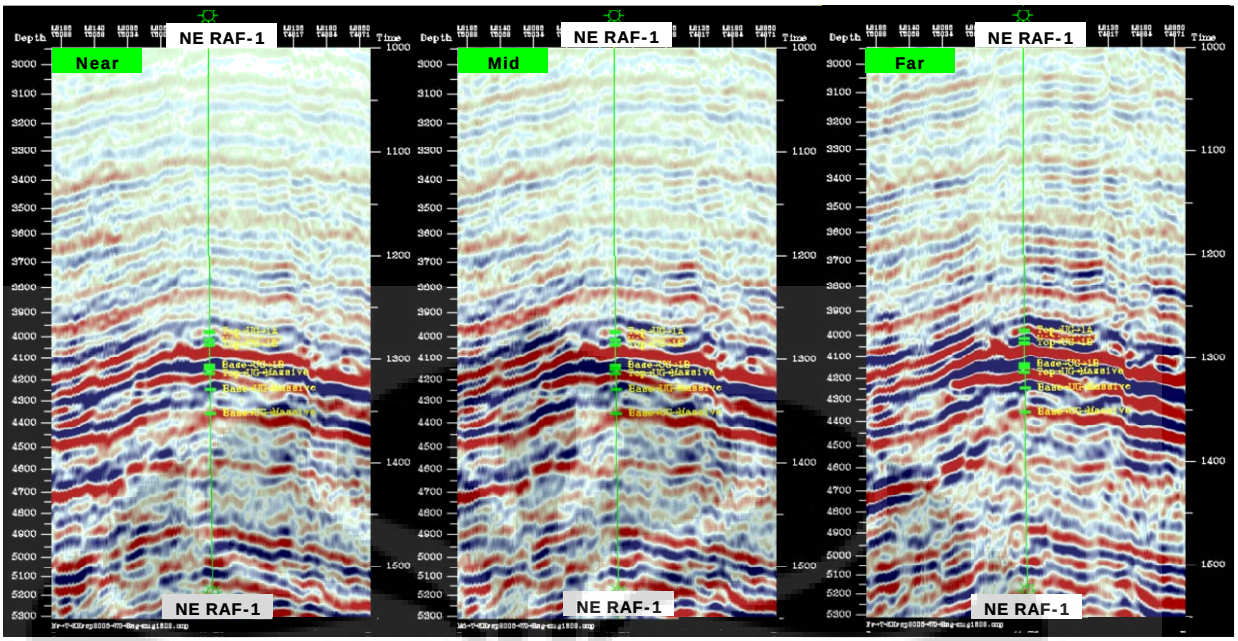

Figure 4.6 Seismic well section of Near, Mid and Far stack migrated at NE RAF-1 well

4.2 Feasibility Study

Once we have been confident with data validity and quality, next we will do the sensitivity test by cross-plotting some rock physic parameters generated from well such as V_PV_S ratio, P and S Impedance, Porosity, Water Saturation, Lambda-Rho, Mu-Rho etc. This is done to check whether the used dataset have the quantity relationship and sensitive to discriminate lithology and fluid effect and also feasible for the further process. In addition, a feasibility check is also conducted to check whether seismic resolution can highlight the reservoir thickness by applying well log frequency filter on key curves refer to dominant frequency contained in the seismic data. As in the workflow, this is the important phase whether we continue to use this dataset or not. If the sensitivity result does not discriminate lithology and fluid effect then suggested to get other dataset which will produce relationship for those above rock physic parameters and or if the log frequency filter is not resolved in seismic dominant frequency then we can go to get other dataset.

Figure 4.7 and 4.8 show cross plot of V_P/V_S vs Z_P and Z_S vs Z_P at RAF-3 and NE RAF-1 well that demonstrate fluid and simplified lithology (sand – shale) discrimination at the interval of Upper Gabus Formation.

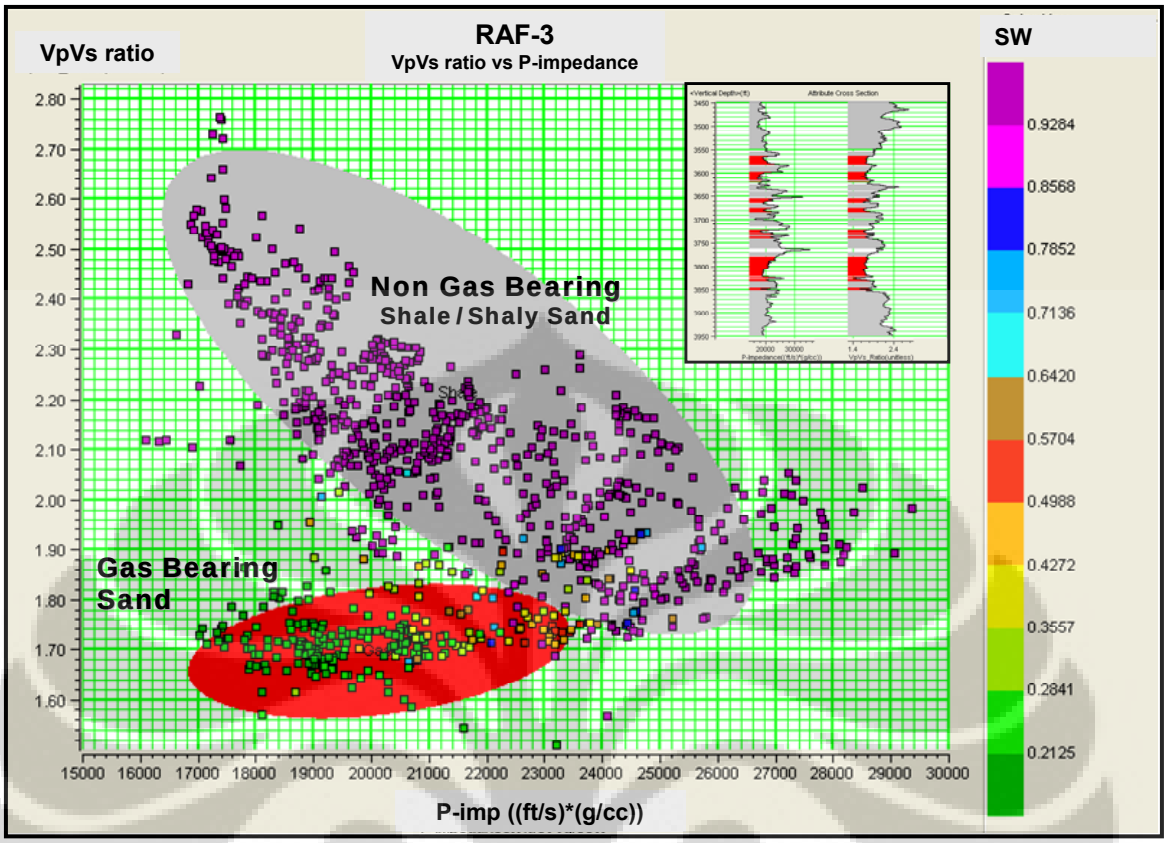

Figure 4.7 show cross plot of V_P/V_S vs P-impedance at RAF-3 well that demonstrate the fluid and litology discrimination at the interval of Upper Gabus Formation.

Qualitatively, from this above cross-plot, shale can be discriminated at VpVs ratio: 1.9 – 2.6 and Gas sand at 1.6 – 1.8. These values are consistently close to or in the range of Goodway's (1997) values table of rock physics analysis using Lame' parameter as showed on table 3.1 repeated from Chapter 3.

TABLE 1	Vp (m/s)	Vs (m/s)	ρ (g/cc)	Vp/Vs	$(Vp/Vs)^2$	σ	λ + 2μ	μ	λ	λ/μ
Shale	2898	1290	2.425	2.25	5.1	0.38	20.37	4.035	12.3	3.1
Gas Sand	2857	1666	2.275	1.71	2.9	0.24	18.53	6.314	5.9	0.9
Avg. Change	1.40%	25%	6.40%	27%	55%	45%	9.20%	44%	70%	110%

(moduli λ, μ are in GPa's)

Table 3.1 Rock physics analysis using Lame' parameter (Goodway's, 1997)

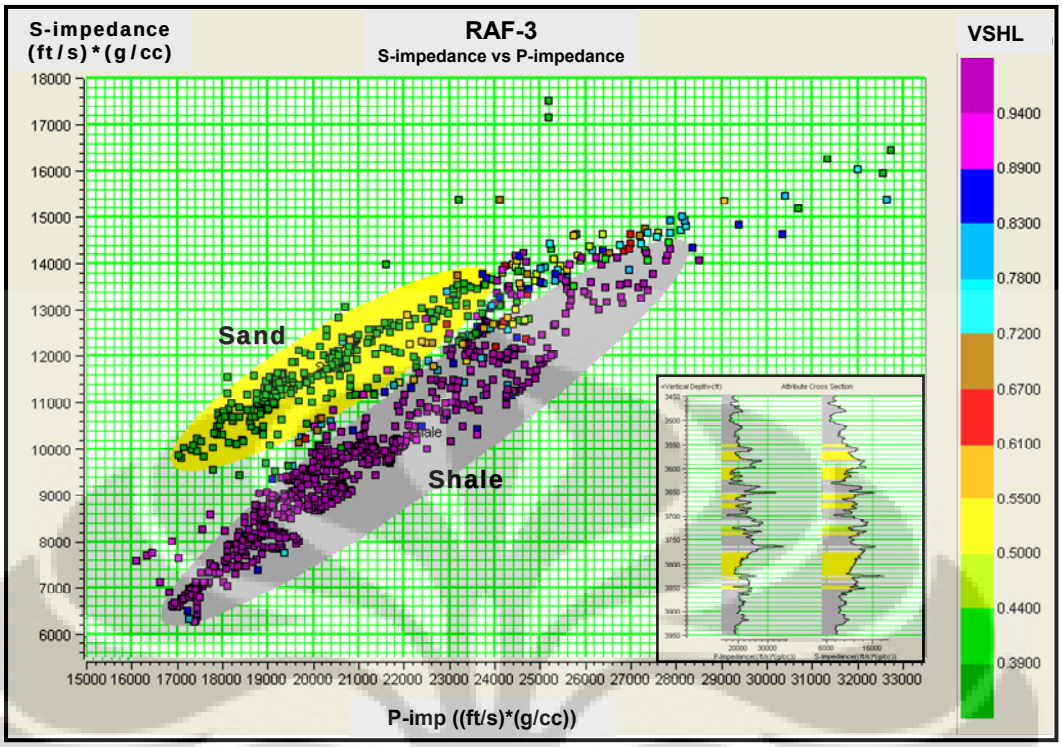

Figure 4.8 show cross plot of S-imp vs P-imp at RAF-3 well that demonstrate simplified litology (sand – shale) discrimination at the interval of Upper Gabus Formation

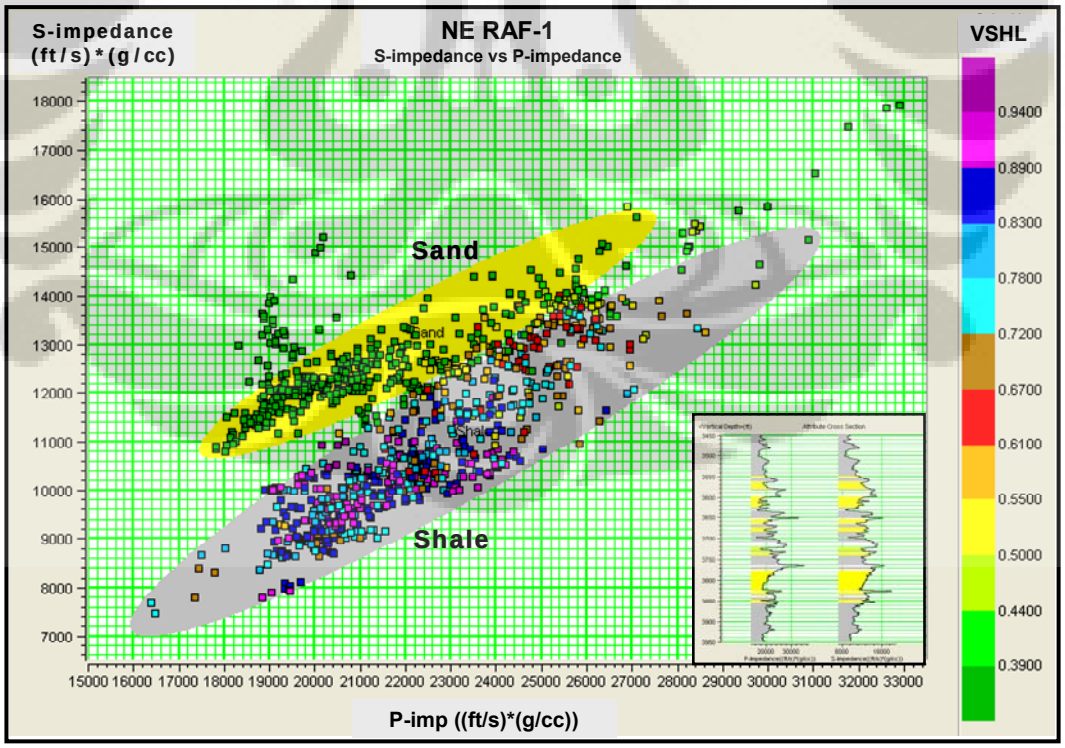

Figure 4.9 show cross plot of S-imp vs P-imp at NE RAF-1 well that demonstrate simplified litology discrimination at the interval of Upper Gabus Formation

In addition, a feasibility check has also been conducted to check whether seismic vertical resolution can highlight the reservoir thickness. By the theory, seismic vertical resolution is about ¼ λ where λ = v / f. With v: average velocity at reservoir interval 8660 ft/s and f: dominant frequency 30 Hz, minimum reservoir thickness which can be resolved by seismic resolution is 72 ft at the minimum. However instead of quantitative estimation, it is also checked qualitatively by log frequency filtering. Several log frequency filtering were applied to V_PV_S ratio curve of RAF-3 and NE RAF-1 (figure 4.10 and 4.11) in relation with dominant frequency contained in the seismic data. Figure 4.12 show that dominant frequency was populated on frequency 30 Hz at RAF-3 and 35 Hz at NE RAF-1. From figure 4.10, it can be concluded that some reservoir resolution still can be resolved at seismic dominant frequency range of 30 - 35 Hz.

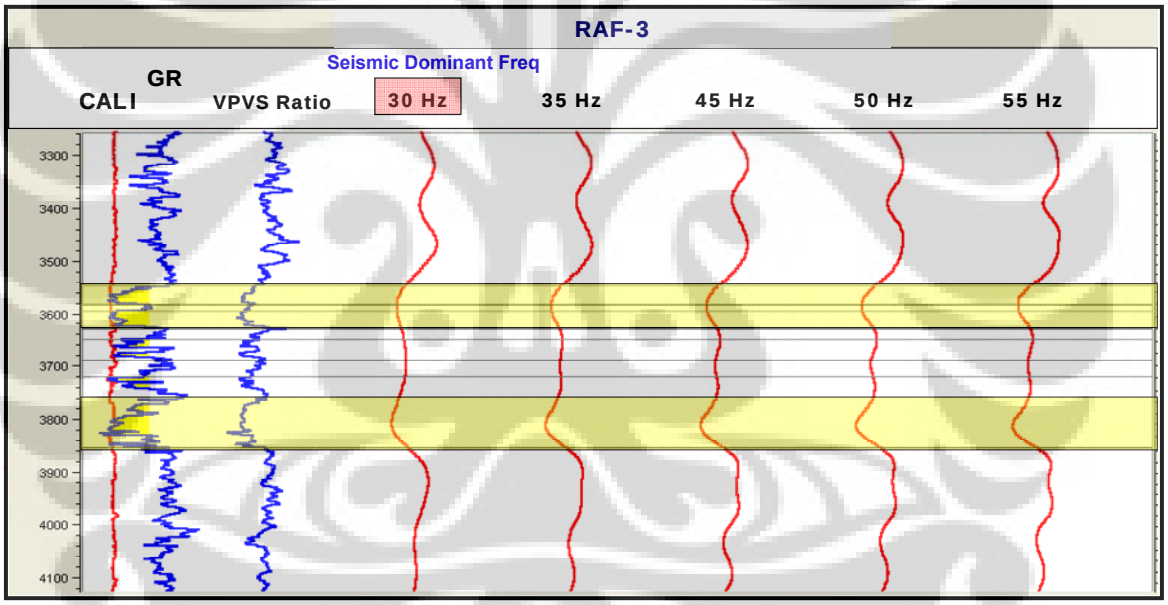

Figure 4.10 Frequency filter applied on VpVs ratio curve of RAF-3 show that some reservoir sand still can be resolved at Seismic Dominant Freq Range of 30 Hz

This feasibility study has given a confirmation that on this dataset, cross plot of rock physics parameters are able to discriminate the effect of lithology and fluid at the interval of Upper Gabus Formation for and the theses are feasible to carry on and furthermore the reservoir still can be resolved at dominant frequency of seismic data.

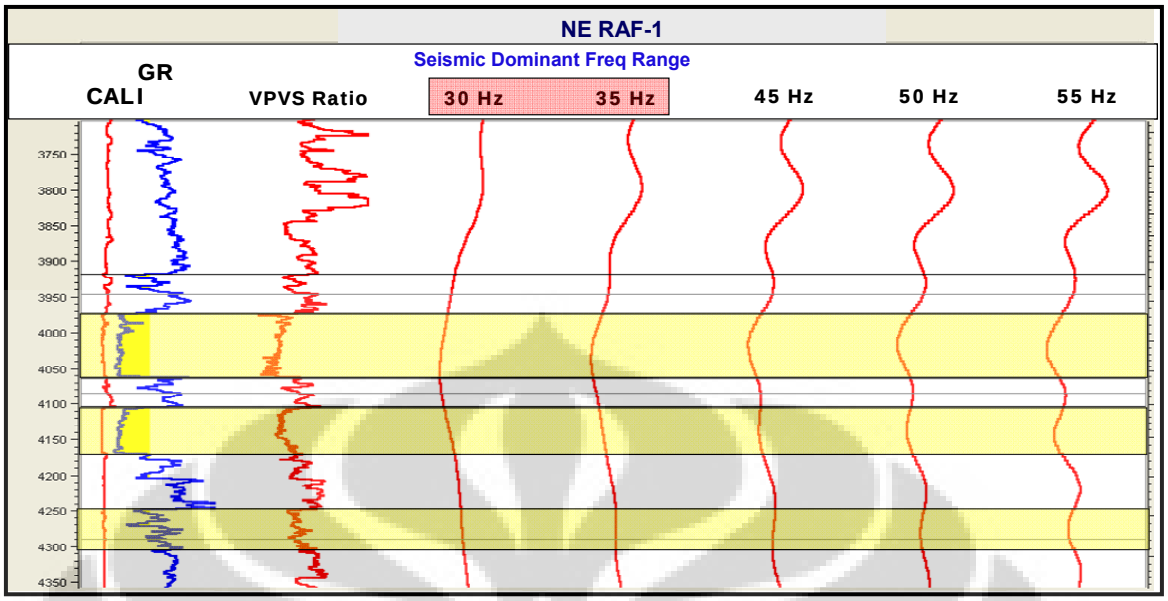

Figure 4.11 Frequency filter applied on VpVs ratio curve of NE RAF-1 show that some reservoir sand still can be resolved at Seismic Dominant Freq Range – 35 Hz

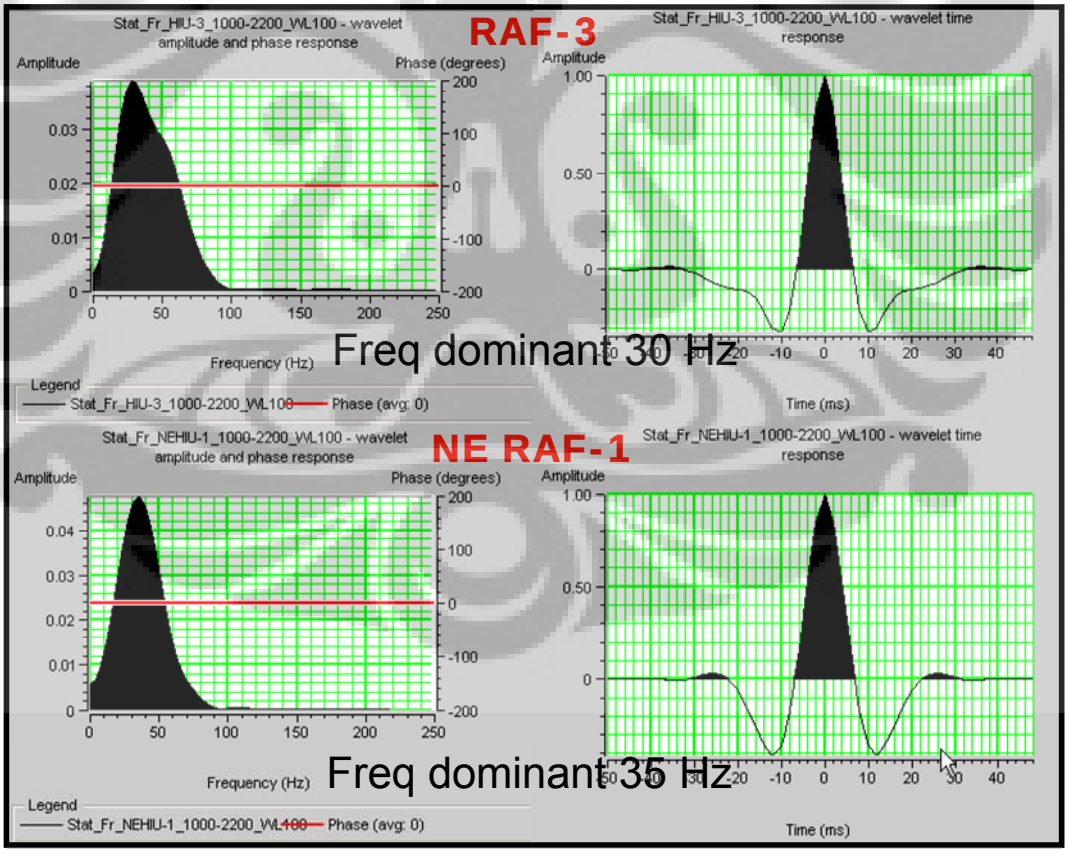

Figure 4.12 Extracted wavelets were from seismic data at RAF-3 and NE RAF-1 with interval 1 – 2.2 sec show dominant frequency range 30 - 35 Hz and its zero phase

4.3 Well-Seismic Tie and Wavelets Estimation

Subsequently, in this step, well data is tying to seismic data which in practical work means tying seismic event in time domain to well geological event in depth domain. This is done by correlating the real seismic trace at the well location with a synthetic seismogram obtained from convolution of wavelet with reflection coefficients. Wavelet itself is a transient signal which has limited amplitude and time interval. A simplification is common used in any inversion process by assuming that there is only a single wavelet as in fact wavelet varies in time and has a complex form.

4.3.1 Synthetic Seismogram

Synthetic seismogram is generated by convolving reflection coefficient with wavelet at the well location. The used wavelet should be appropriate in order to produce the best match or correlation between Synthetic seismogram and the real seismic trace which in this case, full stack migrated volume is used for well-seismic tying purpose. The goal of this correlation is to get best match qualitatively and quantitatively by the highest correlation coefficient (0 – 1).

Wavelet can be generated from several common methods such as Ricker wavelet: dominant frequency value as the input; Bandpass wavelet: Low-High cut and pass frequency values as the input; Statistical wavelet: extracting wavelet from seismic data around the well target zone; Well wavelet: extracting wavelet from seismic data along the bore hole in the target zone interval. However from some trial and error, in this study, Ricker wavelet has already produced a good correlation for well-seismic tying with some time shift applied.

In this study, the correlation window was set at 1000 – 1500 ms, in order to focus on the interested interval. From the correlation window, using the original time-depth data available in the well, it found that it only required 8 ms time shift to get 0.726 correlation coefficient at RAF-3 (figure 4.13) and 2 ms time shift to get 0.819 correlation coefficient at NE RAF-1 (figure 4.14). As the other result of this process, a corrected time-depth table was saved for further process.

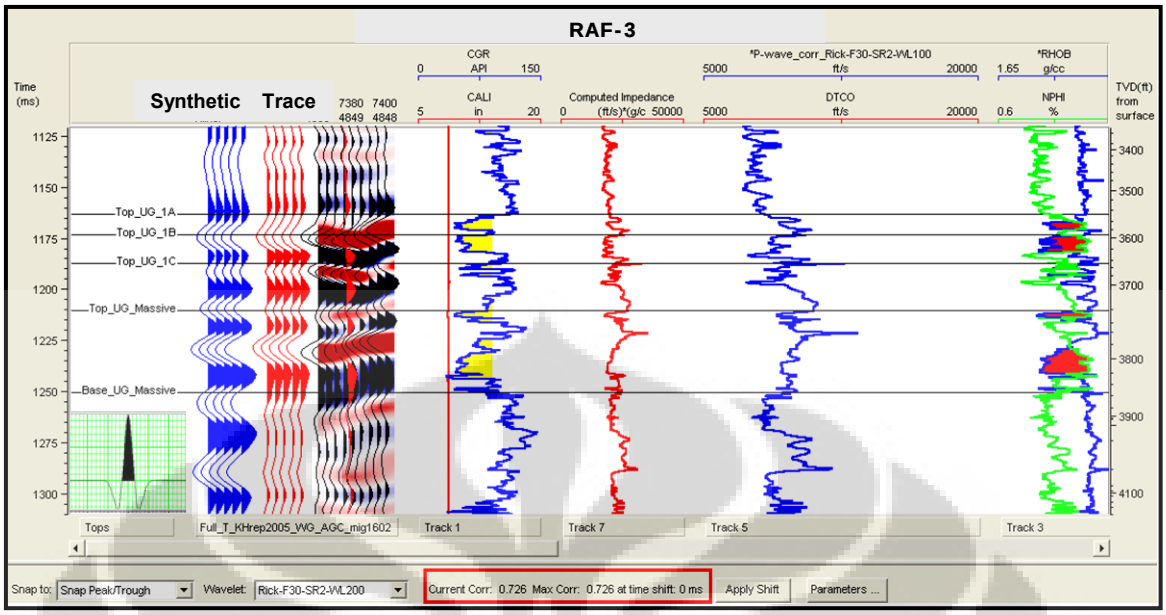

Figure 4.13 Seismic synthetic to trace correlation at RAF-3 using Ricker wavelet 30 Hz.

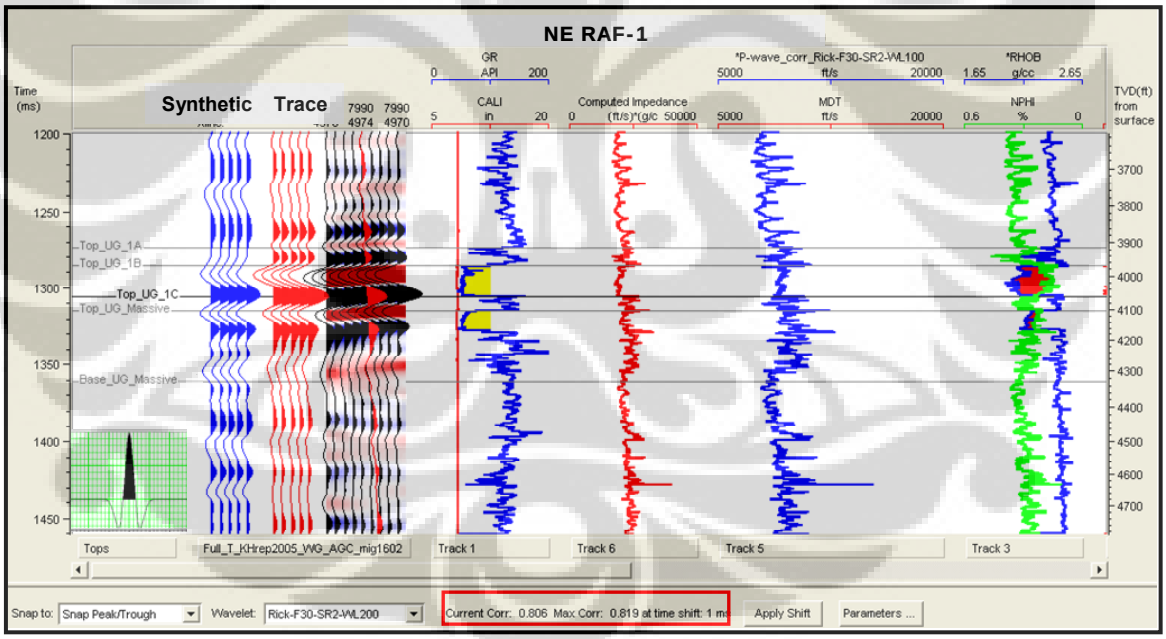

Figure 4.14 Seismic synthetic to trace correlation at NE RAF-1 using Ricker wavelet 30 Hz.

From the correlation windows above, it can be seen that some of top reservoirs were not consistently falls on the same seismic event. This is possibly due to disparity in lithology, porosity, thickness or its fluid content between RAF-3 and NE RAF-1 especially at UG-1A, UG-1B and UG-1C sand. However, after reviewing at larger area of the seismic data, therefore based on seismic event continuity as well as consider its

consistency and its easiness to pick, it was decided that Top_UG_1A falls at Zero Crossing; Top_UG_1B at Zero Crossing; Top_UG_1C at Peak; Top_UG_Massive at Trough and Base_UG_Massive at Peak and this become the reference in horizon picking.

4.3.2 Wavelet Estimation

Next stage is a critical task to do in this workflow which is wavelet estimation from every partial angle stack: near, mid and far angle stack. These wavelets later become the important input in the simultaneous inversion algorithm. Wavelet estimation is generated in two (2) steps. First, estimate wavelet by Statistical extraction method to get the first pass of estimation and second, estimate wavelet by Well extraction method to get finer estimation and higher correlation coefficient.

Wavelets were extracted from seismic data at an interval of 1000 – 1500 ms with a wave length 100 and taper length 25 to minimize the unwanted side lobes. After conducting some trial and errors of wavelet extraction to get the highest correlation coefficient for each wavelet used for the correlation, it could be concluded that well extracted wavelets of NE RAF-1 give the higher correlation coefficient than wavelets extracted from RAF-3 (table 3.2). Figure 4.15 show wavelet plot in time and frequency response of RAF-3 and NE RAF-1 for every partial angle stack, it is shown that NE RAF-1 well extracted wavelets are closer to zero phase which is consistent to the used seismic phase. Therefore this is justified to use NE RAF-1 well extracted wavelet for simultaneous inversion process later.

Additional test was also conducted which using NE RAF-1 wavelet to RAF-3 synthetic to trace correlation to check whether it still give a good result or not. Figure 4.16 show that NE RAF-1 wavelet was still give good correlation coefficient when it was used to RAF-3 synthetic to trace correlation.

Well / Volume	Statistical Extraction			Well Extraction		
	Near	Mid	Far	Near	Mid	Far
RAF-3	0.760	0.734	0.758	0.774	0.808	0.798
NE RAF-1	0.868	0.864	0.751	0.910	0.907	0.789

Table 4.1 Correlation coefficient resulted from statistical and well extraction

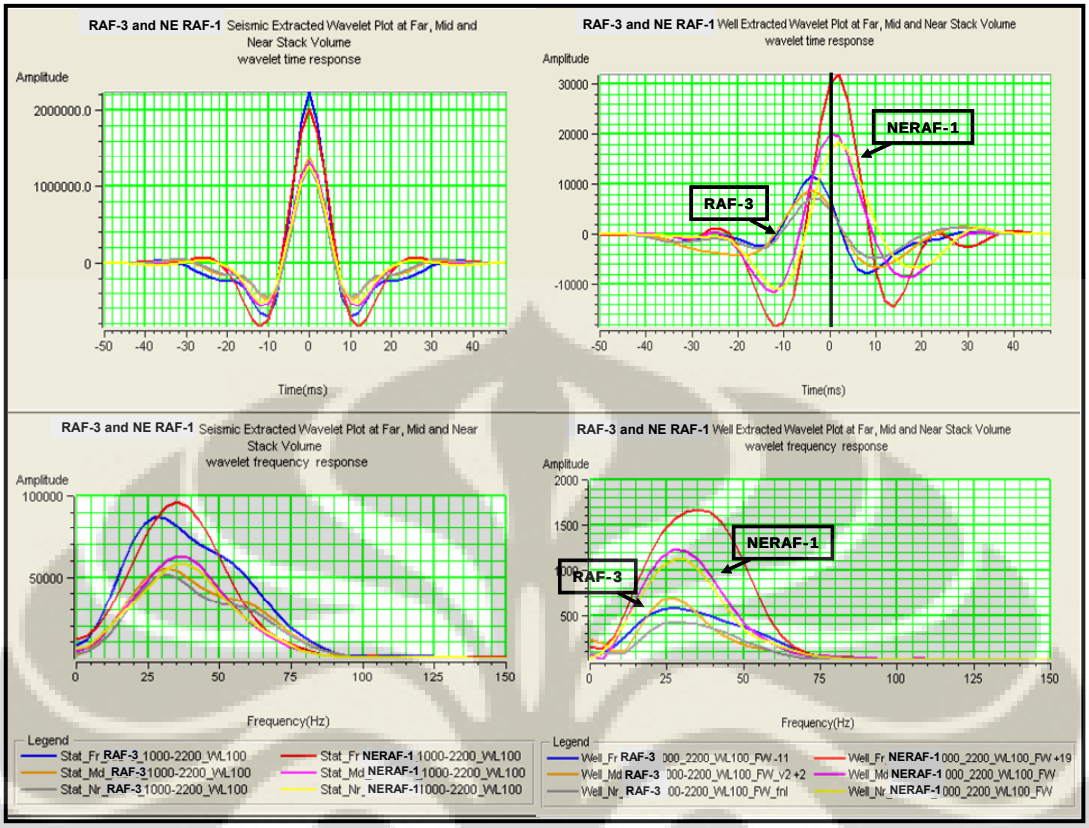

Figure 4.15 show wavelet plot in time and frequency response of RAF-3 and NE RAF-1 for every partial angle stack

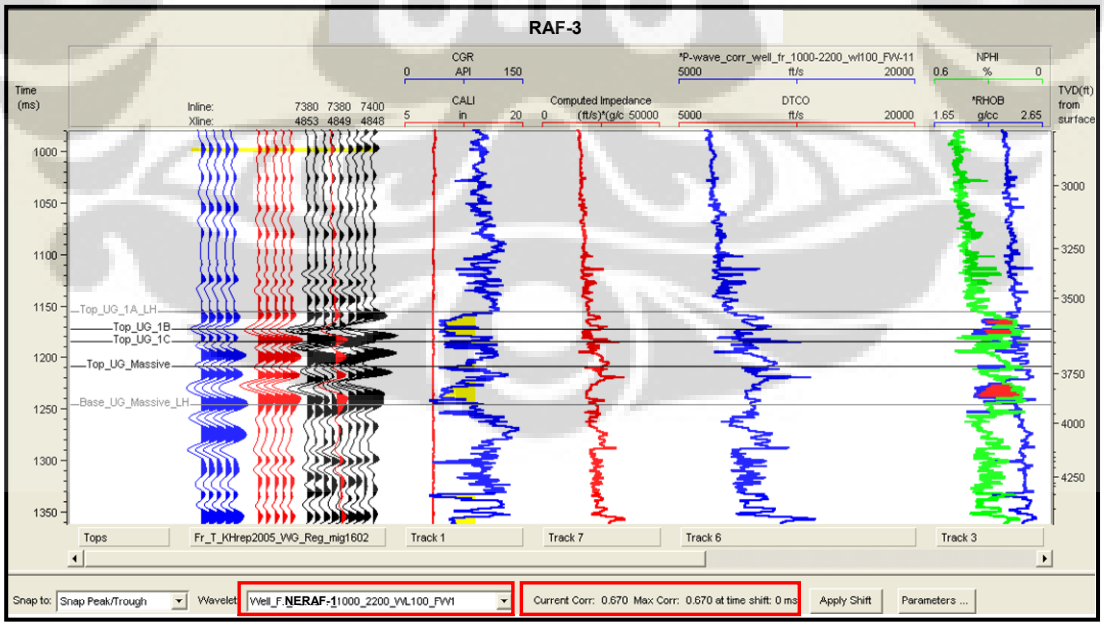

Figure 4.16 show that NE RAF-1 well extracted wavelet was still give good correlation coefficient when used for RAF-3 synthetic to trace correlation.

4.4 Horizon and Fault Interpretation

Using full stack migrated volume, first step in this stage is interpreting the fault framework. Fault picking was done at per 10 xlines and 50 ilines then correlated between fault segments. Next, seismic horizons of the seismic event can be picked refer to geological well event using corrected time-depth curve resulted from well seismic tie step. Horizon picking was also done at the same increment as fault interpretation. It was initially picked at arbitrary line between RAF-3 and NE RAF-1 (figure 4.17) and combining with inline and xline looping technique. Then it was interpolated to populate them laterally. In this study, there are 5 interpreted horizons: Top_UG_1A, Top_UG_1B, Top_UG_1C, Top_UG_Massive and Base_UG_Massive. Figure 4.20 shows these 5 interpolated horizons.

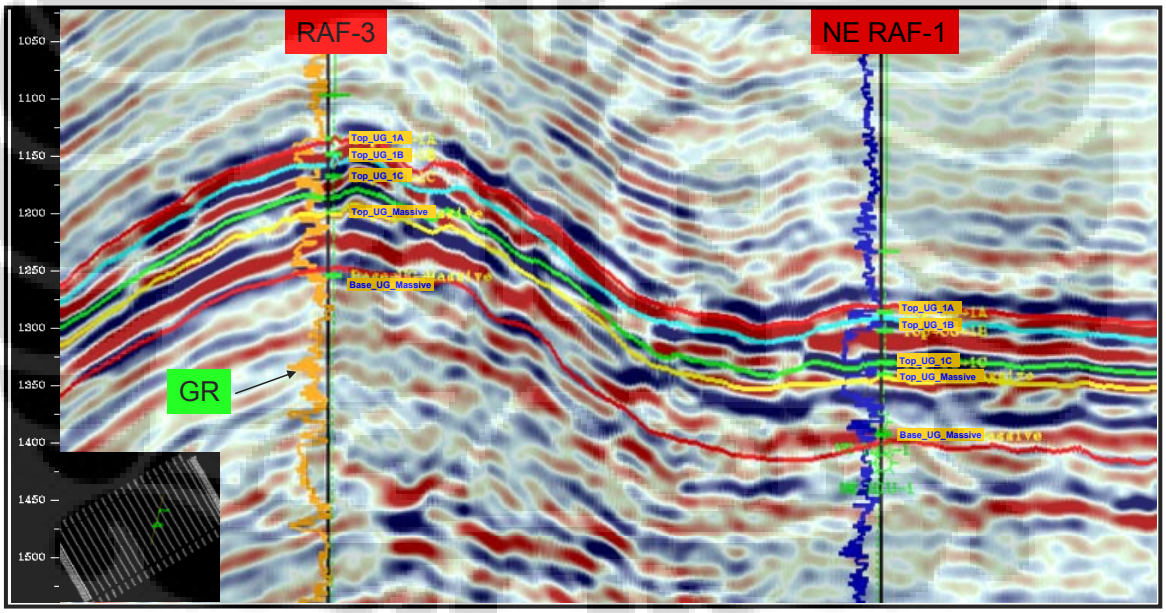

Figure 4.17 Horizon picking at RAF-3 and NE RAF-1 arbitrary line

Fault polygon was generated by trimming the horizons intersection to fault segment which then calculated its heave. This fault polygon was then used for time structural mapping.

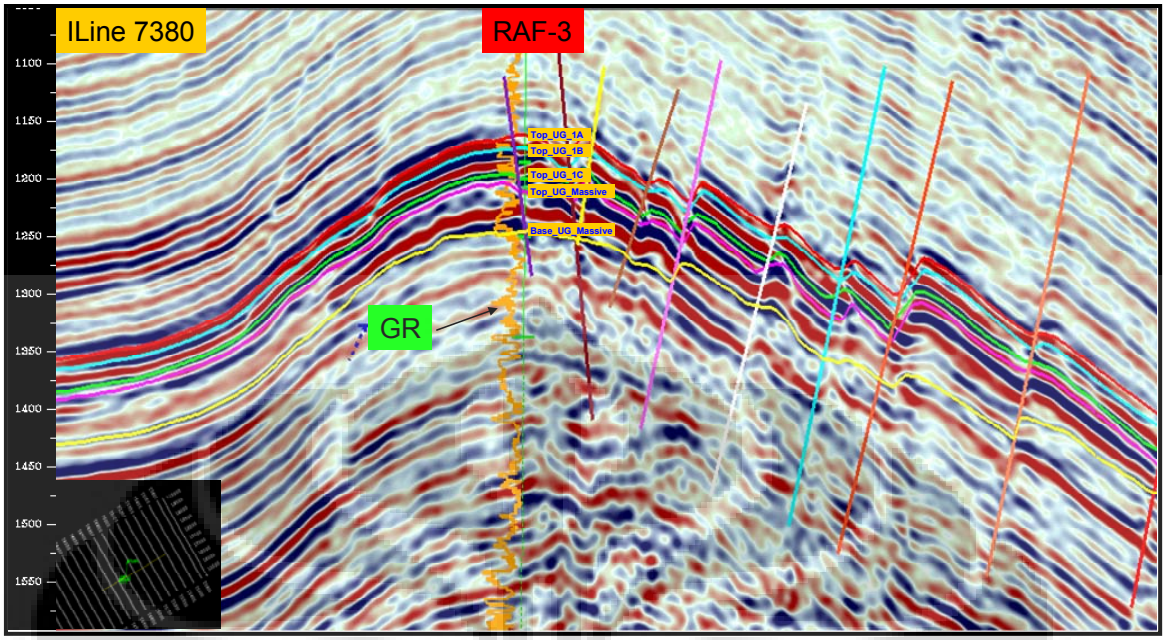

Figure 4.18 Horizon and fault picking at Inline 7380 at RAF-3 well location

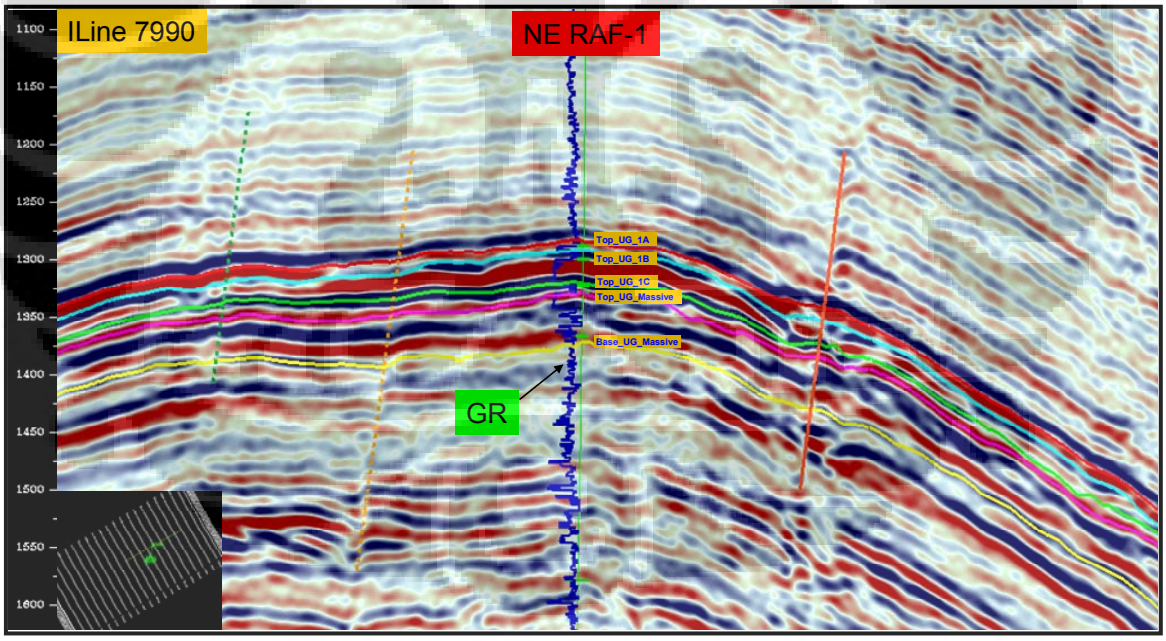

Figure 4.19 Horizon and fault picking at Inline 7990 at NE RAF-1 well location

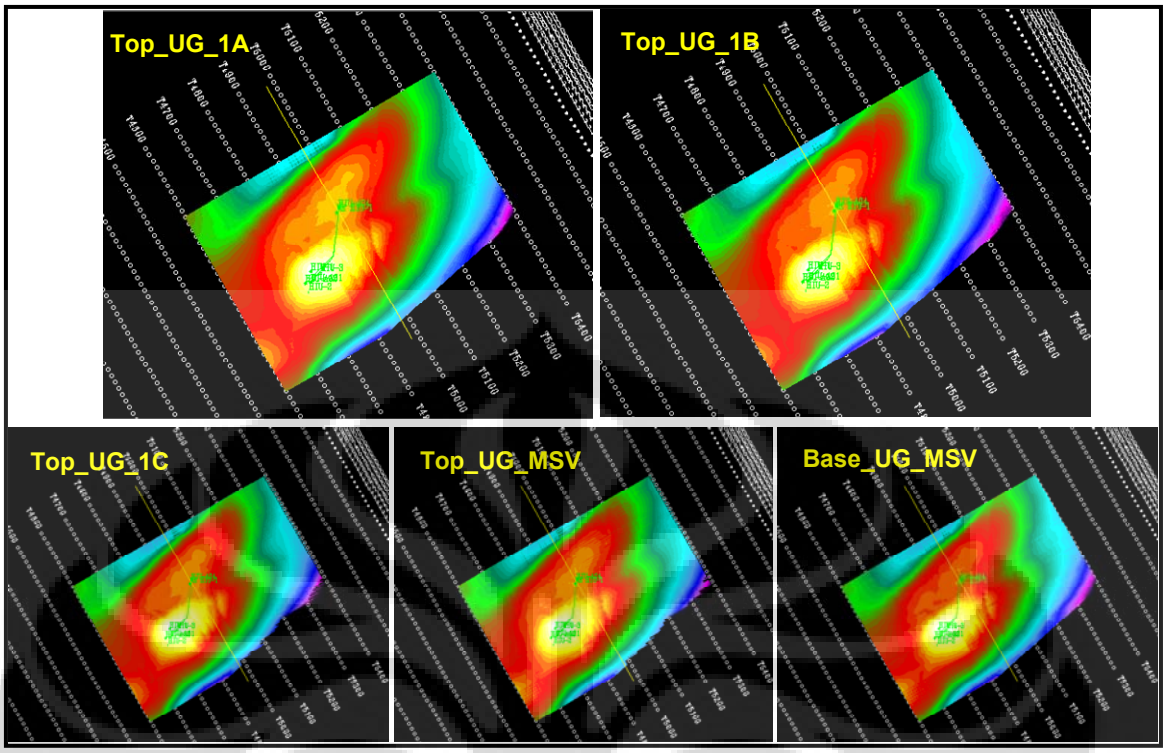

Figure 4.20 Five interpolated horizons in this study

4.5 Low Frequency Model

Before stepping to inversion process, it is required to have low frequency model which provides an initial guess in the inversion and also provides a proper selection of log curves used in determining the regression coefficients in the well data cross plot. Low frequency or also known as Initial Model is generated by interpolating and extrapolating well P-impedance (Z_P), S-impedance (Z_S) and Density with horizons as the guidance which then filtered in frequency. In this study, frequency filtered at high pass 5 Hz and high cut 10 Hz. As the result, there are 3 initial models generated: Z_P model, Z_S model and Density model (figure 4.21)

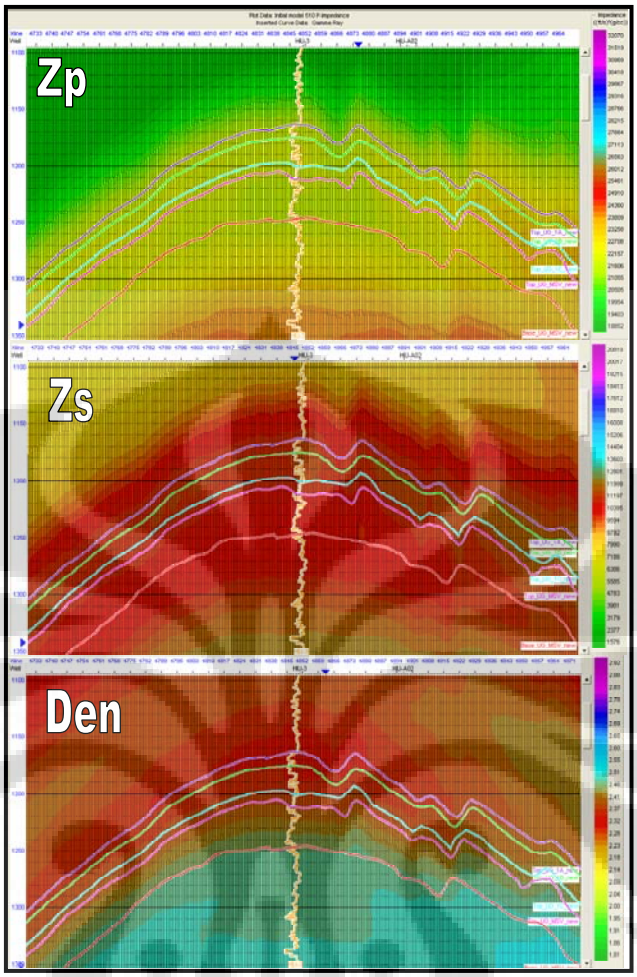

Figure 4.21 Initial models section at RAF-3 well location

4.6 Pre-Inversion QC Analysis

The Inversion QC analysis performs an inversion on selected well locations, which means testing a range of inversion parameters quickly and also used to see how well the analysis inversion succeeded or to compare different parameters before performing the actual inversion.

The inversion parameters are reflecting the background relationship between $\ln(Z_P)$, $\ln(Z_S)$, and ln(Density) which written on equation (36) and (37) on Chapter 3. They are extracted from the regression linear trends drawn on cross plot $\ln(Z_P)$ versus $\ln(Z_S)$ and $\ln(Z_P)$ versus ln(Density) as the regression coefficient – k, k_C, m, m_C, ΔL_S, ΔL_D (figure 4.22). These coefficients were then used to generate the inversion QC analysis window (figure 4.23) which giving good correlation coefficient: 0.952.

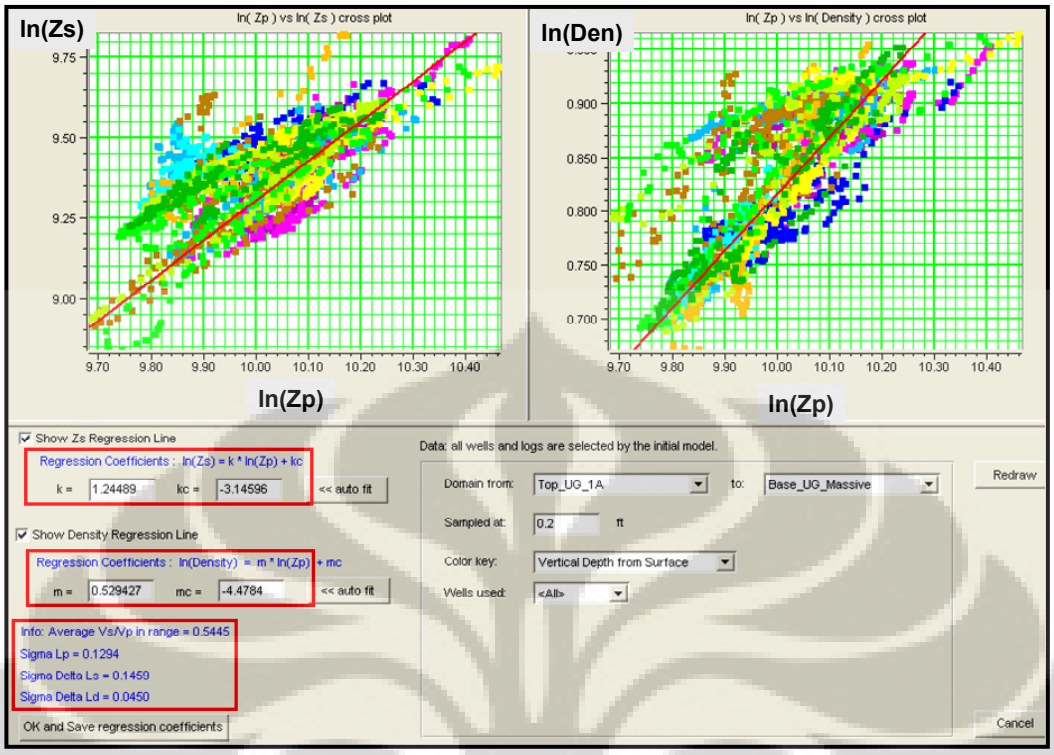

Figure 4.22 show regression linear trend between ln(ZP), ln(ZS) and ln(Density) and its regression coefficient

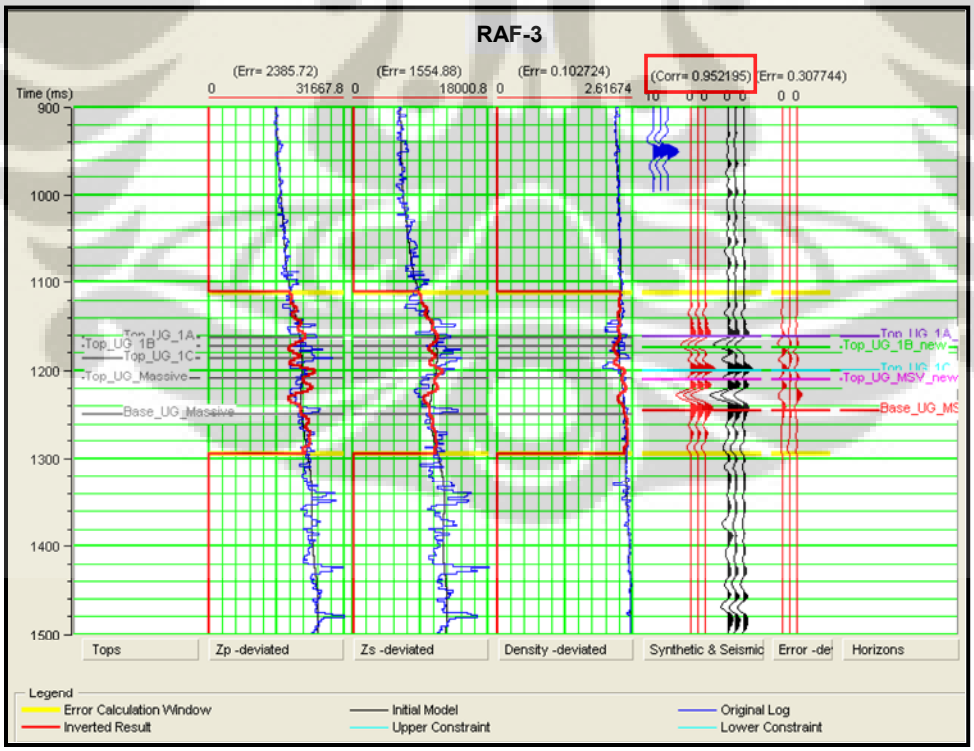

Figure 4.23 inversion QC analysis window at RAF-3 showing good correlation between the inversion traces and the original logs

4.7 Simultaneous Inversion

Next, after having the inversion parameters and confident with the inversion QC analysis, simultaneous inversion can be then conducted. Simultaneous inversion process collaborate low frequency model, partial angle stack seismic, wavelets and the inversion parameters to generate P impedance, S impedance and Density volumes. The simultaneous inversion target was constrained at +/- 50 ms of Top_UG_1A and Base_UG_Massive for the time and disk space efficiency. Inversion results at the well section are showed at figure 4.24.

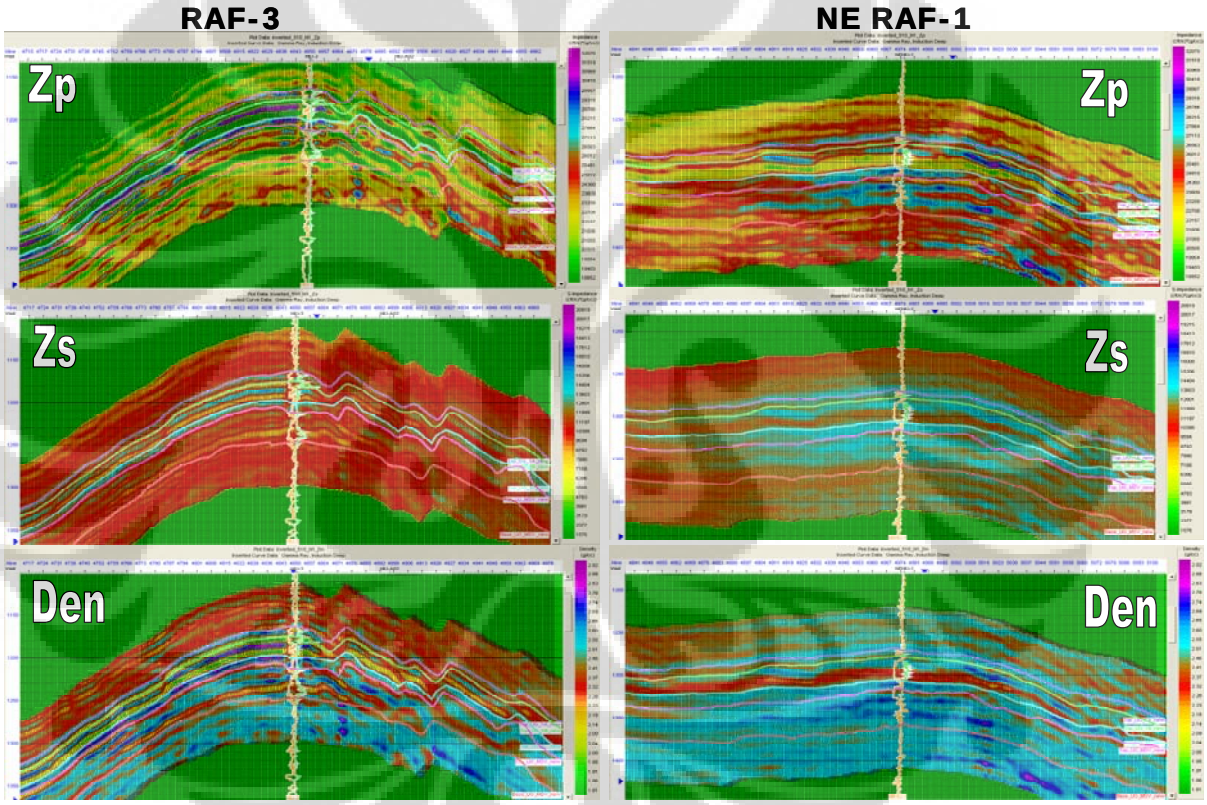

Figure 4.24 Inversion results at the RAF-3 and NE RAF-1well section

The next step in the study workflow: Analysis and Interpretation will be discussed at Chapter 5: Analysis and Interpretation.

Chapter Five:
ANALYSIS AND INTERPRETATION

Based on the simultaneous inversion results done in Chapter 4 which are P-impedance, S-impedance and Density volumes, they can be analyzed for further interpretation to achieve the thesis goals in the following ways.

5.1 Rock Physics Template

Rock physics template (RPT) was generated by plotting all parameters in the same scale and same template for defining the rock physics model in the RAF structure and later will be applied as a guide in mapping gas and lithology distribution on the seismic scale. This step is started by making cross plot S-impedance and P-impedance of RAF-3 and NE RAF-1 well data (figure 5.1) to define lithology and fluid effect discrimination zones. Next step is overlying these zones on cross plot of S-impedance and P-impedance extracted from inversion result at well location.

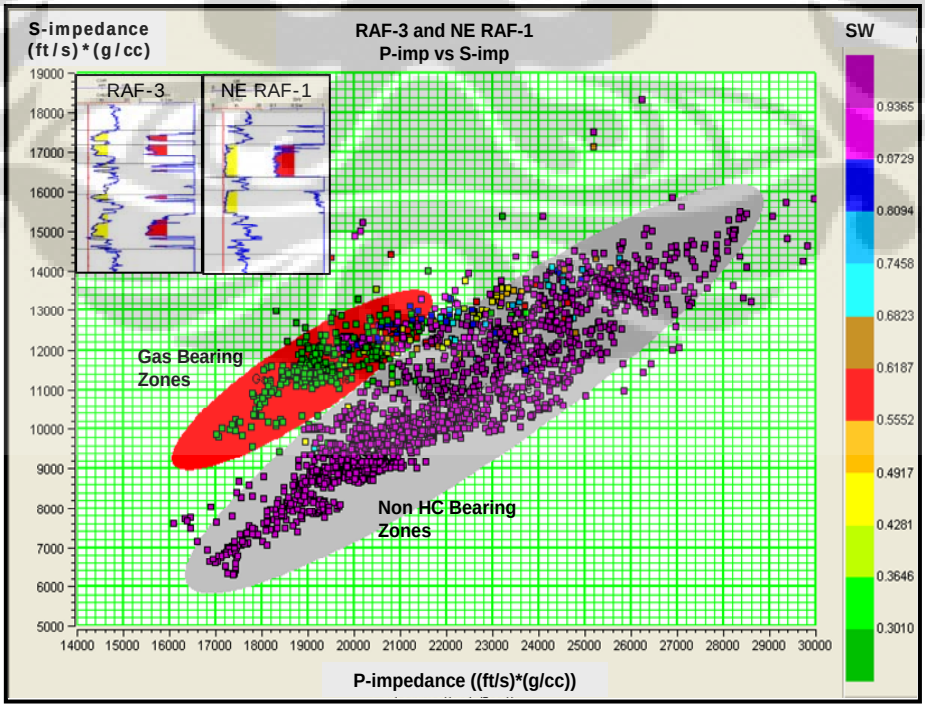

Figure 5.1 P-impedance vs. S-impedance cross plot of RAF-3 and NE RAF-1 well

The reason of this overlying is to test whether the inversion result can discriminate lithology and fluid effect as well as to check whether its discrimination zones falls consistently within zones generated from well cross plot.

Figure 5.2 confirmed that inversion result extracted at RAF-3 and NE RAF-1, at reservoir interval, showing good discrimination of lithology and fluid effect and the overlaid well cross plot zones are consistently fallen on the expected area. The good overlying is seen on the Non HC Bearing zone where well cross plot zone is almost covering all the inversion point. While Gas Bearing zones although do not cover perfectly on the expected points, it has a consistent trend. This is understandable as seismic data has lower vertical resolution compared to well data instead of they both have different sample interval which 2 ms for seismic and 0.5 ft for well data.

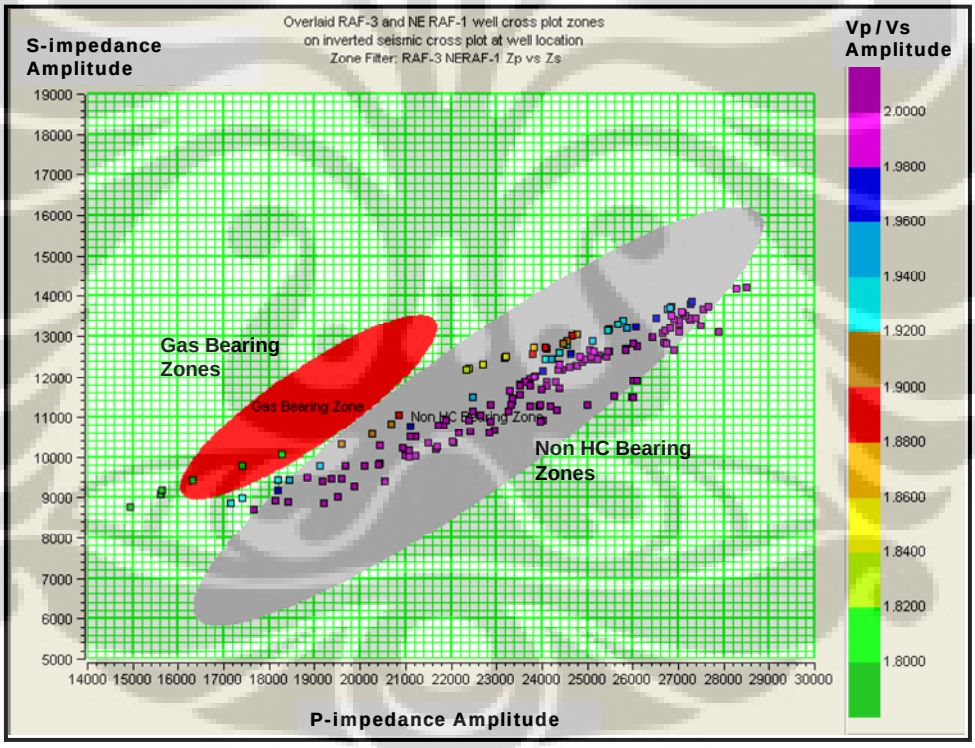

Figure 5.2 P-imp and S-imp cross plot of inversion result extracted at well location at reservoir interval and overlaid with well cross plot zones.

However for further interpretation, we will customize the cross plot zones to fit the seismic data population and distribution (figure 5.3). The well log cross section zones are mostly showing a very good match corresponds to well log lithology and fluid content.

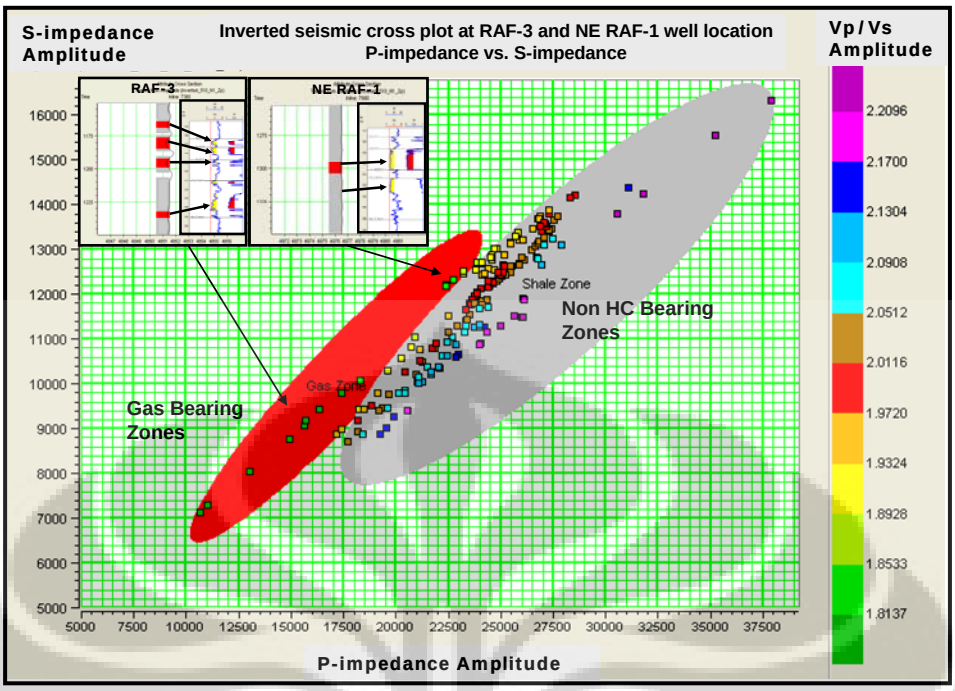

Figure 5.3 Customized cross plot zones of P-impedance and S-impedance extracted at well location and at reservoir interval.

5.2 Cross Plot Volume

Next step is to bring this cross plot zones: Gas Bearing and Non HC bearing zones into seismic volume as color data. As shown in figure 5.4 and 5.5, seismic sections are overlaid by cross plot zone at RAF-3 and NE RAF-1 location.

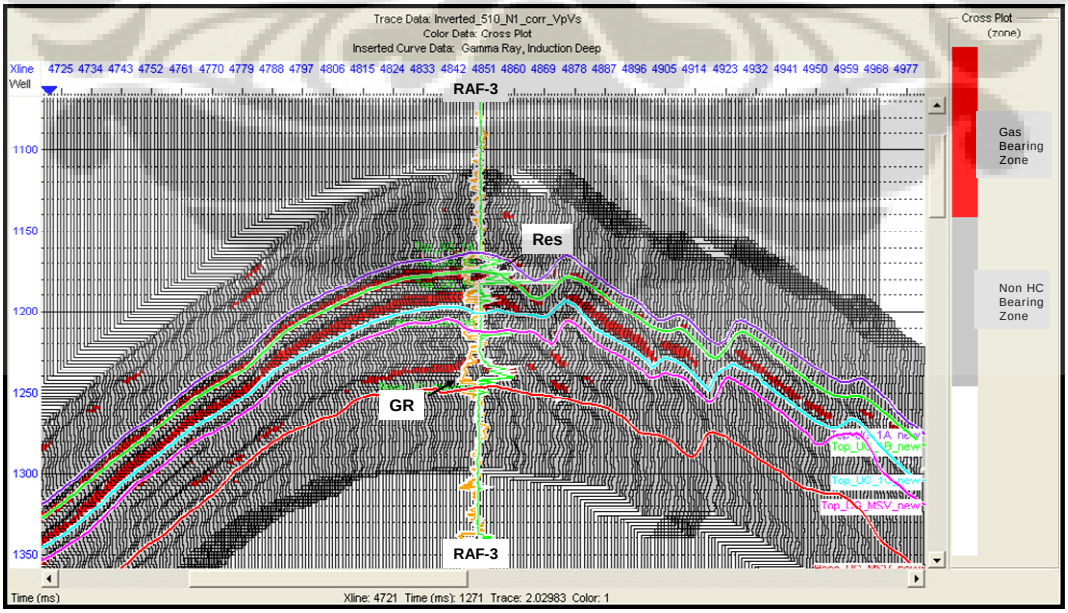

Figure 5.4 Seismic sections overlaid by cross plot zone at RAF-3 well location

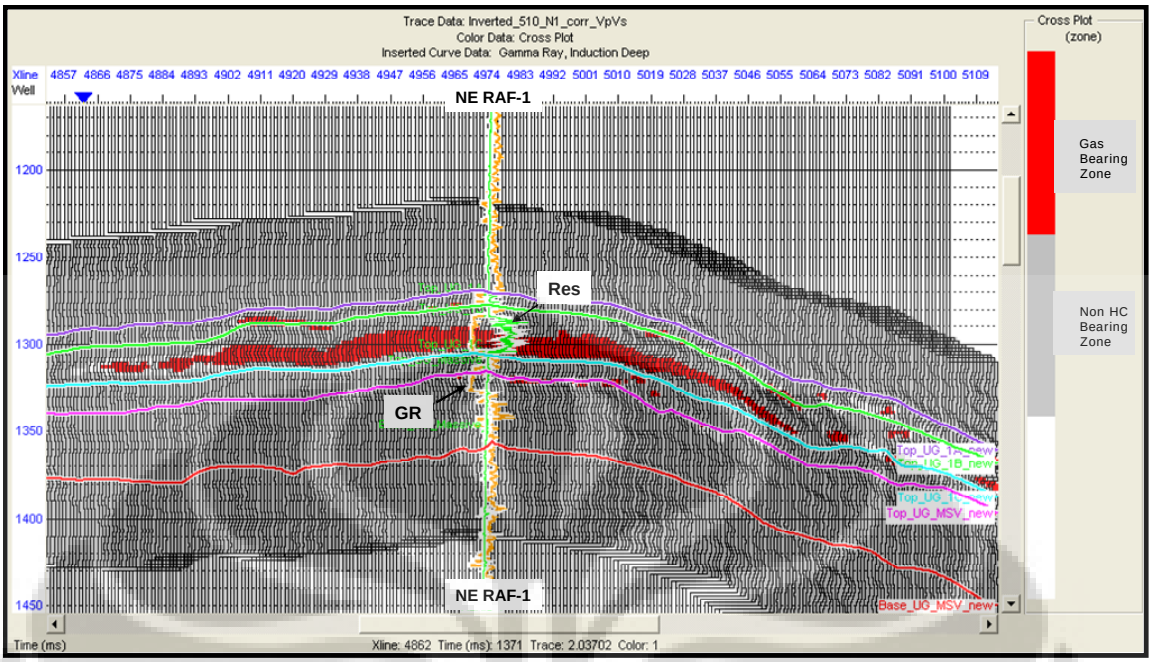

Figure 5.5 Seismic sections overlaid by cross plot zone at NE RAF-1 well location

From figure 5.4 and 5.5, it could be seen that the red color of RPT is consistently coloring the gas pay zone of RAF-3 and NE RAF-1 at all Upper Gabus Massive reservoirs except UG Massive sand which possibly due to tuning thickness. Also the same thing, the grey color is consistently coloring the non pay zone which could be shale, wet sand or shaly sand. The arbitrary section crossing RAF-3 to NE RAF-1 shows the red and grey color distribution across the structures (figure 5.6)

5.2.1 Blind Well Tests

This step is done to confirm whether the RPT applied that derived from 2 wells: RAF-3 and NE RAF-1 is also working well to predict the fluid content at the wells that excluded from the simultaneous inversion process. They are RAF-2, RAF-A01 and RAF-A02.

Figure 5.7 shows that the RPT has worked well to predict the fluid content on those wells at almost all Upper Gabus Massive reservoir. However on particular reservoir UG Massive sand at RAF-A01 and RAF-A02 are not colored by the red, this possibly due to overlap zone on the poor discriminated area while UG Massive sand at RAF-2 is possibly due to tuning thickness.

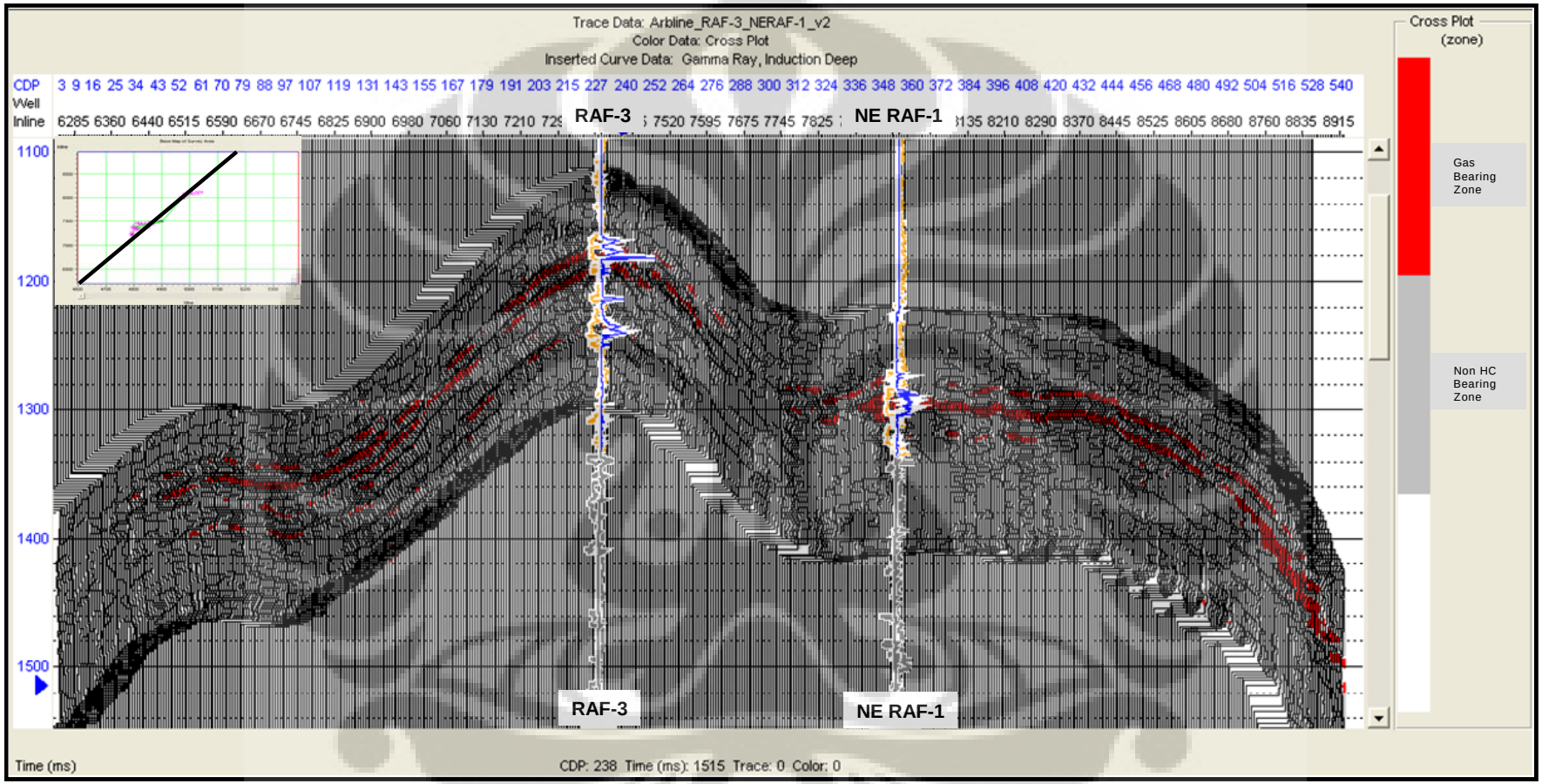

Figure 5.6 Arbitrary section crossing RAF-3 to NE RAF-1 shows the red and grey color distribution across the structures

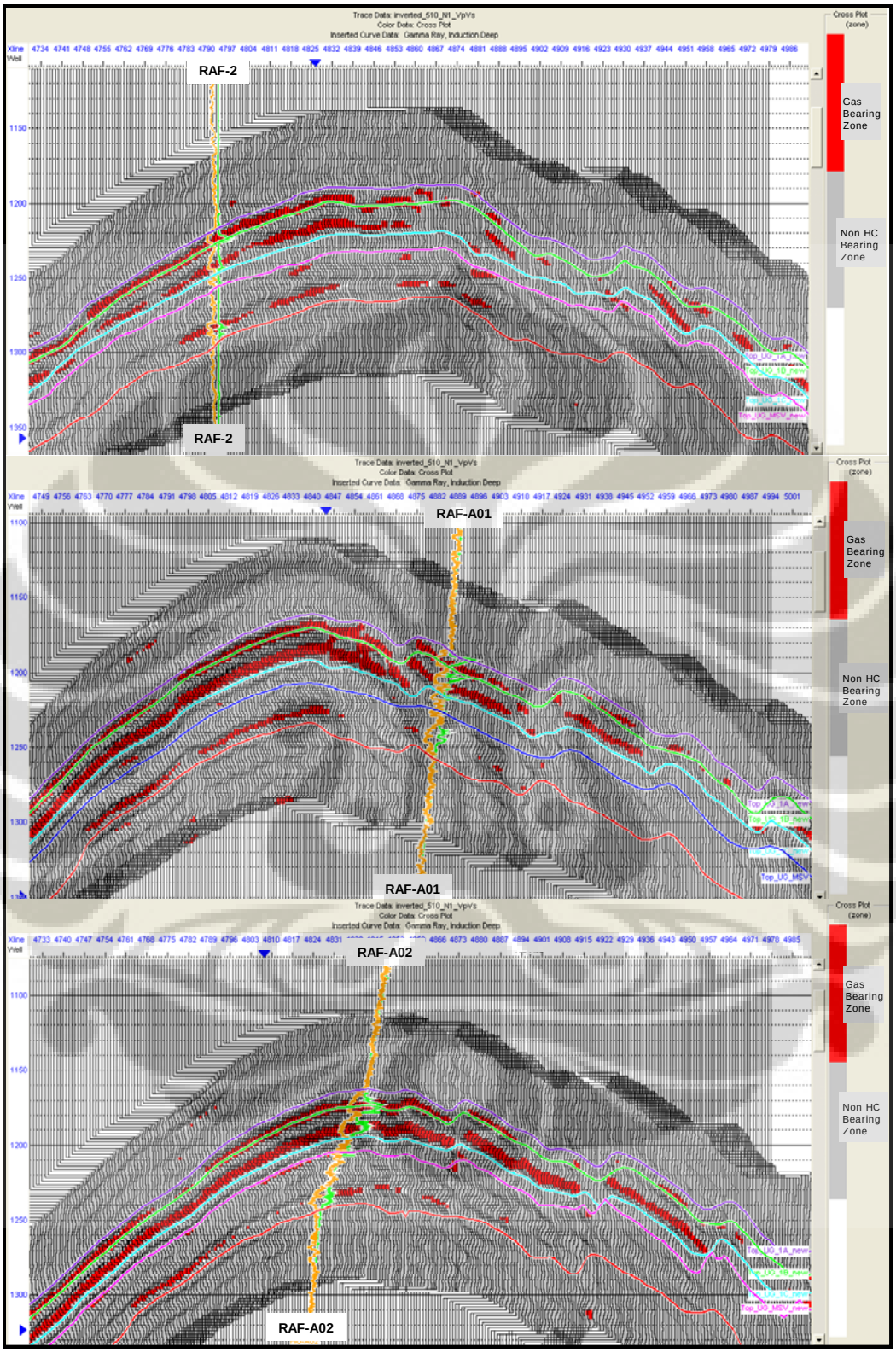

Figure 5.7 Seismic sections overlaid by cross plot zoning at RAF-2, RAF-A01 and RAF-A02 well location

5.2.2 Horizons Slicing

After reviewing the gas bearing and non-HC bearing zones distribution in vertical section, it is also a need to see the zones distribution laterally by generating horizon slice for some horizon intervals. Figure 5.8 shows horizon slice at Top UG-1A and Top UG-1B interval reflecting gas accumulation distribution at UG-1A sand. It is seen the distribution forming the low sinuosity channel like trend.

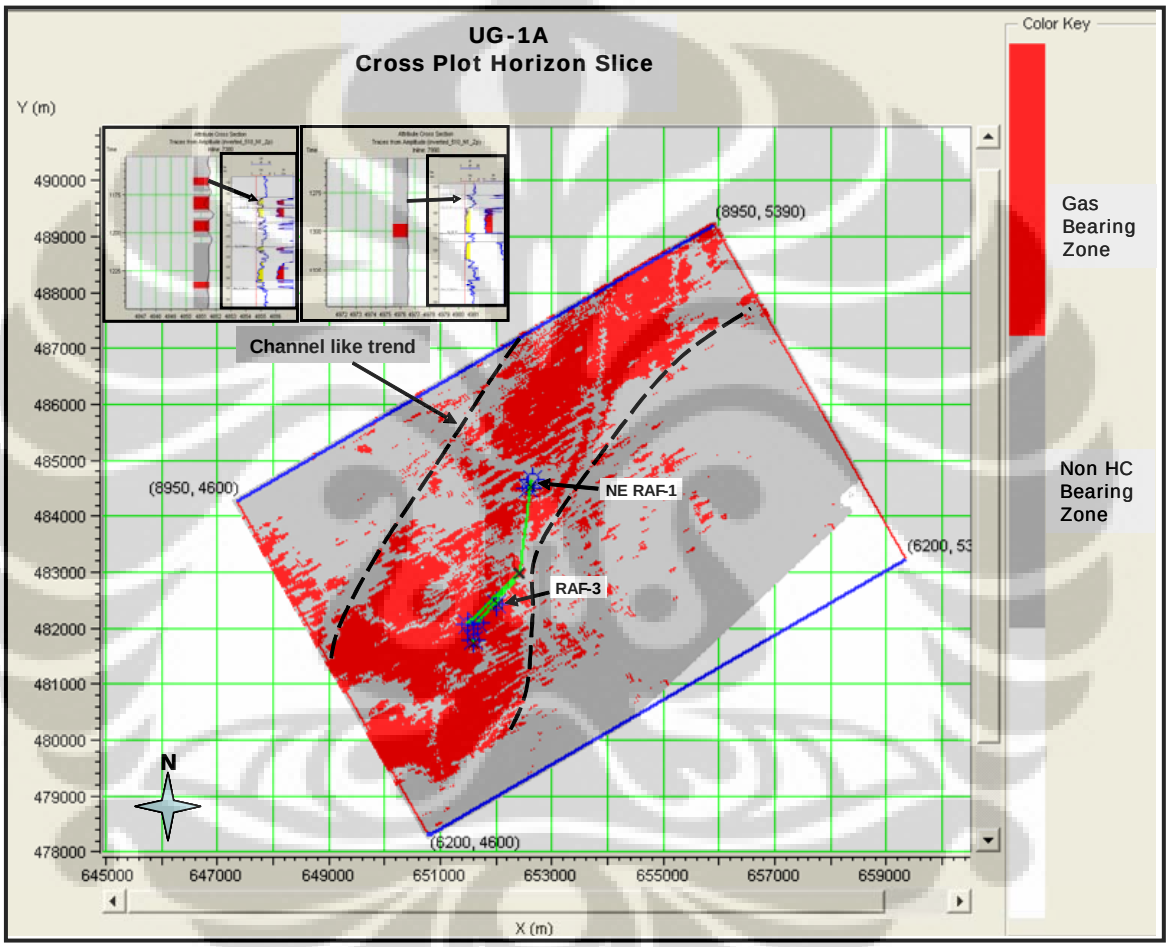

Figure 5.8 Horizon slice at Top UG-1A and Top UG-1B interval showing channel like trend gas accumulation distribution.

A separated gas accumulation distribution between RAF structure and NE RAF structure is shown on figure 5.9 which reflecting gas accumulation on stack of UG-1B and UG-1C sand. A less of gas accumulation distribution is seen on figure 5.10 which reflecting the gas accumulation on UG Massive sand. This is possibly due to lack of gas content or due to tuning effect or overlap zone on the poor discriminated area cross plot.

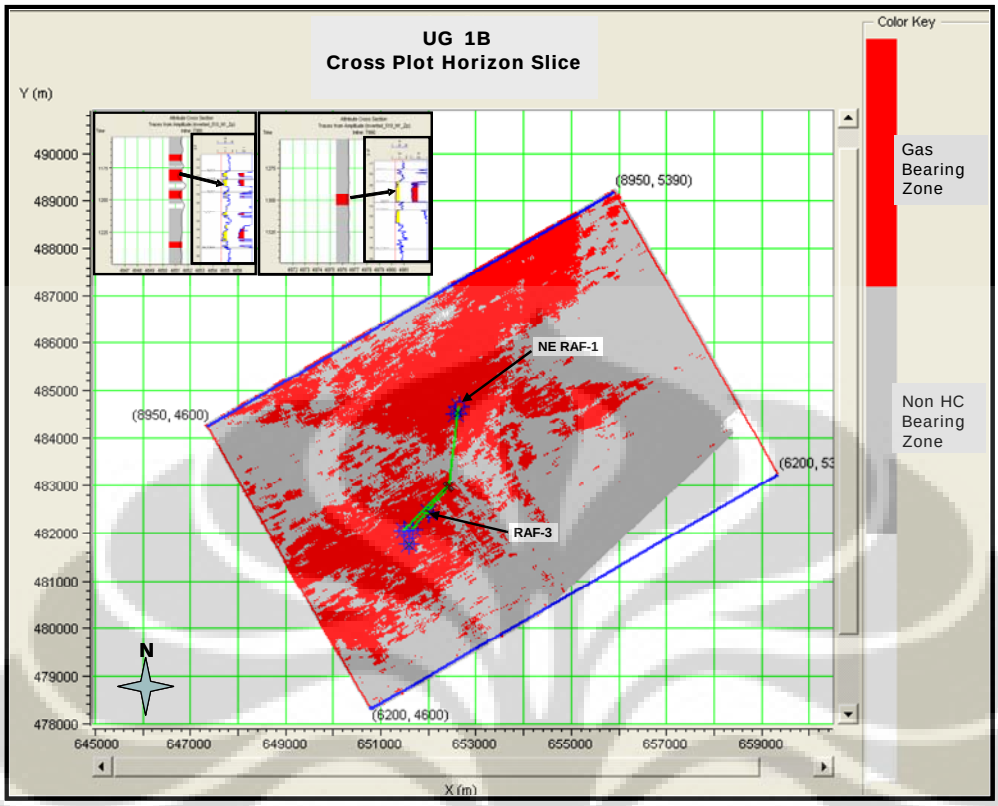

Figure 5.9 Show gas accumulation distribution on stack of UG-1B and UG-1C sand.

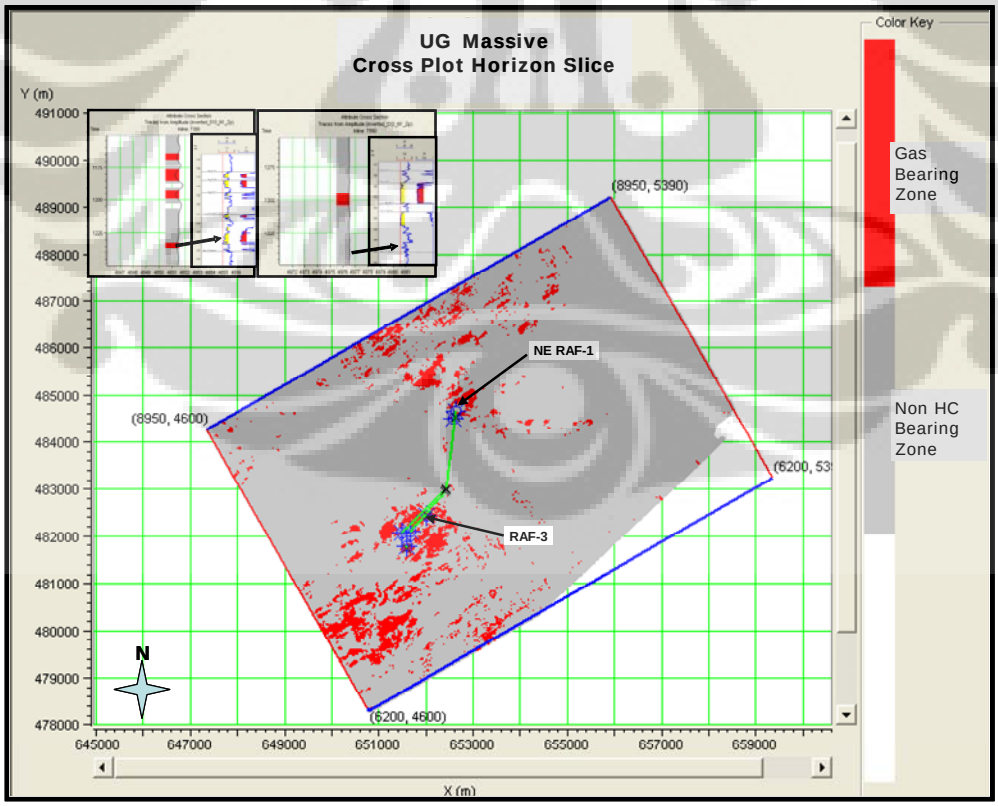

Figure 5.10 Less gas accumulation distribution on UG Massive sand.

5.3 Sand Prediction

Sand prediction is generated through creating VShale volume. By plotting Density (ρ) against VShale and Porosity as the color point from the known logs of RAF-3 and NE RAF-1, it can be concluded that the lower left quadrant is clean sand and good quality (porosity) sand (figure 5.11). This allows us to calculate the Sand % volume from the Inversion Density volume by generating regression linear at clean sand trend where minimum and maximum VShale value is constrained at 0.01 to 0.6. The program then calculates its regression linear equation

y = 0.657447x + 2.09292 or

x = (y – 2.09292)/ 0.657447

where: y = Density and x = VShale

So we will have VShale volume derived from Density volume

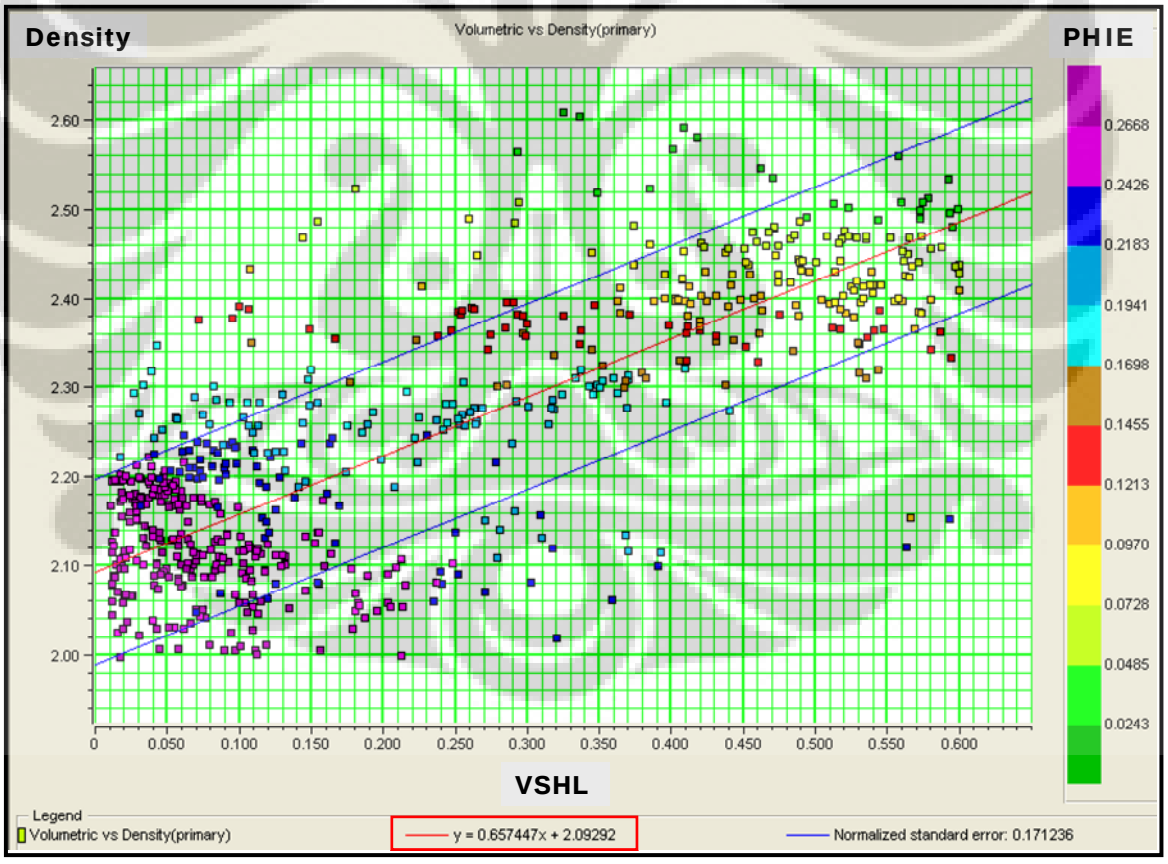

Figure 5.11 Cross plot Density (ρ) vs VShale of RAF-3 and NE RAF-1 showing regression linear at clean sand trend and good quality (porosity) sand zone (yellow box).

Based on VShale volume, we can predict laterally the clean and good quality sand distribution at reservoir levels by slicing the volume guided by the seismic horizons. Figure 5.12 shows predicted sand distribution at UG-1A sand where dominantly concentrated at RAF structure. While good lateral of sand distribution prediction is demonstrated at UG-1B (figure 5.13). The predicted distribution is occupied at both RAF and NE RAF structure. Sand distribution at NE RAF structure is getting diminished at UG-1C and UG Massive as shown in figure 5.14 and 5.15. Th lateral sand distribution prediction of these 4 reservoirs in RAF and NE RAF structure: UG-1A, UG-1B, UG-1C and UG Massive are consistent to vertical sand distribution described by the well correlation of all wells in RAF field shown in figure 2.6 of Chapter 2.

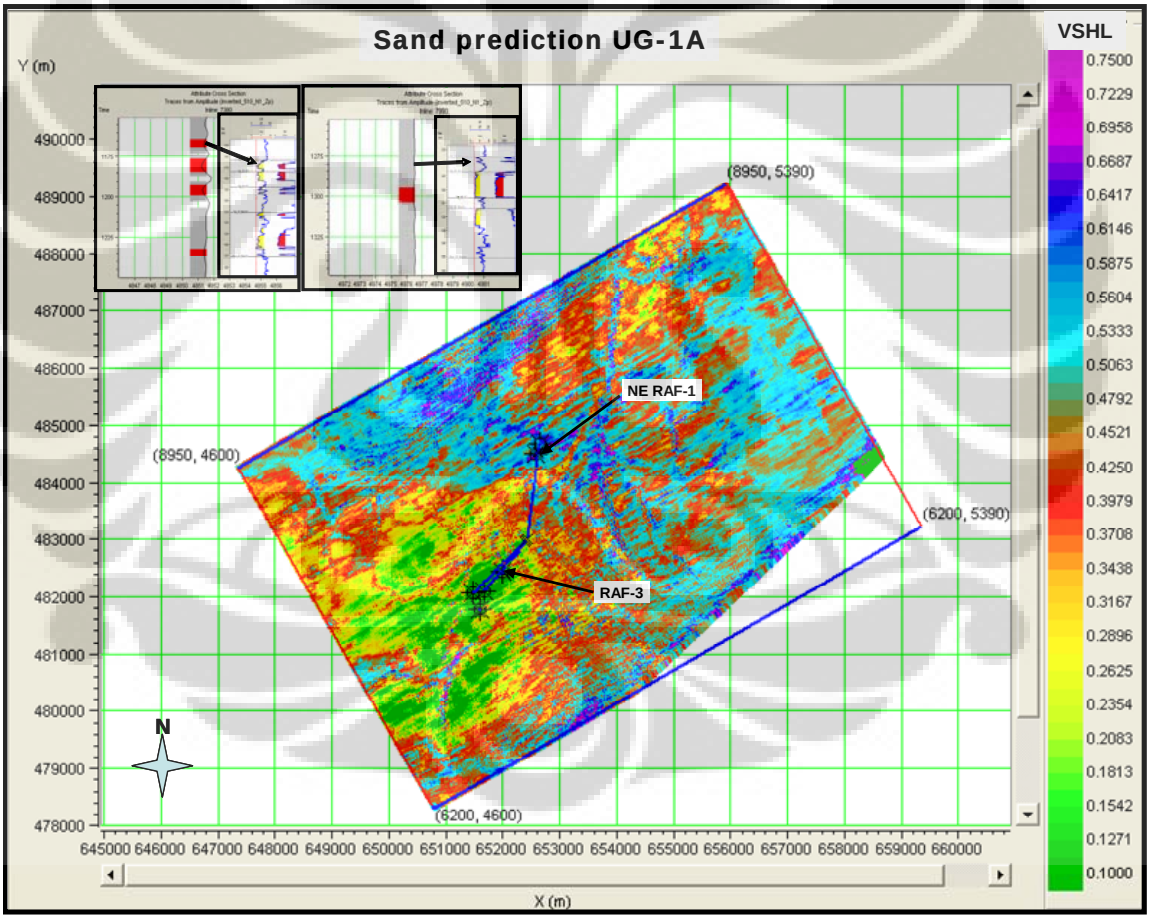

Figure 5.12 Sand prediction at UG-1A interval where clean and good quality sand is concentrated at RAF structure.

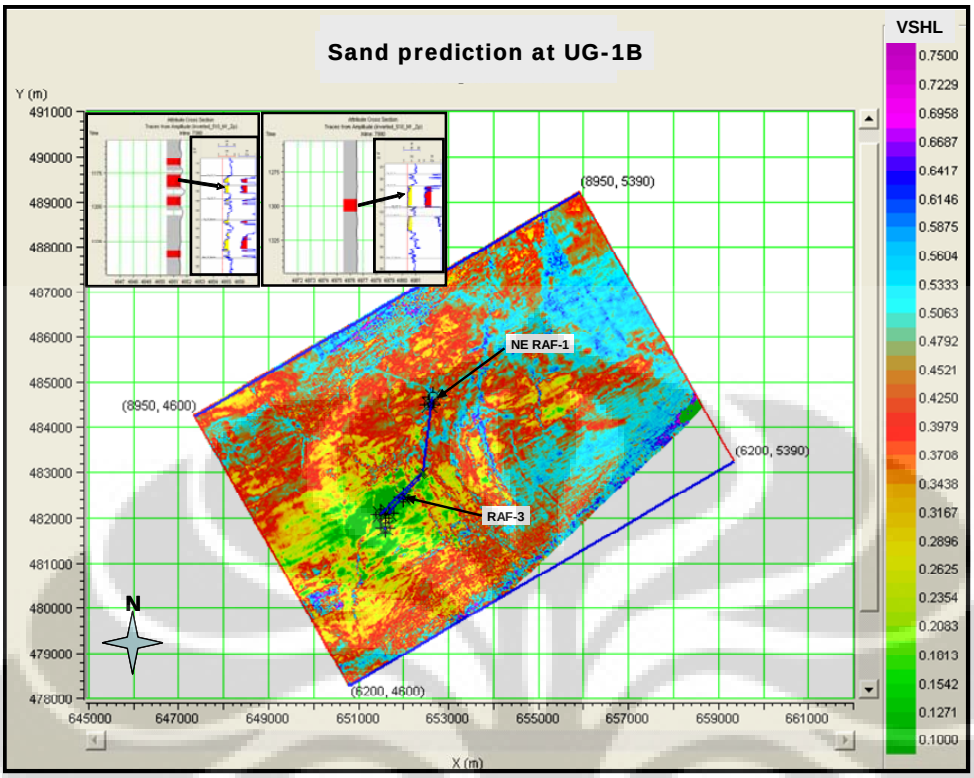

Figure 5.13 Sand distribution prediction at UG-1B interval

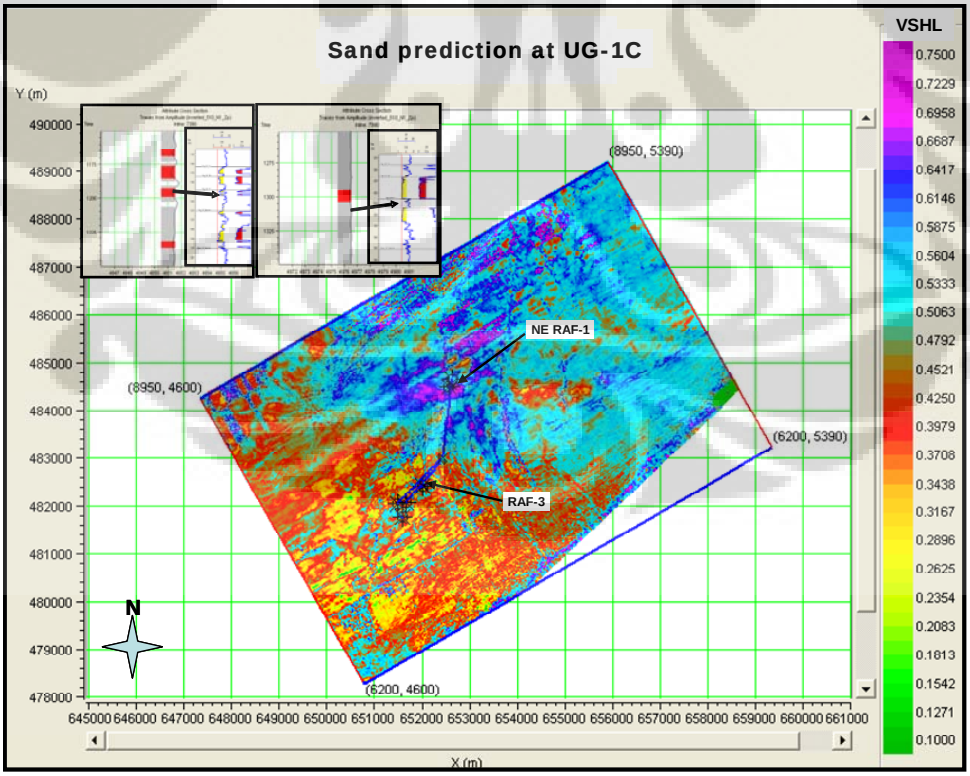

Figure 5.14 Sand distribution prediction at UG-1C interval where sand diminished at NE RAF structure

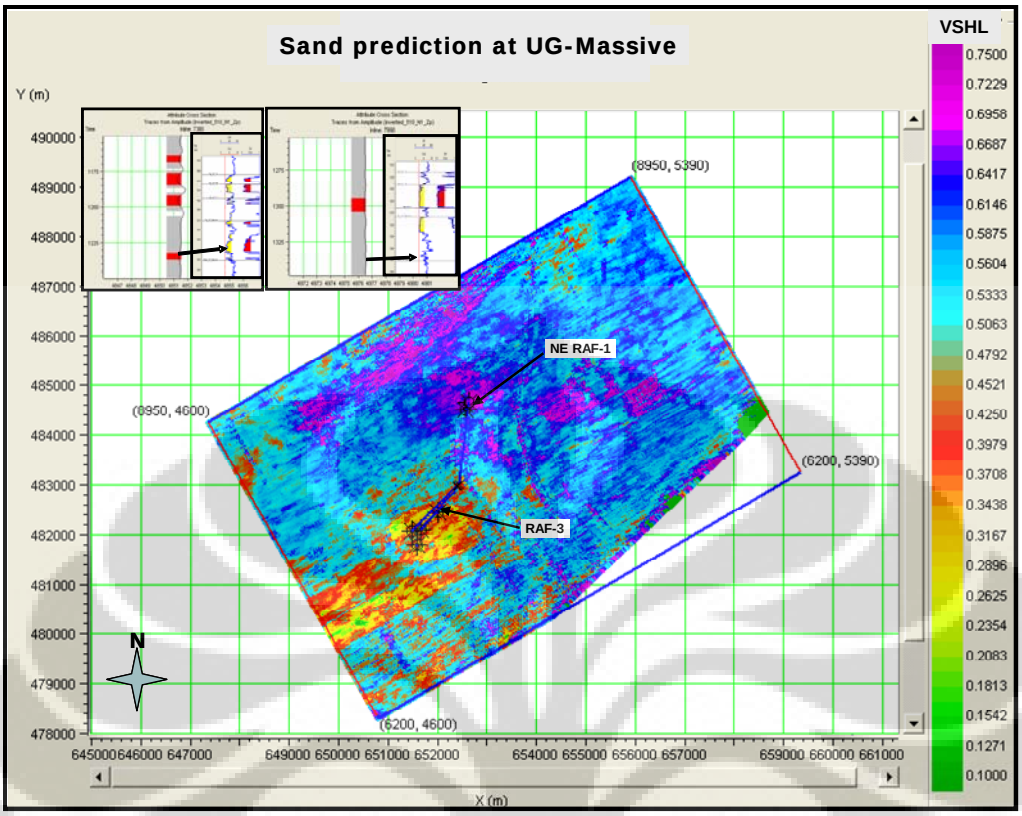

Figure 5.15 Lesser sand distribution of UG Massive interval at RAF structure

5.4 Porosity Prediction

Porosity prediction is generated through Porosity volume created using P-impedance volume. By plotting PHIE (Effective porosity) against P-impedance and Saturation Water as the color point from the known logs of RAF-3 and NE RAF-1, it can be derived 2 porosity trends: Pay and Wet trend (figure 5.16). This allows us to calculate the Porosity volume from the Inversion P-impedance volume using regression linear equation at the Pay trend:

$$y = -1.76575*10^{-5}\, x + 0.6303107$$

where y = Porosity and

x = P-impedance

And we will have Porosity volume derived from P-impedance volume.

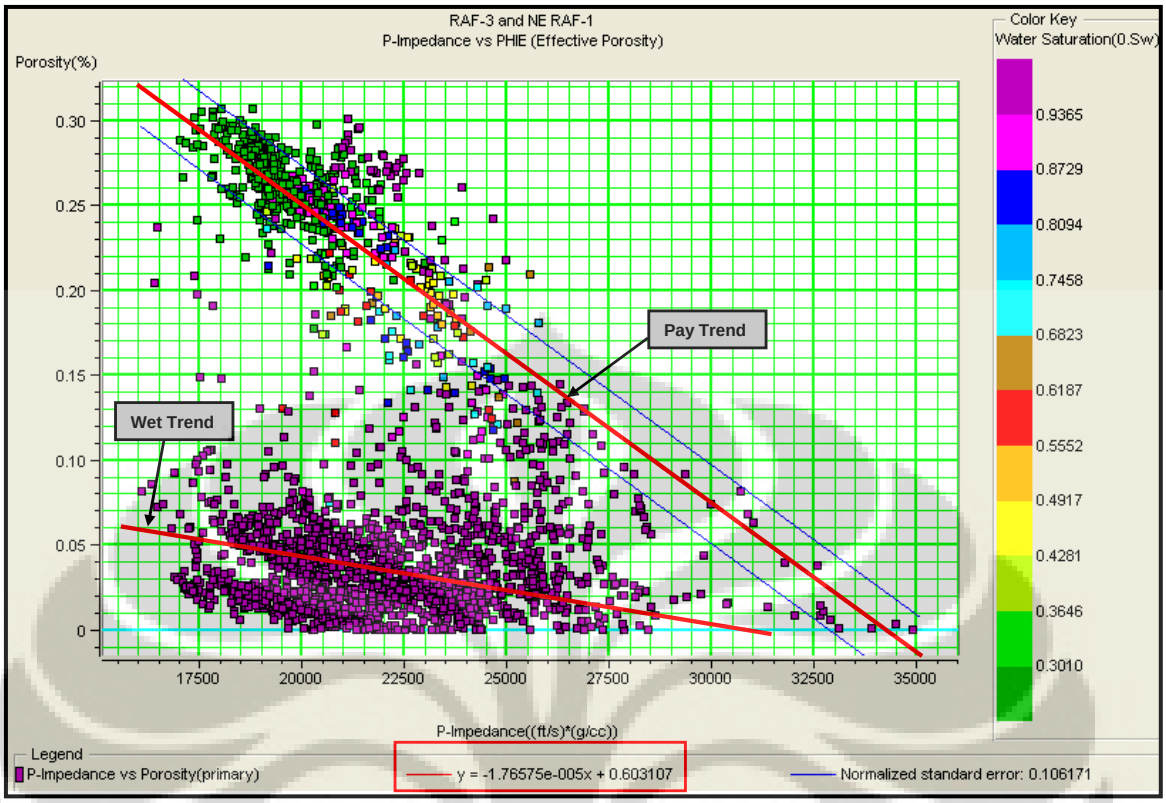

Figure 5.16 Two (2) Porosity trends derived from cross plot PHIE against P-impedance

As follow, based on Porosity volume, laterally we can predict good porosity sand distribution at reservoir levels by slicing the volume guided by the seismic horizons. Figure 5.17 – 5.20 show porosity distribution prediction equivalent at UG-1A, UG-1B, UG-1C and UG Massive interval. It looks the porosity distribution trend is following the sand distribution prediction

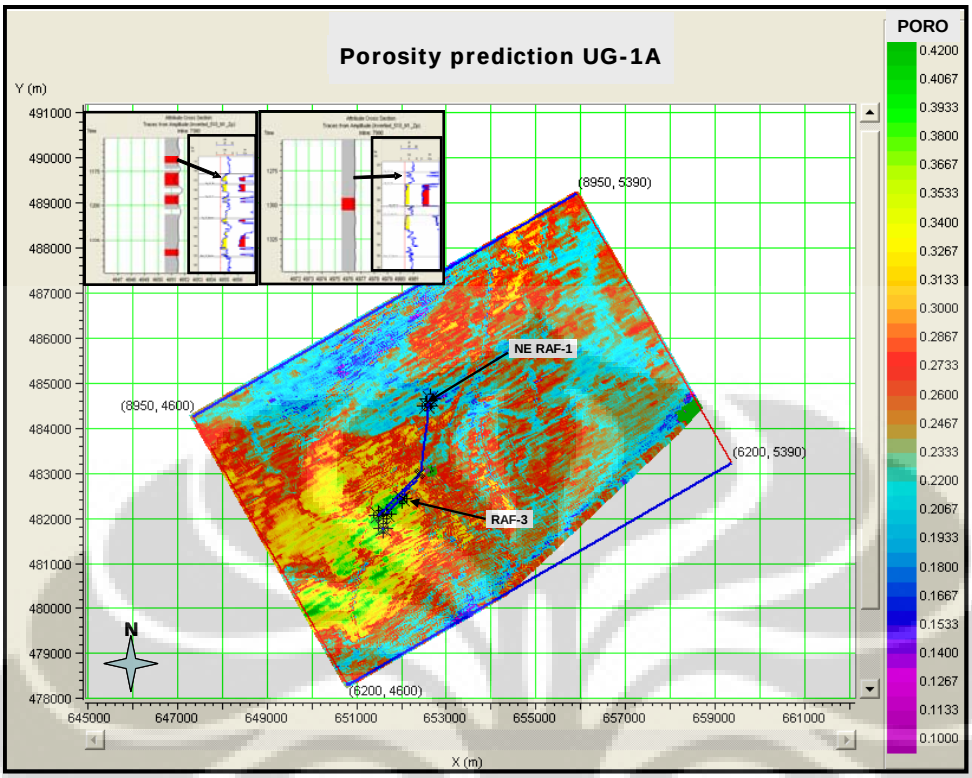

Figure 5.17 Porosity distribution prediction of UG-1A interval

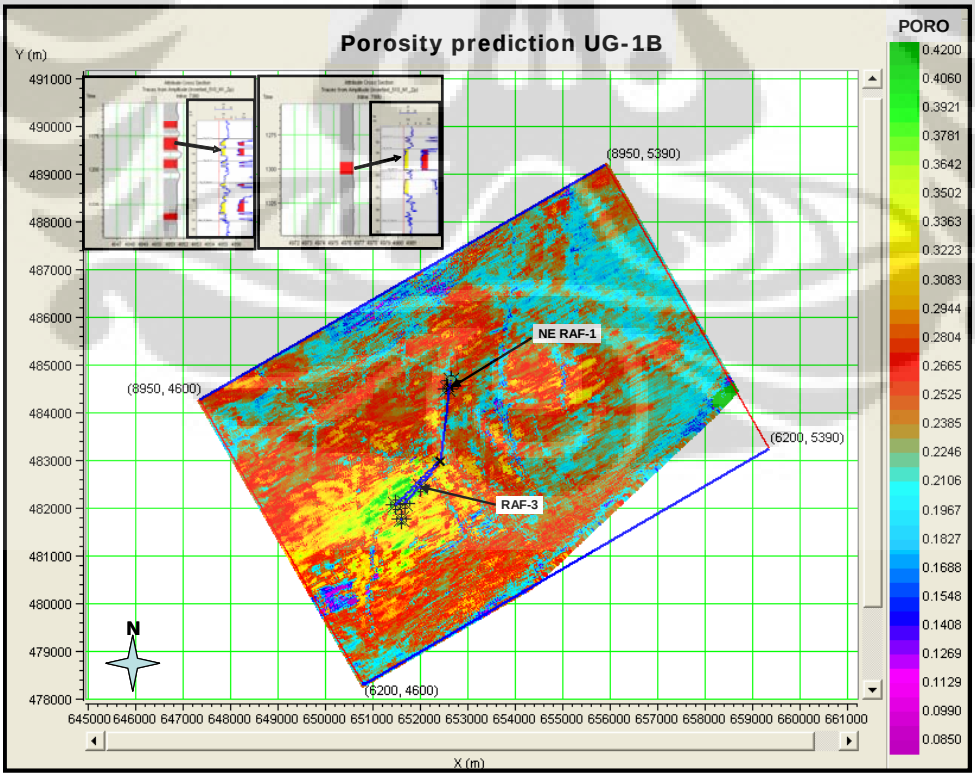

Figure 5.18 Porosity distribution prediction of UG-1B interval

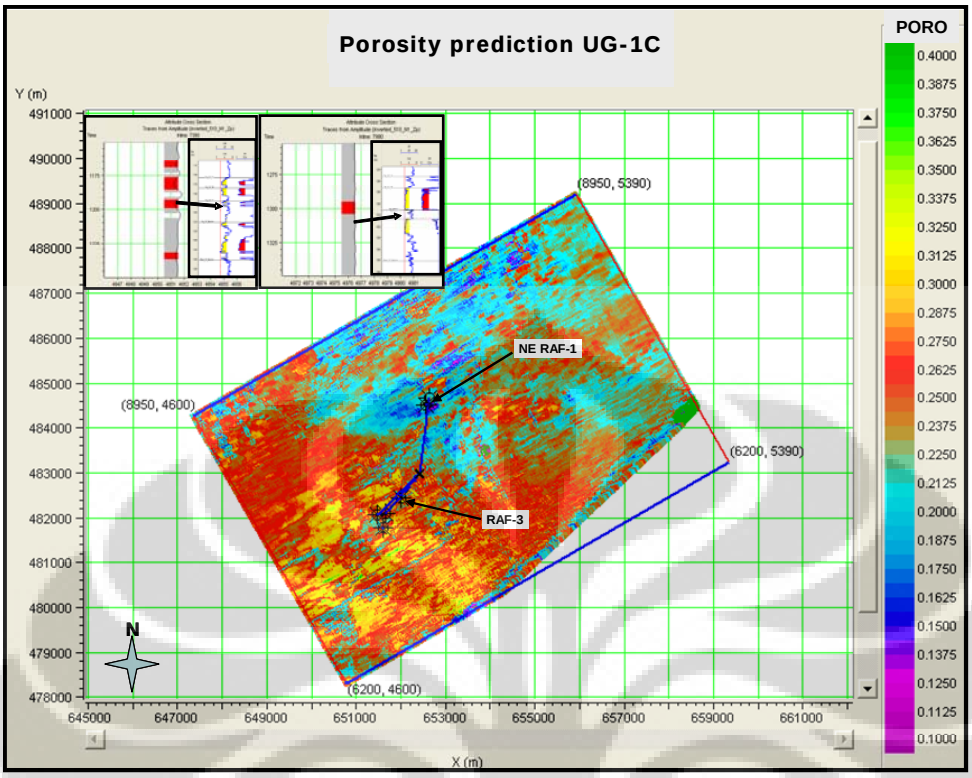

Figure 5.19 Porosity distribution prediction of UG-1C interval

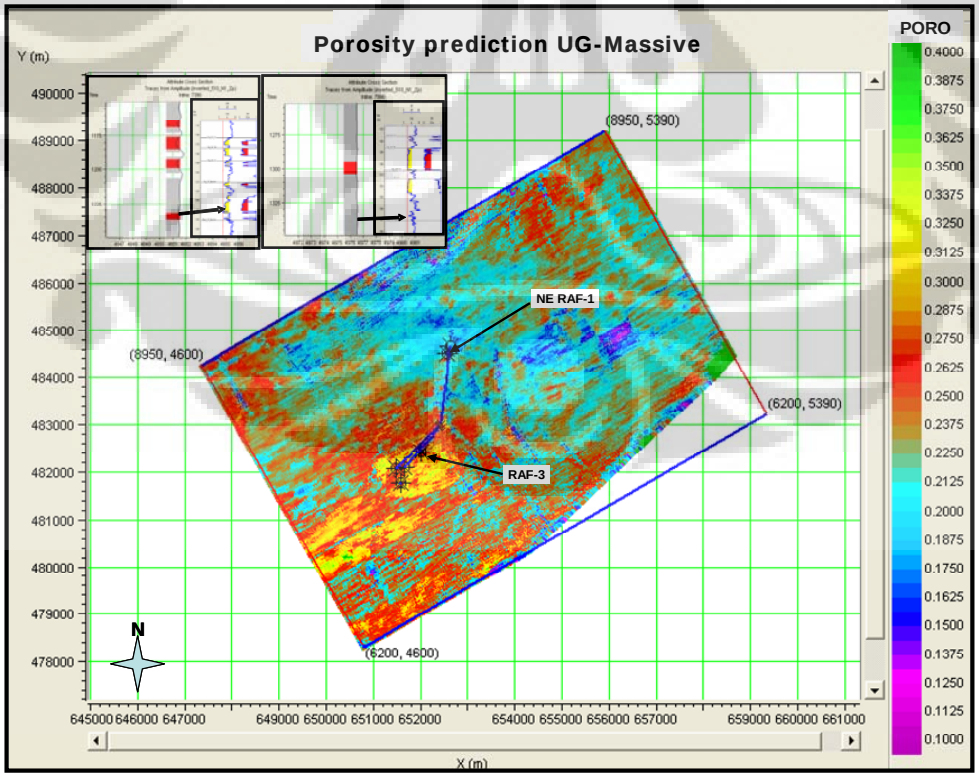

Figure 5.20 Porosity distribution prediction of UG-Massive interval

5.5 Pore Gas Prediction

Pore gas distribution is predicted through Lamda-Rho volume which generated from P-impedance and S-impedance volume using equation 10 in Chapter 3:

$$\lambda\rho = Z_P^2 - 2Z_S^2$$

where: $\lambda\rho$ = Lamda-Rho Z_P = P-impedance Z_S = S-impedance

As discussed in Chapter 3, Lamda-Rho or Incompressibility is a measure of the physical response of volume changing when given the stress. This changing is more caused by changing in pore and its fluid rather than changing in grain size. The easier the medium are compressed, the lower the incompressibility value will be. Low incompressibility values are associated with gas sand therefore Lamda-Rho is a good indicator for pore gas content. Figure 5.21 – 5.24 show pore gas distribution prediction at equivalent to the reservoir sands.

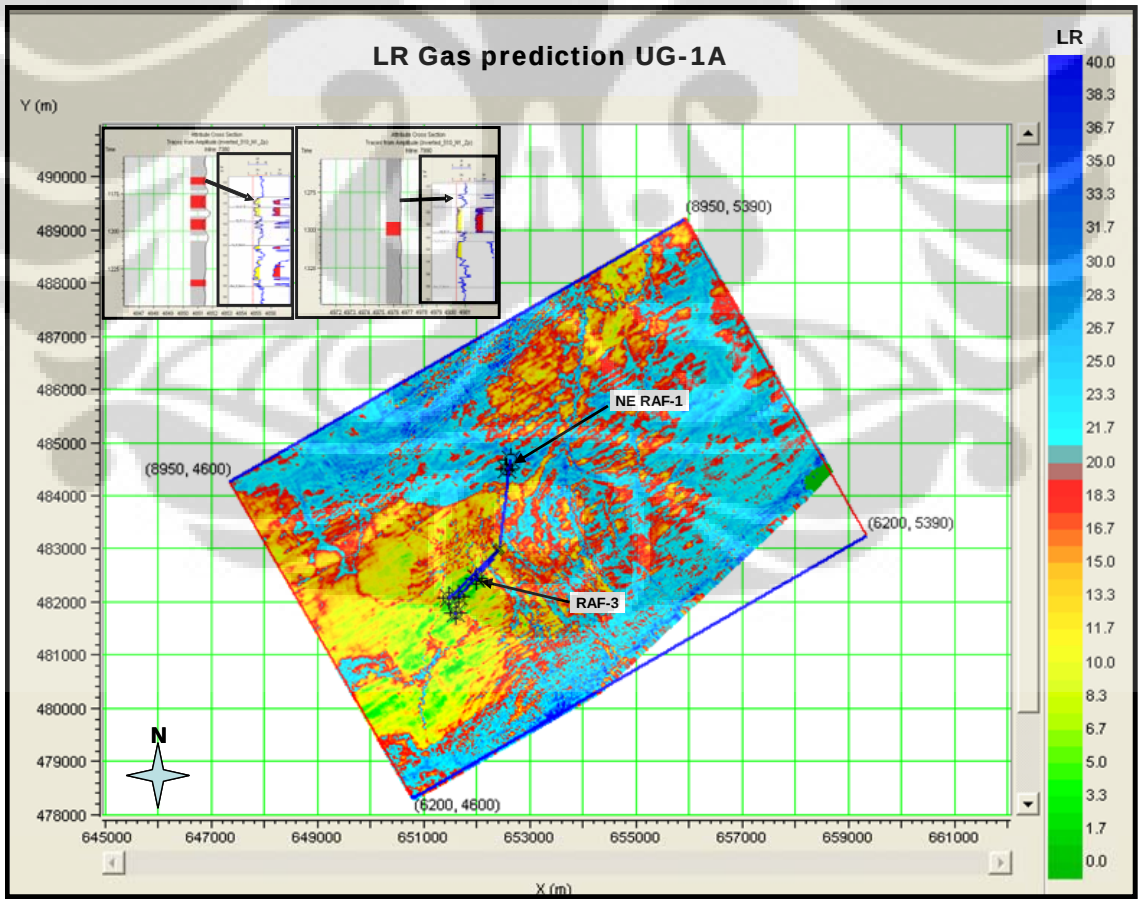

Figure 5.21 Pore gas distribution prediction of UG-1A interval

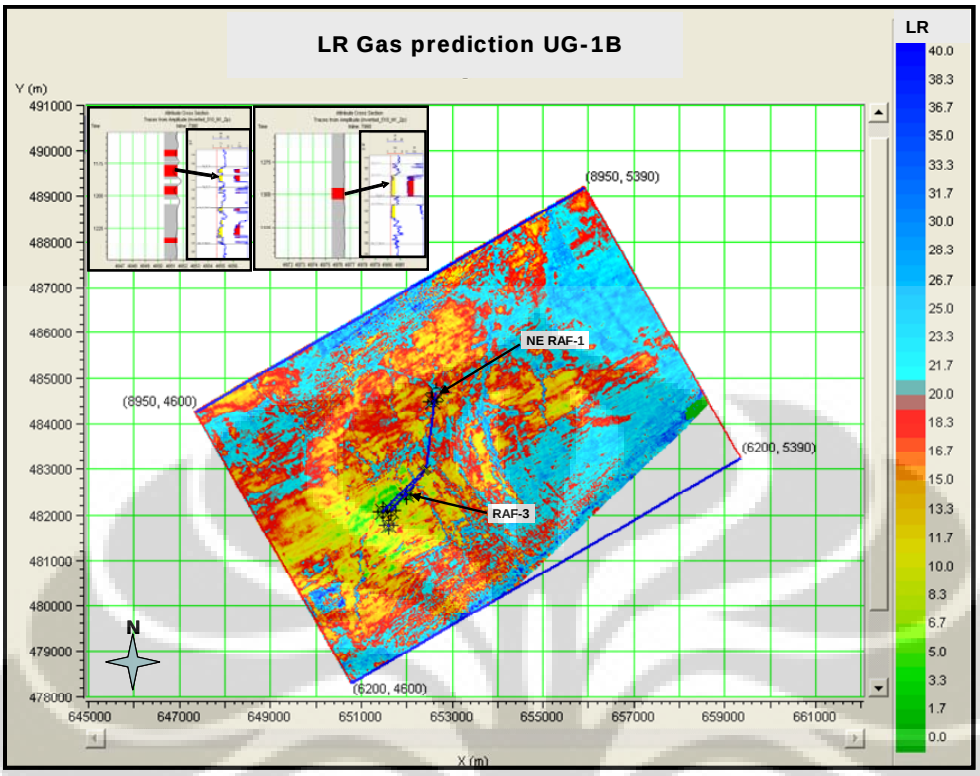

Figure 5.22 Pore gas distribution prediction of UG-1B interval

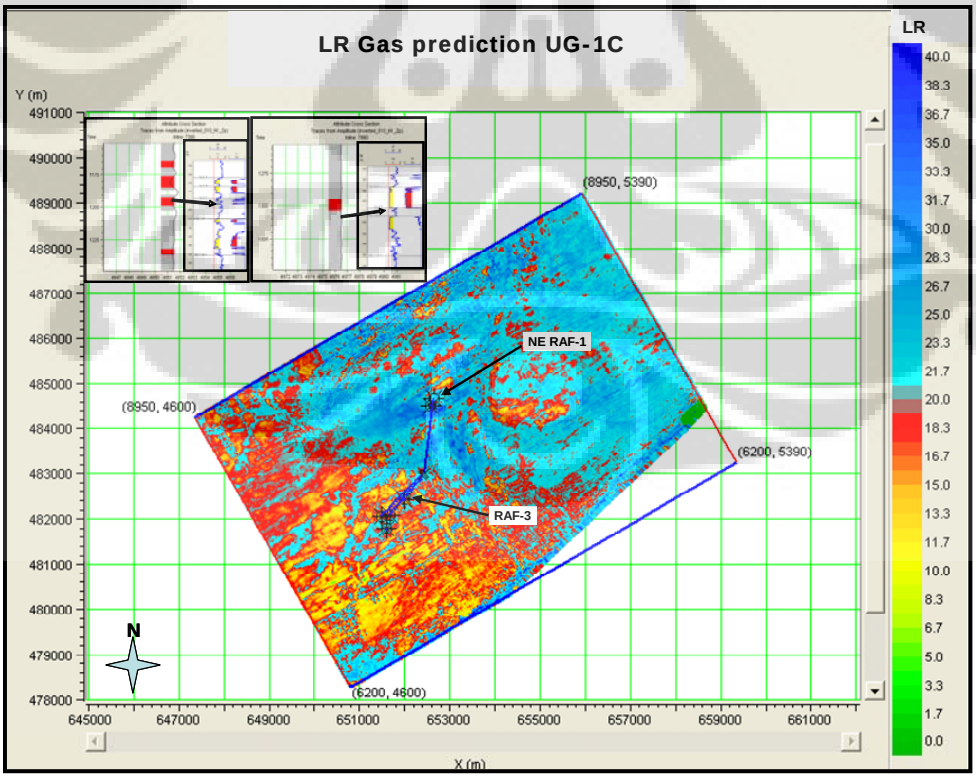

Figure 5.23 Pore gas distribution prediction of UG-1C interval

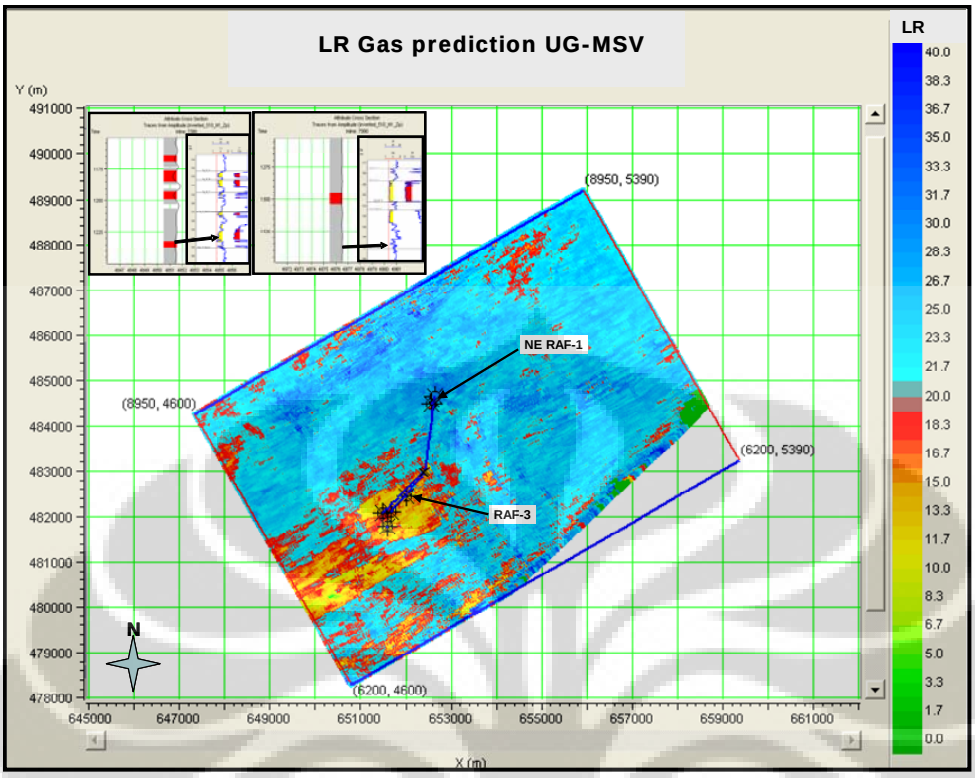

Figure 5.24 Pore gas distribution prediction of UG-Massive interval

5.6 Water Saturation Prediction

Water saturation prediction is calculated by using the Inversion Density volume and the Derived Porosity volume, in Wyllie's formula (equation 11 in Chapter 2):

$$\rho = \text{ø}\left((1 - S_w)\,\rho_{Gas} + S_w\,\rho_{Water}\right) + (1 - \text{ø})\,\rho_{Matrix}$$

where:

ρ_{Gas} = 0.68 (avg based on PVT test) ρ_{Matrix} = 2.65 ρ_{Water} = 1

or

$$S_w = \frac{\left(\rho - \rho_{Matrix} + \text{ø}\,(\rho_{Matrix} - \rho_{Gas})\right)}{\text{ø}\,(\rho_{Water} - \rho_{Gas})}$$

And we will have water saturation volume to be used for horizons slicing to predict its lateral distribution at reservoir level. Figure 5.25 – 5.28 show water saturation distribution prediction at equivalent to the reservoir sands.

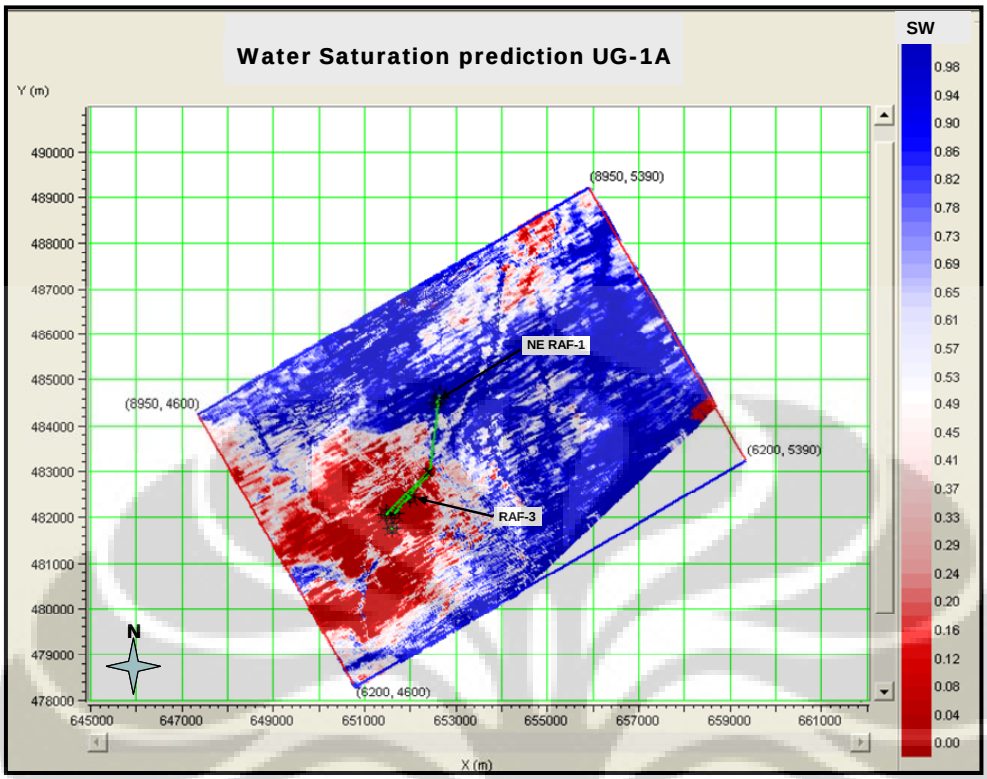

Figure 5.25 Water Saturation distribution prediction of UG-1A interval

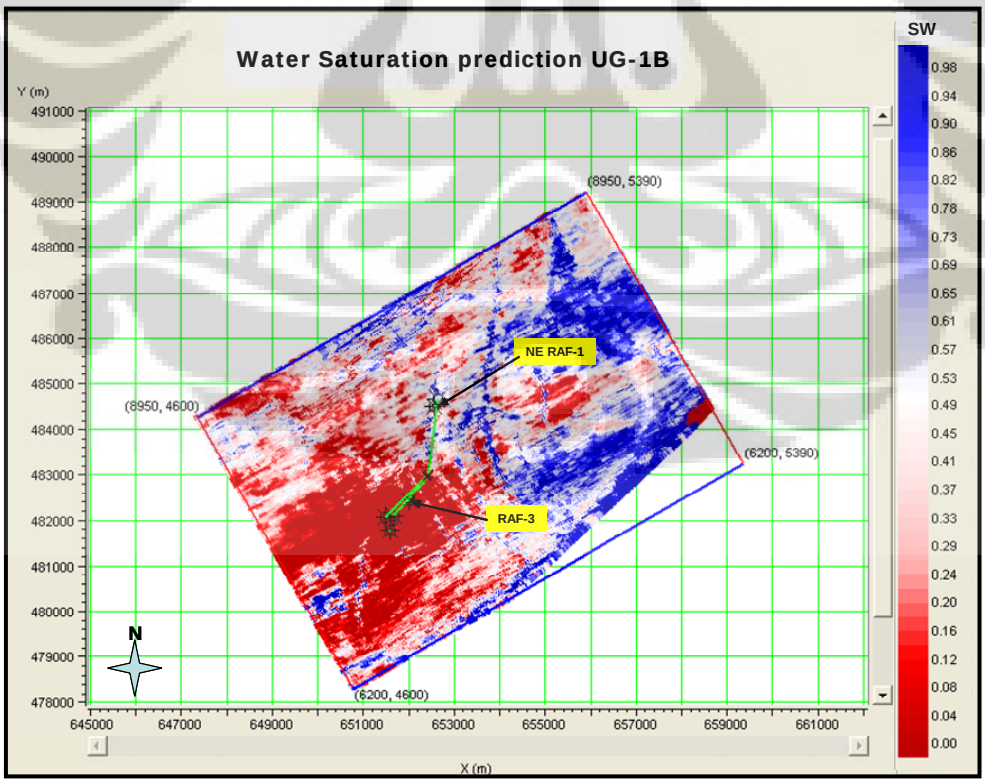

Figure 5.26 Water Saturation distribution prediction of UG-1B interval

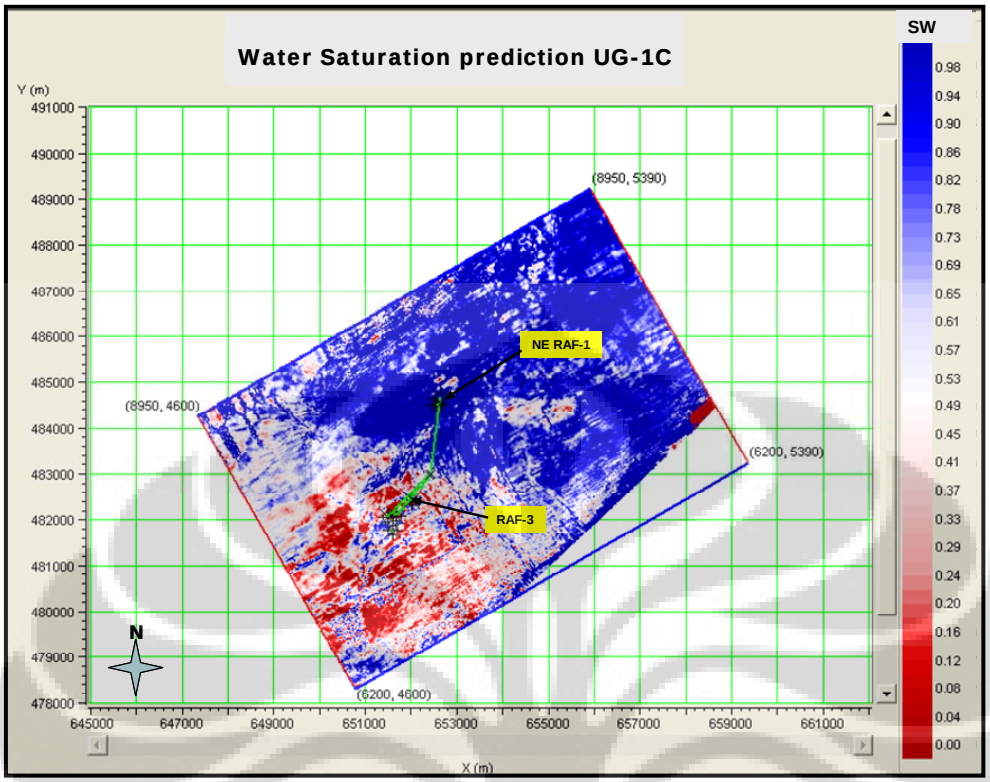

Figure 5.27 Water Saturation distribution prediction of UG-1C interval

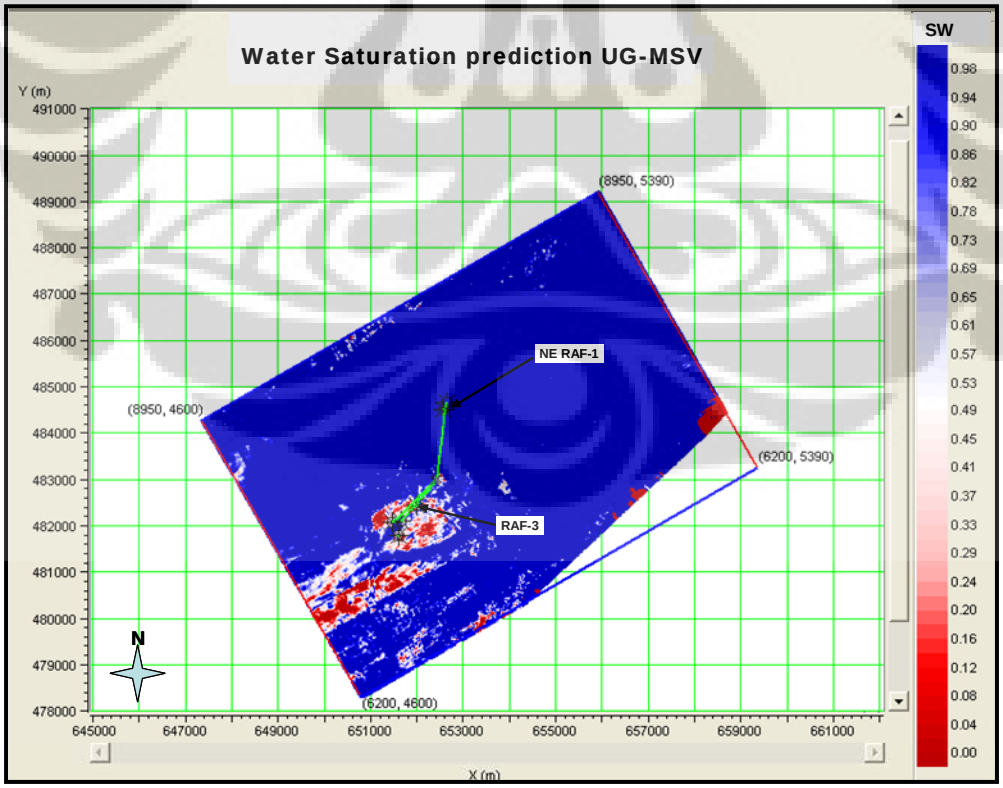

Figure 5.28 Water Saturation distribution prediction of UG-Massive interval

5.7 Potential Area Identification

Based on the observation of data analysis and interpretation techniques result above, it can be summarized that good quality sand and gas accumulation of Upper Gabus formation at RAF field consistently are distributed widely at UG-1A and UG-1B interval. And when these intervals are overlaid with its structural contour and fault, it can be identified the prospective areas which potentially un-drained by the existing producing wells which might be due to the fault trap. The existing producing wells are RAF-A02 which was designed to drain Upper Gabus formation and RAF-04: horizontal well which was specifically designed to drain UG-1B, while RAF-A01 was designed to drain the other lower formations at this field. This identification might support the strategy for further development of optimizing the hydrocarbon recovery from this field.

Figure 5.29 – 5.32 show the overlying structure maps and its fault associated on Sand and gas prediction map of UG-1A and UG-1B interval. They also show 2 potential areas: at Eastern flank of RAF structure and at Northwest of NE RAF structure nose.

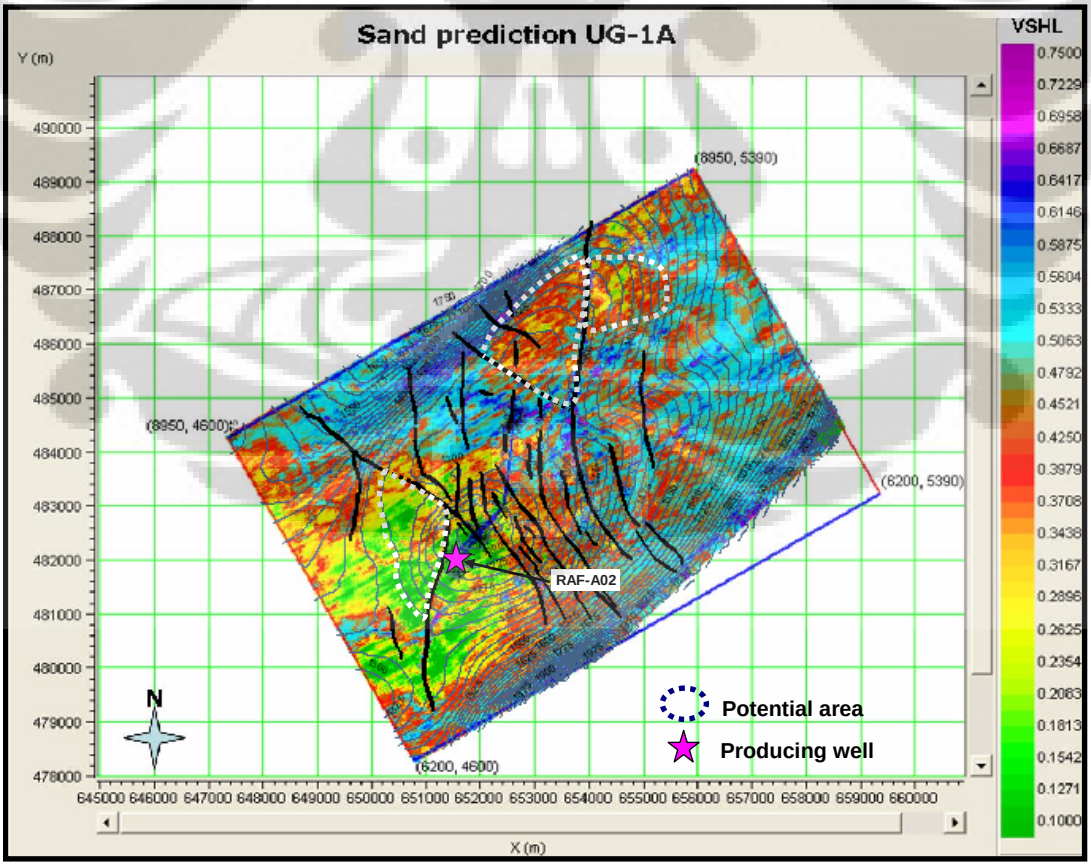

Figure 5.29 Potential areas at UG-1A based on Sand prediction map

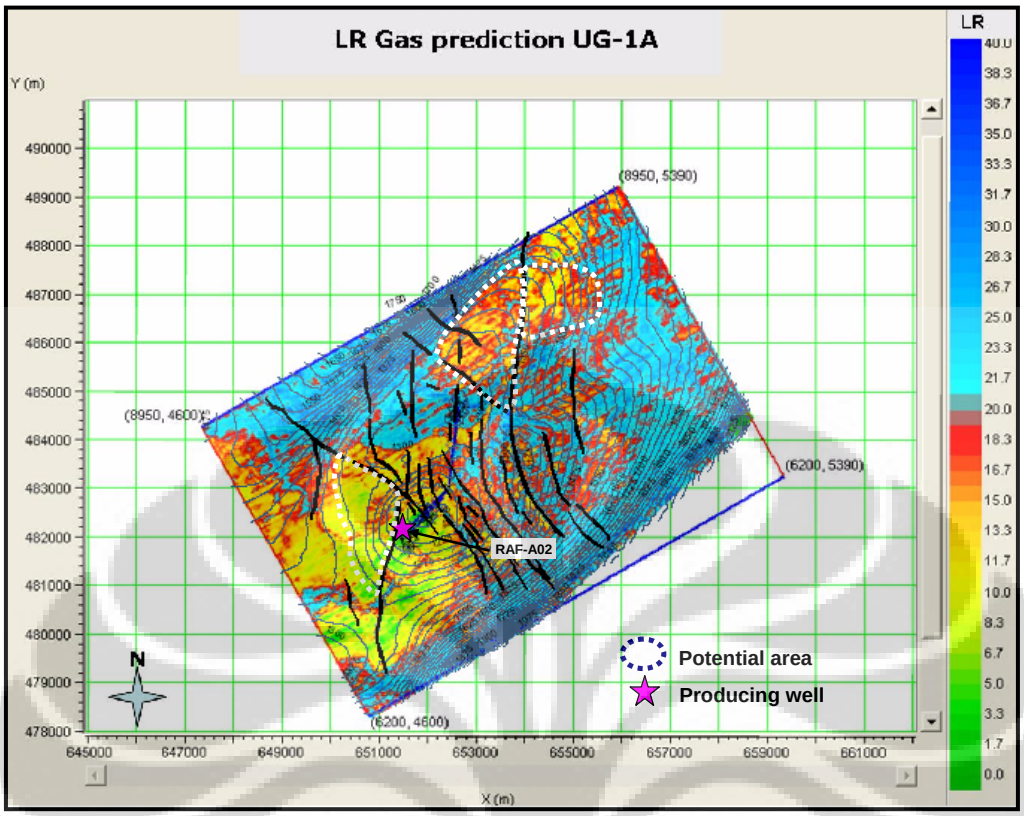

Figure 5.30 Potential areas at UG-1A based on Lamda-Rho pore gas prediction map

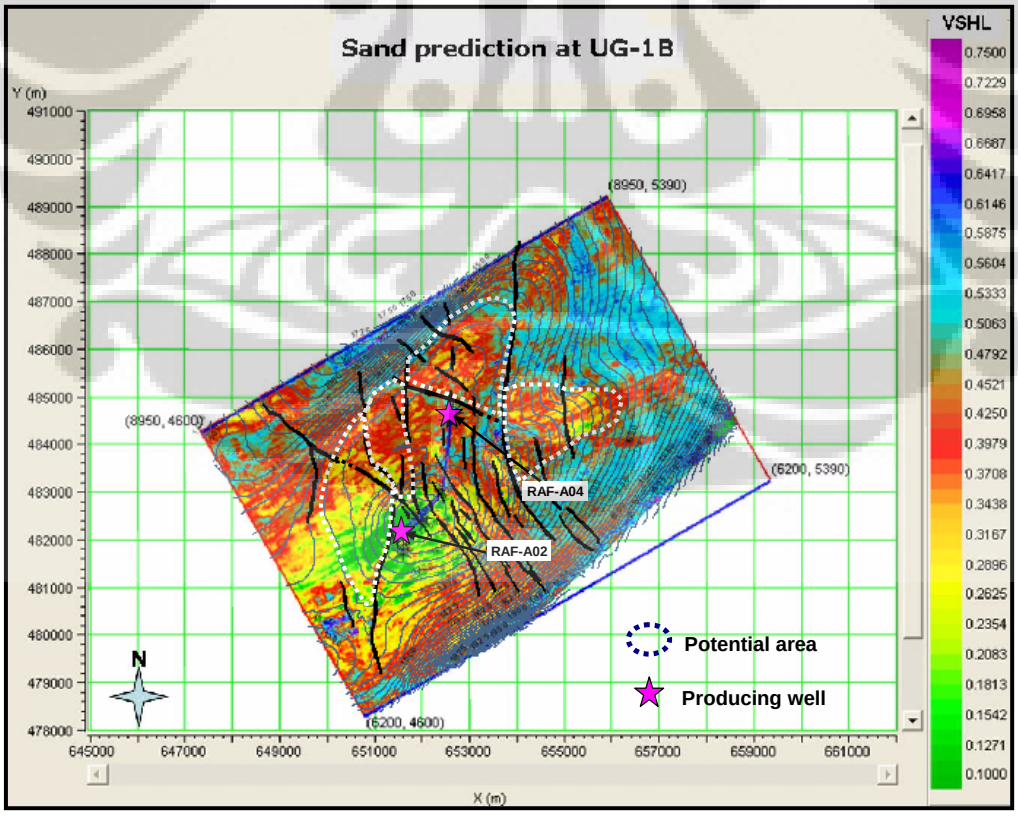

Figure 5.31 Potential areas at UG-1B based on Sand prediction map

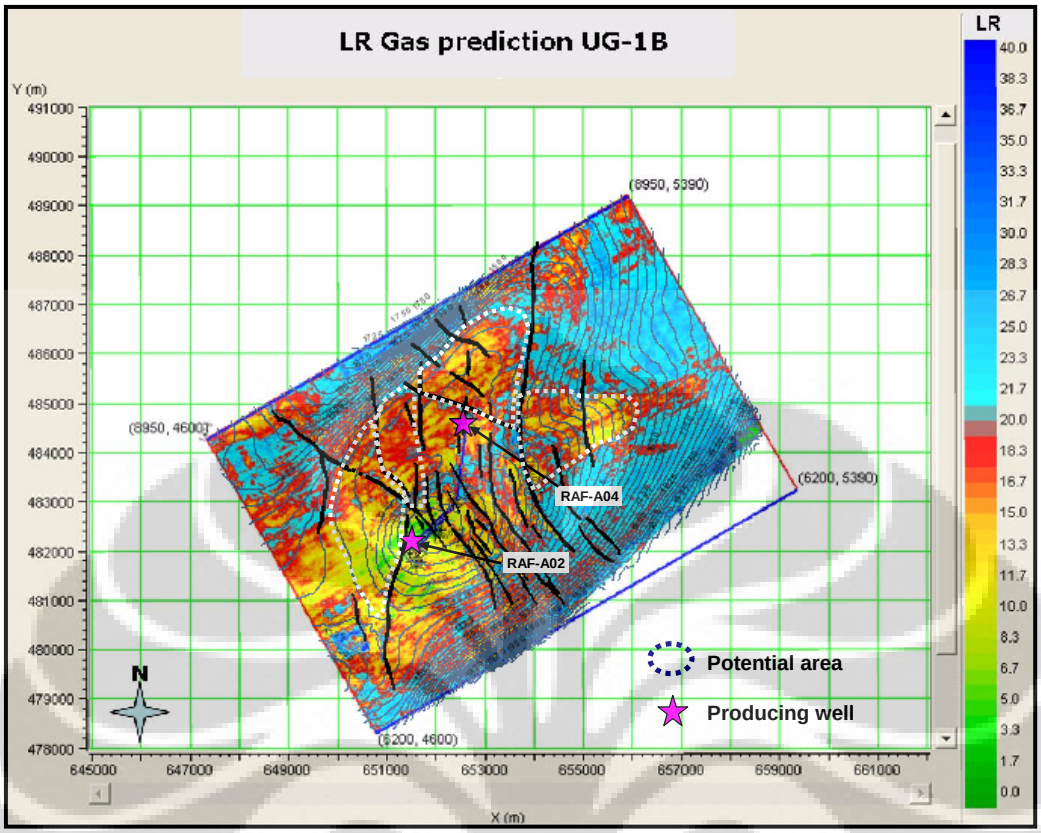

Figure 5.32 Potential areas at UG-1B based on Lamda-Rho pore gas prediction map

Chapter Six:
CONCLUSION AND RECOMMENDATION

Through this thesis and its data analysis and interpretation, it can be concluded a few things especially relate to the thesis objectives and hypothesis as mentioned in the earlier chapter.

6.1 Hypothesis versus Result

1. The hypothesis that there is a relationship between rock physics (Z_P, Z_S, V_P/V_S, $\lambda\rho$, $\mu\rho$) and rock properties (Density, Porosity, Gas saturation, Shale Volume) on data in study area could be proven empirically through feasibility study and data analysis where P-impedance correlate to Porosity, Lamda-rho, P and S-impedance and also V_P/V_S crossplot are correlate indirectly to lithology and gas saturation.
2. The hypothesis that Seismic Simultaneous inversion method is feasible to be applied in study area and can be used to estimate a reliable P-impedance, S-impedance and Density volumes could be can proven through the feasibility study where the seismic data in this study area still can resolve some main reservoirs at the Upper Gabus formation and also through Pre-inversion QC Analysis which giving a good coefficient correlation and similar trend between inverted result logs and the original log at the well location. The analysis of the inversion product including blind well tests has been proving that the result is consistent with the actual gas presence observed from the existing wells in the study area.
3. The hypothesis that Seismic Simultaneous Inversion derivative product and its combination with rock physics techniques allow us to have qualitative and quantitative analysis to predict and estimate the desired reservoir characters such as porosity, gas distribution, its geometry and connectivity could be achieved through cross plot volume section and slice, Sand, Porosity, Pore gas and Water Saturation prediction map which generated by slicing the volumes at reservoir horizon levels.

6.2 Objectives versus Result

1. **Simultaneous Inversion as a proof of concept and provide a better image**

   Seismic Simultaneous Inversion has been giving a good match correspond to gas distribution at the Upper Gabus interval on the existing RAF wells both on 2 wells which used in the inversion and 3 wells as the blind well tests. This promising result is a proof of concept that Seismic Simultaneous Inversion can be used as one of the tools to approach the Hydrocarbon or Reservoir distribution prediction. Moreover, its derivative products which combined with rock physics techniques analysis could provide a better image to predict vertical (figure 6.1) and lateral section of reservoir character distribution (figure 6.2) compare to conventional seismic interpretation techniques.

2. **Identify potential areas**

   Through the observation from cross plot volume section and slice, Sand, Porosity, Pore gas and Water Saturation prediction map, it can be concluded that good quality sand and gas accumulation of Upper Gabus formation at RAF field consistently are distributed widely at UG-1A and UG-1B interval. These distributions form channel-like trend feature both at UG-1A and UG-1B. From the slices, it is seen that going northeastward, sand quality is getting poorer in porosity and sand percentage. This can be interpreted that the sediment source was coming from the southwest and settled into a lacustrinal deltaic system at the northeast.

   When it overlaid by structure contour and its associated fault, it can be identified 2 potential areas: first, at Eastern flank of RAF structure and second, at Northwest flank of NE RAF structure nose. These areas could be the potential candidates for further integrated study.

   First areas, identified at Eastern flank of RAF structure with VShale varies at 12% - 38%, Porosity approx. vary at 27% – 38% and 4% – 49 % of water saturation. Second area, is located at Northwest flank of NE RAF structure nose. In this area, Porosity is ranging approx. at 27% - 34%, VShale vary at 23% - 39% and water saturation at 12% - 49%.

On both areas, it is expected that hydrocarbon is still trapped on this faulted compartmentalization. By placing wells at these areas, it is expected could optimize the gas recovery from this field.

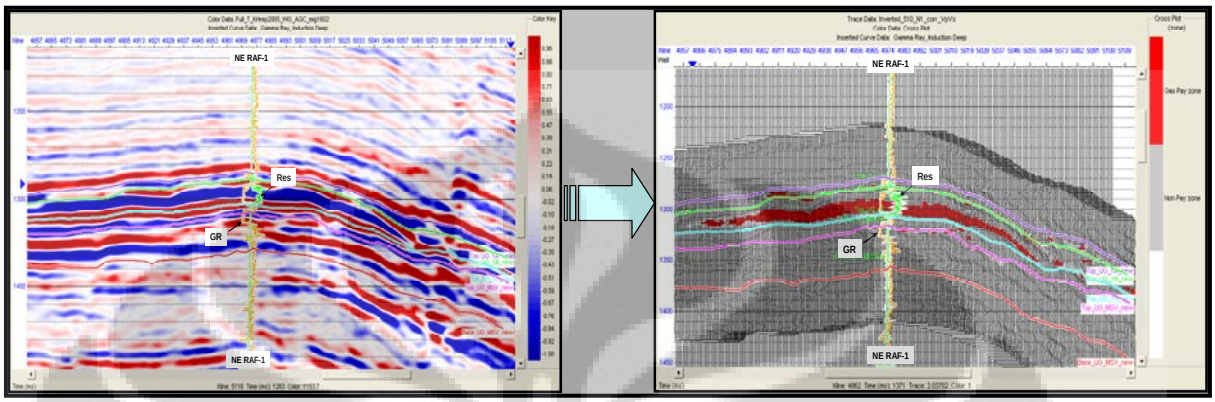

Figure 6.1 Simultaneous Inversion combined with rock physics technique analysis provide better image of vertical section.

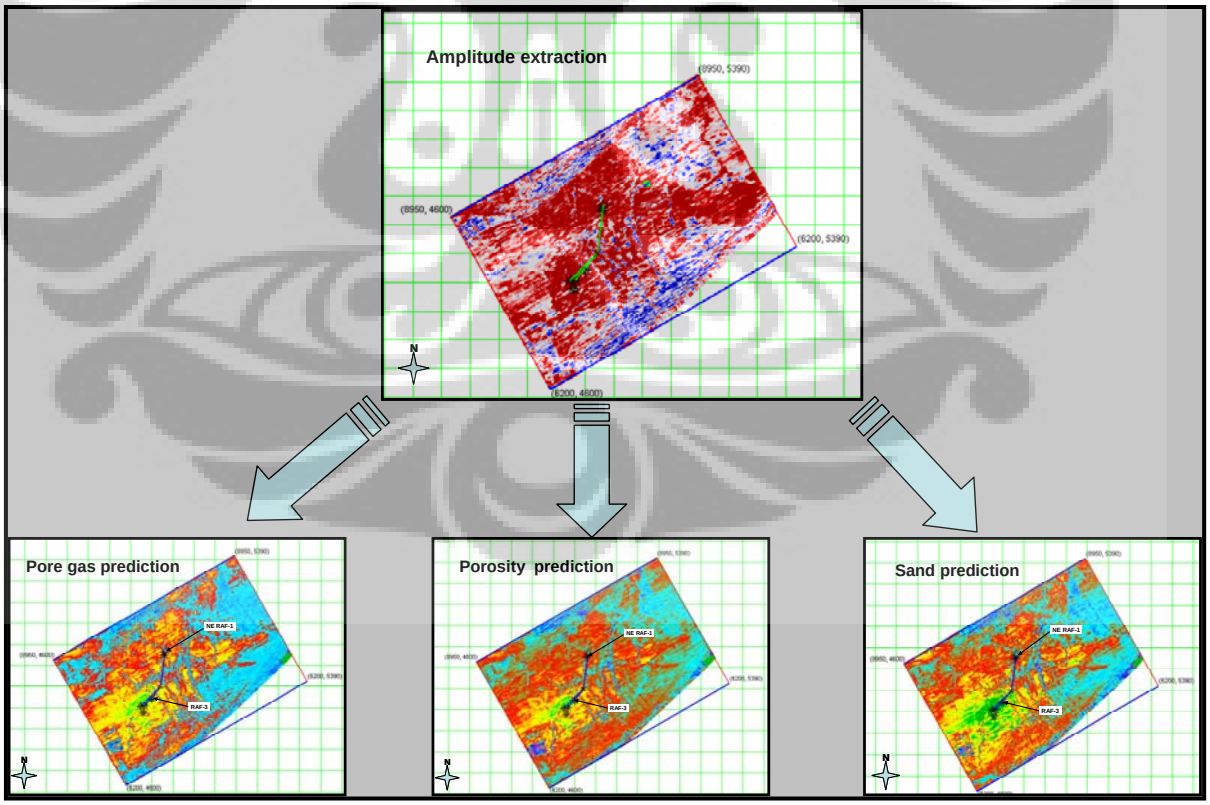

Figure 6.2 Simultaneous Inversion derivative products provide better image of lateral section.

6.3 Pitfalls

However, from the result observation, it is admitted that errors and uncertainties are still remain in this inversion such as:

- A certain reservoir sands such as sands at UG-1C and UG-Massive intervals which thickness less than 30 ft, were not identified as gas zone as expected. This could be interpreted due to tuning thickness effect. As it is expected on the feasibility test, some of sand units may not resolved in seismic resolution.
- Gas zone may over predict at the unexpected area particularly at down dip structure area. This possibly could be explained due to:
  - A single universal wavelet for every partial stack volume used for this inversion. This is just an estimated wavelet while in the real; wavelet could vary across the area.
  - Overlap areas of the poor discrimination area possibly also contribute in this uncertainty.

6.4 Recommendation

Understanding the result and pitfalls, it is considered that this study is an alternative interpretation to investigate gas distribution over the field. It is not intending to answer all of the problems. The result of this study could be assumed as the preliminary identification and can not work alone. It should be followed up by other integrated studies. Fault seal analysis study; to check whether the fault is sealed or not, Reservoir modeling and simulation study should also be conducted further to check how far the drainage radius affected.

On the reservoir properties, Porosity volumes was predicted from a simple linear relationship between PHIE and P-Impedance, Sand prediction or VShale volume was also predicted from a simple linear relationship between Density and VShale, Water Saturation volume was generated simply from Wyllie's equation, and Pore gas was simply predicted from Lambda Rho. Therefore, a more comprehensive geostatistic modeling may be required to get more accurate of lithology, porosity and water saturation qualitative prediction.

REFERENCES

Avseth P, Mukerji T., & Mavko G., 2005. Quantitative Seismic Interpretation, Applying Rock Physics Tools to Reduce Interpretation Risk. Cambridge University Press. UK

Aki, K., and Richards, P.G., 2002, Quantitative Seismology, 2nd Edition: W.H. Freeman and Company.

ConocoPhillips Indonesia Internal Reports, Unpublished

Daines, S.R., 1985. Structural History of the West Natuna Basin and the Tectonic Evolution of the Sunda Region. Proceedings of the Indonesian Petroleum Association 14th Annual Convention, Jakarta. p. 39 – 61.

Fatti, J., Smith, G., Vail, P., Strauss, P., and Levitt, P., 1994, Detection of gas in sandstone reservoirs using AVO analysis: a 3D Seismic Case History Using the Geostack Technique: Geophysics, 59, 1362-1376.

Ginger, D.J., Ardjakusumah, W.O., Hedley, R.J., and Pothecary, J., 1993. Inversion History of the West Natuna Basin : Examples from the Cumi-Cumi PSC. Proceedings of the Indonesian Petroleum Association 22nd Annual Convention, Jakarta. p. 635 – 658.

Goodway, B., Chen, T., and Downton, J.,1997, Improved AVO fluid detection and lithology discrimination using Lame petrophysical parameters: "λρ", "μρ"and "λμ fluid stack", from P and S inversions, CSEG Expanded Abstracts,148-151.

Hampson, D., Russell, B., and Bankhead, B., 2005, Simultaneous inversion of pre-stack seismic data: Ann. Mtg. Abstracts, Society of Exploration Geophysicists.

Pendrel, J., and Goodway, W., 2000, Estimation and interpretation of P and S impedance volumes from simultaneous inversion of P-wave offset seismic data, 70th Ann. Int. SEG Mtg, p.174-177.

Russell, H., 1999 Theory of the Strata Program, Hampson-Russell Software Services

Sukmono, S., 2002 An Introduction to Seismik Reservoar Analysis, in Seismik Inversion and AVO Analysis for Reservoar Characterization, Department of Geophysical Engineering ITB, Bandung

Suprajitno, M., 2000. Physical Aspect of Exploration Seismology, Geophysics Program of Mathematics and Sciences Department UI, Depok

White, JR, J.M., Wing, R.S., 1978. Structural Development of the South China Sea with Particular Reference to Indonesia. Proceedings of the Indonesian Petroleum Association 7th Annual Convention, Jakarta. p. 159 - 177.

Wongsosantiko, A., Wirojudo, G.K., 1984. Tertiary Tectonic Evolution and Related Hydrocarbon Potential in the Natuna Area. Proceedings of the Indonesian Petroleum Association 13th Annual Convention, Jakarta. p. 161 – 184.